INFORMATION TO USERS

This manuscript has been reproduced from the microfilm master. UMI films the text directly from the original or copy submitted. Thus, some thesis and dissertation copies are in typewriter face, while others may be from any type of computer printer.

The quality of this reproduction is dependent upon the quality of the copy submitted. Broken or indistinct print, colored or poor quality illustrations and photographs, print bleedthrough, substandard margins, and improper alignment can adversely affect reproduction.

In the unlikely event that the author did not send UMI a complete manuscript and there are missing pages, these will be noted. Also, if unauthorized copyright material had to be removed, a note will indicate the deletion.

Oversize materials (e.g., maps, drawings, charts) are reproduced by sectioning the original, beginning at the upper left-hand corner and continuing from left to right in equal sections with small overlaps. Each original is also photographed in one exposure and is included in reduced form at the back of the book.

Photographs included in the original manuscript have been reproduced xerographically in this copy. Higher quality 6" x 9" black and white photographic prints are available for any photographs or illustrations appearing in this copy for an additional charge. Contact UMI directly to order.

UMI®

.

Diffusion-Based Microalloying via Reaction Sintering

by

Donald Paul Bishop

A Thesis Submitted to the Faculty of Engineering

in Partial Fulfillment of the Requirements for the degree of

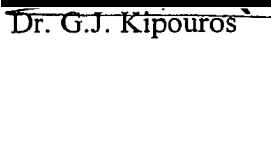DOCTOR OF PHILOSOPHY

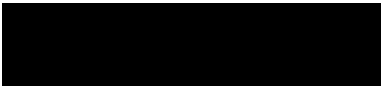Major Subject: Metallurgical Engineering

Approved:

_____
Dr. W.F. Caley

_____
Dr. G.J. Kipouros

_____
Dr. M.C. Chaturvedi

_____
Dr. F. Taheri

_____
Dr. Hani Henein

Dalhousie University - DalTech

Halifax, Nova Scotia   1998

DALHOUSIE UNIVERSITY - DALTECH LIBRARY

"AUTHORITY TO DISTRIBUTE MANUSCRIPT THESIS"

TITLE :

Diffusion-Based Microalloying via Reaction Sintering

The above library may make available or authorize another library to make available
photo/microfilm copies of this thesis without restrictions.

Full Name of Author :   Donald Paul Bishop

Signature of Author :

Date :   June 26/98

TABLE OF CONTENTS

vi

LIST OF FIGURES

xi

LIST OF TABLES

LIST OF ABBREVIATIONS AND SYMBOLS

Symbol

at%	Atomic Percent
BFI	Bright Field Image
CDFI	Centered Dark Field Image
CIP	Cold Isostatic Press
CIPing	Cold Isostatic Pressing
D	Diffusion Coefficient
DP	Diffraction Pattern
EDS	Energy Dispersive System
EPMA	Electron Probe Micro-Analysis
GP	Guinier-Preston
GP1	Guinier-Preston 1
GP2	Guinier-Preston 2
GPZ	Guinier-Preston Zone
HV	Vickers Hardness
HRB	Hardness Rockwell "B"
I/M	Ingot Metallurgy
K	Degrees Kelvin
LPS	Liquid Phase Sintering
PFZ	Precipitate Free Zone
P/M	Powder Metallurgy
S'	Intermediate precipitate of Al_2CuMg
S	Equilibrium precipitate of Al_2CuMg
SCE	Stress Corrosion Cracking
SEM	Scanning Electron Microscope
SFE	Stacking Fault Energy

SSS	Solid State Sintering
SLPS	Supersolidus Liquid Phase Sintering
T	Time
TEM	Transmission Electron Microscope
UTS	Ultimate Tensile Strength
wt%	Weight Percent
XRD	X-Ray Diffraction
% RA	Percentage Reduction in Area
ε	Elongation to Fracture
Ω	Omega Precipitate
θ''	Intermediate precipitate of $CuAl_2$
θ'	Intermediate precipitate of $CuAl_2$
θ	Equilibrium precipitate of $CuAl_2$
ρ	Density
σ	Yield Strength (0.2% Offset)
δ	Equilibrium Precipitate of $LiAl_3$
δ'	Intermediate Precipitate of $LiAl_3$
η	Equilibrium Precipitate of Mg_2Zn
η'	Intermediate Precipitate of Mg_2Zn

ACKNOWLEDGEMENTS

ABSTRACT

In an effort to improve the properties of Al-based alloys, microalloying with select elements has proven to be a viable method. Despite the broad variations in alloys and microalloying additions considered, almost all studies have relied on the use of traditional ingot metallurgy practices. Consequently, any influence from the means of alloying is seldomly addressed. With this in mind, an alternative technique termed "core/shell" processing was developed based on powder metallurgy principles.

Prior to initiating "core/shell" experiments, the sintering response of two alloy powders (ternary Al-4Cu-0.5Mg and a commercial P/M version of 2014 Al-4.4Cu-0.8Si-0.8Mn-0.5Mg) was assessed. Both alloys responded well to sintering and reached sintered densities that facilitated final swaging to near theoretical density.

Numerous samples microalloyed with Li, Sn or Ag as well as alloy standards were prepared using a variety of sintering times. Mechanical and physical properties of the "core/shell" processed samples were then characterized and compared to those of alloy standards. The properties evaluated included age hardening response/TEM, tensile behaviour, dry sliding wear resistance, density and the corrosion rate in salt water.

Results of age hardening experiments indicated that Ag promoted a substantial increase in peak hardness in the ternary alloy, but was far less effective in commercial P/M 2014. Similar experiments were conducted with Sn-bearing samples of P/M 2014. It was discovered that Sn promoted a decrease in both hardness and tensile strength; this became more acute as sintering time was prolonged. Since Sn accumulated in the intergranular regions, the soft malleable nature of this metal was then imparted to P/M 2014. Consequently, the reduction in hardness and tensile strengths resulted.

In wear tests of P/M 2014 standards, a trend of reduced resistance to wear with increased sintering time was noted and postulated to be the result of microstructural coarsening. Despite the occurrence of similar coarsening in Sn modified samples, wear resistance was found to increase with sintering time and in turn Sn content. This resistance was found to surpass all P/M samples considered as well as a wrought version of 2014. Although Ag appeared to promote a similar response, the extent of improvement was relatively minor. It was postulated that Sn would melt through the frictional heat developed during sliding, thus reducing the direct metal to metal contact and consequently, wear rate.

To determine the corrosion resistance of samples based on P/M 2014, polarization resistance curves were measured. Relative to a wrought counterpart, P/M samples exhibited a superior resistance to corrosion. Due to the relatively minor extent of Sn and Ag additions, the majority of samples exhibited a similar rate of attack.

Through the completion of this work, several of the benefits that P/M processing offers over ingot metallurgy were explored. Those included were near net shape formability, reduced machining, as well as enhanced mechanical properties and corrosion resistance. Using the fundamental principles of P/M, a novel technique for microalloying P/M products was developed. Relative to ingot metallurgy techniques the process offers the versatility of P/M and is specifically advantageous through its ability to (i) alloy selected regions of a given component, (ii) vary the extent of alloying (macro/micro) and (iii) vary the depth of alloying (surface/through thickness). Furthermore, since the process is potentially feasible for several alloying additions and alloy systems it may well prove to be a viable industrial practice.

1 INTRODUCTION

Through consumer demands for improved metals performance, new and innovative alloys are being developed on a regular basis. Such developments have led to the production of alloys typically based on iron, aluminum, copper, and nickel. Despite this broad variety, iron-based alloys have traditionally received the lions share of the global market. Aluminum-based alloys, however, are inherently light weight and tailorable to strengths comparable to those of certain steels; thus they have emerged as the principle competitor [1]. Amongst the many possible methods available to enhance the mechanical properties of aluminum to a level comparable to steel, alloying tends to have the most direct influence. Thus, alloying has justifiably received a considerable amount of attention, and is presented in detail in the following sections.

1.1 MACROALLOYING OF ALUMINUM

The most common alloying elements for aluminum include copper, magnesium, silicon, zinc, manganese, and lithium, typically added on the order of one to several weight percent. By varying the amounts and combinations of such elements, the net mechanical and physical properties can be suitably altered. Such alterations may be achieved through microstructural modifications, including the formation of secondary phases, solid solutions and the promotion of age hardening behaviour. For example, as shown in Figure 1.1 [2,3], alloying additions have a profound effect on the stiffness of aluminum, both positively and negatively. Aside from influences on the mechanical properties of aluminum, alloying additions are also known to affect corrosion resistance, electrical conductivity, thermal conductivity, and as shown in Figure 1.2, density [2,3].
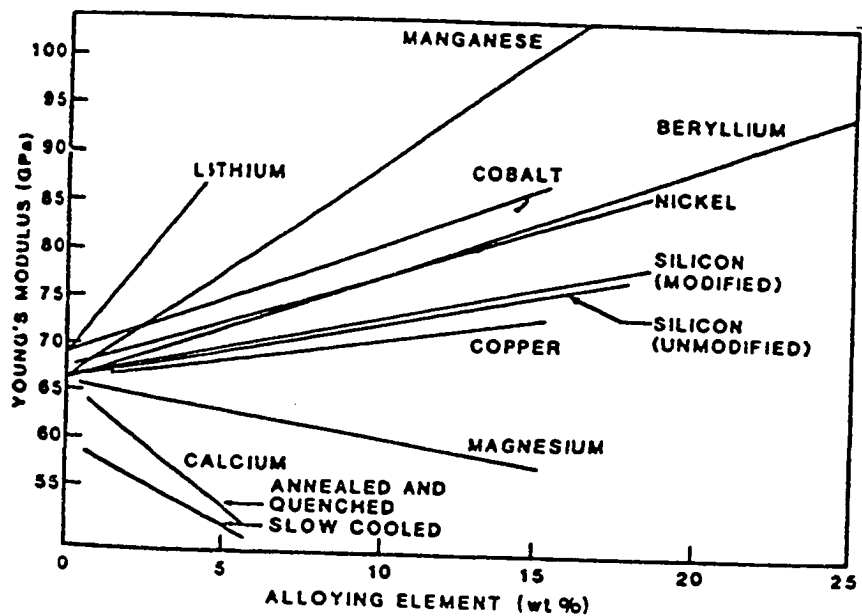
Figure 1.1 Effects of various elements on the Young's modulus of aluminum [2,3].
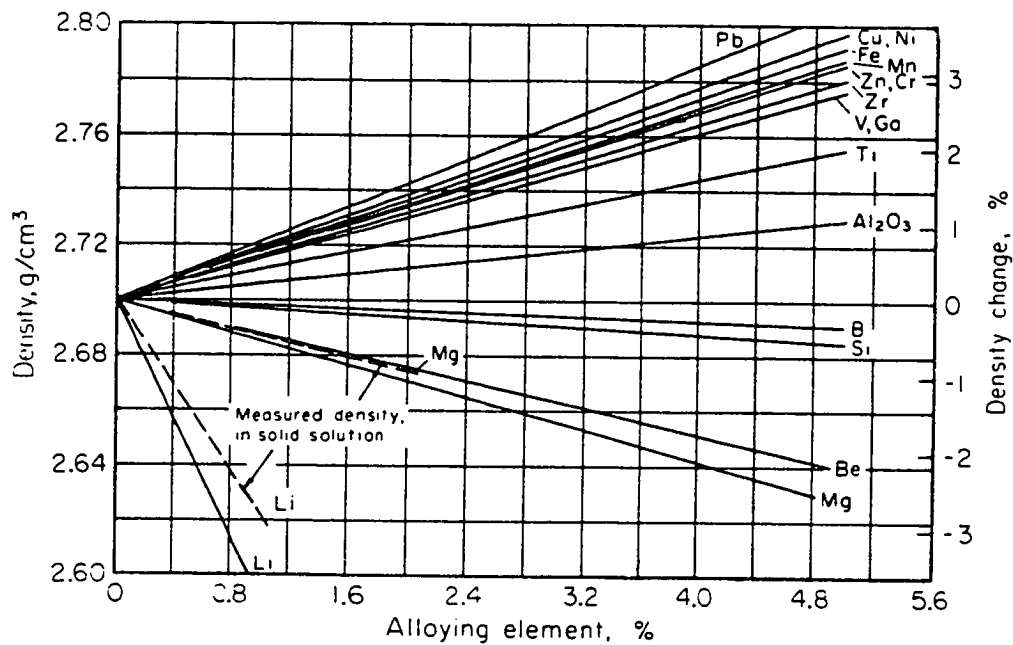
Figure 1.2. Influence of alloying additions on the density of aluminum [2,3].

1.2 MICROALLOYING OF ALUMINUM ALLOYS

Although the majority of alloying elements are added to aluminum at levels of the order of one weight percent, considerable research has shown that several can be added in trace amounts (0.1 to 0.01 wt%) yet still have a significant influence on the resulting microstructure, and subsequently, mechanical properties [4]. Elements including yttrium, cadmium, indium, tin, cobalt, zirconium, titanium, vanadium, beryllium, bismuth, silver, and germanium, are in this category and will be discussed in later sections.

When added to aluminum alloys, trace elements can have several possible effects. Firstly, they may act to alter precipitation processes in age hardenable alloys. As these precipitation processes are responsible for producing the high strengths associated with such alloys, the majority of research has been focused here. Secondly, trace elements may act to refine the resulting grain size in cast structures and modify secondary phases, such as eutectics, which may exist within the bulk microstructure of alloys. Each of these effects will be individually discussed in the following sections.

1.2.1 Influence on Precipitation

In all high-strength aluminum alloys, the phenomenon of age hardening is responsible for the strength levels achievable. A general age hardening procedure begins with a solutionizing step in which alloying elements are dissolved into solid solution at an elevated temperature, followed by quenching. The result is a supersaturated solid solution, which is subsequently reheated to a moderate temperature, typically of the order of 433-453 K. During this secondary treatment, elements initially dissolved in solid solution are precipitated out as a relatively homogenous distribution of fine, ordered intermetallics. In order to optimize strength, a combination of shearable non-shearable precipitates is desirable [4, 5]. This avoids planar shear and in turn, low ductility. Such precipitates are typically ordered intermetallics (i.e. Al_2Cu, Al_3Li), carbides (NbC), or

nitrides (BN), and their formation leads to dramatic improvements in numerous mechanical properties.

The precipitation process in age hardenable aluminum alloys has been shown to consist of several essential stages [4], the order and nature of which depends primarily on alloy composition. In general, the sequence begins by the formation of coherent clusters of atoms known as Guinier-Preston zones (GPZs), followed by precipitation of an ordered, intermetallic phase semi-coherent in nature. Such phases are typically referred to as "prime phases" (i.e. θ', δ', S'), and are typically associated with optimum strength levels. An outline of the more commonly encountered precipitates is given in Table 1.1. The smaller and more homogeneously distributed these precipitates are, the higher the overall strength. With extended aging, coherency is lost, and precipitates eventually become fully incoherent equilibrium phases (i.e. θ, δ, β).

In order to enhance precipitation, a fine dispersion of preferential sites for nucleation must exist. In some alloy systems, dislocations are the preferred sites for nucleation; thus, precipitation density can be increased by a slight deformation prior to aging. Another possible site for preferential nucleation in many systems, however, has been clusters of trace elements [4]. Through this clustering action, an interface is created; this provides a site for preferential nucleation. Since these clusters tend to be extremely small and uniformly dispersed, the resulting precipitate pattern is so as well. Typically, elements having a larger atomic radius than aluminum, which can readily interact with smaller atoms and vacancies, tend to form the most stable clusters. Despite this fact, transition elements such as Ni and Fe, which are actually smaller than aluminum atoms, also hold promise.

A typical example of this phenomenon is the influence of small amounts (~0.1 wt%) of Cd, In and Sn on θ' ($CuAl_2$) precipitation during aging of an Al-Cu binary which

Table 1.1 Common precipitates encountered in age hardenable Al alloys [2-4].

	Chemistry	Crystal Structure	Habit Planes	Morphology
θ'	Al_2Cu	Tetragonal	{100}	Blocky plates
S'	Al_2CuMg	Orthorhombic	{100}, {210}	Rods, needles
Ω	Debatable	Debatable	{111}	Thin hexagonal plates
δ'	Al_3Li	Cubic		Spherical
T_1	Al_2CuLi	Hexagonal	{111}	Thin hexagonal plates

serves as the basis of many commercial alloys. Through the work of Sankaran et al [6], it was discovered that all three elements promoted the formation of a larger number of smaller θ' precipitates than obtained in the alloy free of trace elements. Using transmission electron microscopy (TEM), it was discovered that the trace elements had a tendency to segregate to the α-Al/θ' interface, thereby lowering the associated interfacial energy. It was thus concluded that increases in θ' precipitate density were attributable to this reduction in the height of the energy barrier facing nucleation.

In 1994, Ringer et al [7] conducted further work into the influence of Sn on θ' precipitation in the binary Al-Cu system. These workers highlighted the fact that the theory previously proposed by Sankaran [6] was indeed possible, yet an alternative explanation also existed. This alternative was that a phase containing a large concentration of the trace element precipitates out first, and subsequently acts as a preferential site for θ' nucleation. In an attempt to prove which theory was correct, samples of aged Al-Cu alloys with and without Sn additions were examined using high resolution (~0.2 nm) atom probe field ion microscopy. The results revealed that Sn initially formed clusters and then precipitated as very small, non-coherent, spherical particles of pure β-Sn. Later, θ' nucleated and grew on these particles, and the result is a much finer distribution of θ' and in turn peak hardness. The absence of GPZs and θ'' precipitates which normally precede the θ' precipitation was justified on the basis that

both require substantial concentrations of vacancies to form. Since the Sn clusters acted as preferential vacancy sinks, an insufficient amount of vacancies was available for GPZ and θ'' formation. Furthermore, the effect of cold work prior to aging was also considered. Such experiments revealed that cold working prior to aging eliminated the benefits of Sn additions previously encountered [7]. It was reasoned that since the dislocation density is increased by cold working, and that Sn atoms have a tendency to gather on such defects, the atoms were in effect, pinned down and did not act as additional sinks. Hence the formation of β-Sn precipitates and the beneficial effects on hardness did not occur.

Aside from work with the Al-Cu binary system, studies have also been conducted on the effects of trace element additions to the Al-Li [8] and Al-Mg [9] systems. By adding 0.19% Sc to an Al-2.4Li alloy, Miura et al [8] studied the resulting aging behaviour. They discovered that Sc reacted to form Al_3Sc precipitates, which acted as preferential sites for δ' (Al_3Li) nucleation. Thus, aging samples at 673K showed that those containing Sc had a significantly higher peak hardness. Not only did Sc promote δ' nucleation, but also acted to restrict its subsequent coarsening during prolonged aging. Further optimization of the aging procedure uncovered the potential to achieve an even higher peak hardness by initially aging at 673K followed by further aging at 473K. Whereas the higher temperature stage generated Al_3Sc precipitates, subsequent aging at the lower temperature resulted in δ' precipitation. Using such an aging procedure, overaging at the lower temperature produced an interesting effect whereby composite precipitates formed consisting of an Al_3Sc core which was surrounded by a shell of Al_3Li.

In another study devoted towards the effects of Sc on aging of Al alloys, Royset et al [9] considered the influence on an Al-Mg binary alloy. As in the work of Miura, an improved peak hardness was realized with the alloys containing Sc; this was again

attributed to Al_3Sc formation. Using dual stage aging, the peak hardness was the same as that found for single stage aging, yet was achieved in 60% less time.

Broadening the scope of the effects of Sc on Al-Mg alloys, Parker et al [10] added up to 1 wt% Sc to alloys of Al-Mg, Al-Mg-Zn and Al-Mg-Ag. Acknowledging the work of others it was noted that Sc does not form compounds with Mg, Zn or Li, and therefore its overall effect on alloys containing such additions is enhanced. Also noted, however, was that the beneficial effects of Sc are markedly reduced in Al alloys containing Cu or Si due to a preferential tendency to react with these elements. Within the alloys examined, it was discovered that Sc promoted significantly higher hardness in Al-Mg alloys when aged between 563-593K. Although the effect of adding Sc to the ternary alloys was considered, it was found less effective due to difficulties in finding an appropriate solutionizing treatment. This point illustrates one of the many potential problems that can arise when dealing with alloys more complex than simple binary systems.

Another addition that has proven beneficial towards the aging response of many alloys is Ag. Microalloyed into ternary Al-Cu-Mg alloys [11-16] Ag additions were found to have a profound influence on θ-type precipitates. The fact that Ag influences these precipitates was discovered in the 1960s [11], and has recently received a great deal of renewed interest. Focusing primarily on alloys of a high Cu:Mg ratio (i.e. 10:1 to 6:1), the addition of a small amount of Ag (~0.4 wt%) has a profound effect on θ-type precipitates. Because of this addition, such precipitates are converted into others referred to as Ω, having a different family of habit planes ({111}) and crystalline structure, the exact nature of which remains in dispute [12-14]. Although also of a general plate-like morphology, these plates are much broader and thinner than θ', and are hexagonal in shape. The chief similarity is chemical composition, yet this point also remains in question.

Through studies such as these, Ag microalloying has risen in popularity, leading to the development of several new commercial alloys. Perhaps of greatest significance is the generation of an alloy referred to as Weldalite 049 [17]. Compositions of this alloy as well as several other commercial alloys commonly used in microalloying experiments are shown in Table 1.2. For example, in alloys based on the Al-Li-Cu system, a trace addition of 0.4 wt % Ag can result in a tensile strength of ~700 MPa, the highest ever recorded for a commercial Al alloy. Furthermore, ALCOA has recently announced a new series of Al-Cu-Mg-Mn-Ag alloys [18]. Because of the attractive elevated temperature properties of Ω, such alloys are designed for extended use at moderate temperatures (400K).

Table 1.2 Nominal compositions (wt %) of several commercial Al-alloys frequently used in microalloying experiments [19].

Alloy	Al	Cu	Li	Mg	Mn	Si	Ti	Zr
2020[1]	Bal.	4.5	1.1	---	0.5	---	---	---
2090	Bal.	2.7	2.3	0.25	---	0.1	0.15	0.12
2219[2]	Bal.	6.3	---	---	0.3	0.2	0.06	0.2
8090	Bal.	1.3	2.4	1.0	---	0.2	0.1	0.1
Weldalite 049[3]	Bal.	6.0	1.3	0.4	---	---	---	0.14

1 Additional 0.2 wt % Cd   2 Additional 0.1 wt% V   3 Additional 0.4 wt % Ag

Despite the complexities encountered when studying the effects of trace elements on commercial Al alloys, many researchers have conducted such studies with significant degrees of success. Since Al-Li based alloys, as used in the aerospace industry, are amongst those most frequently found to suffer from poor fracture toughness, the majority of research has focused on this alloy system. For example, Gilmore et al [20] added 0.1 wt% In to alloy 2020 and discovered a significantly accelerated aging response at 433K.

Despite these results, the exact reasoning for the response was unknown, and it was concluded that the catalytic role of trace elements remains poorly understood.

In the work of Starke and Lin [21] on the influence of grain structure on ductility of alloy 2020, it was noted that a small amount of Cd (0.2 wt%) is deliberately added to this alloy. Adding Cd is known to suppress θ'' formation, while raising the density of θ' precipitates and restricting subsequent coarsening. It was stated that θ' growth kinetics are restricted due to Cd segregation to the θ'/α-Al interface thus lowering the interfacial energy; this was also reported by Sankaran [6].

Further work by Starke et al [22] on the effects of trace additions of Cd, In and Sn on the aging behaviour of Al-Li based alloy 2090 revealed that In greatly increases alloy hardness when peak aged (Figure 1.3). Whereas Cd produced minimal improvements, Sn actually promoted a decrease in hardness throughout the entire aging cycle. Using TEM, it was determined that alloys containing In had a significantly higher concentration of both T_1 and θ' precipitates. While all three elements acted to improve alloy ductility and fracture toughness, only In increased tensile strength as well.
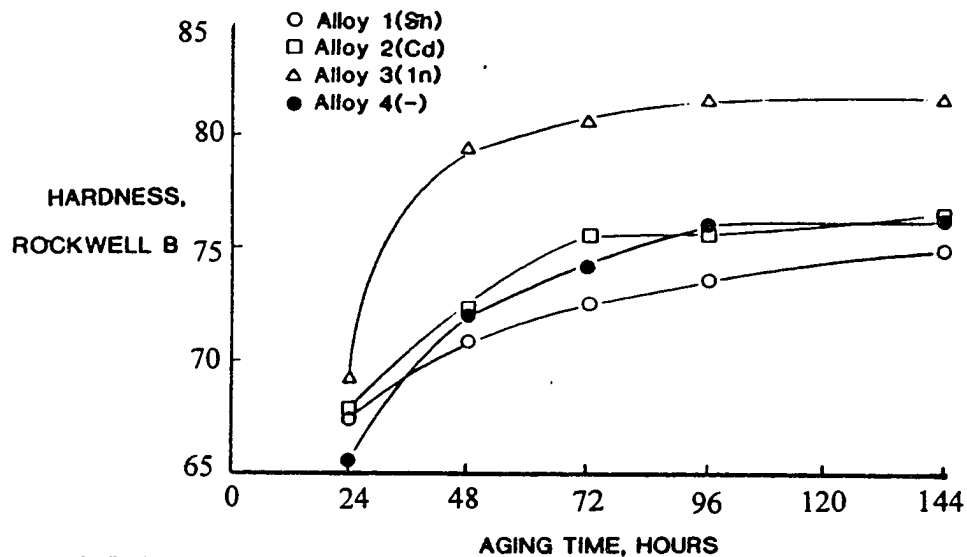
Figure 1.3 Influence of various elements on the aging response of alloy 2090 [22].

Also experimenting with alloy 2090, Park et al [23] studied the effects of adding 0.39 wt% Be. In examining the age hardening response, it was noted that Be-bearing alloys had only a slightly improved hardness when peak aged. Interestingly, a seldom-encountered secondary aging peak was noted. TEM studies indicated that Be caused heterogeneous precipitation of δ', thus restricting the potential development of high hardness. Further precipitation studies confirmed that Be restricted T_1 coarsening and promoted the formation of θ'/δ' composite phases.

Due to a great commercial interest in Al-Li based alloys, many researchers have investigated alloy 8090. For example, Luo and Youdelis [24] added trace levels of V and Be to 8090. In doing so, they found that both elements caused the age hardening rate, peak hardness and in turn tensile strength, to be improved over the unmodified base alloy. Despite optimizing the aging response of 8090 by a deformation prior to aging, the peak hardness of alloys containing trace element additions remained superior. The noted improvements were attributed to an increased density of S' (Al_2CuMg) precipitates. As a cautionary note, although tensile strength and ductility improved with the addition of V, it was also reported that the formation of coarse $Al_{11}V$ precipitates resulted in a loss of impact toughness.

In other work by the same authors [25], the effect of 0.15% Be on alloy 8090 was assessed. It was found that Be promoted an improved hardening response during aging. This increased yield and ultimate tensile strength, although impact toughness remained constant. As has often been the case, such improvements were believed to be due to a decrease in size and increase in density of precipitates. In a continued study of the same system [26], the authors discovered that Be initially encouraged the formation of clusters of vacancies, together with Cu, Mg and Be atoms. From these clusters, the normal precipitation sequence for the unmodified alloy followed.

Using a less frequently chosen element for microalloying, Gui et al [27] added 0.1 wt% Y to aluminum alloy 8090. Examination of the Y-containing alloy showed an increased uniformity in the precipitation of S', but a restricted growth of a second precipitate encountered in this alloy - δ'. Consequently, the yield and ultimate tensile strengths actually fell slightly, although ductility improved.

The effect of the addition of trace levels of Te to alloys similar in composition to 8090 was examined by Al-Haidary and Jabur [28]. Studies showed that alloys containing Te exhibited a lower hardness and tensile strength in the peak aged condition, whereas the ductility and fracture toughness were also improved. It was postulated that strength loss was due to the formation of a small number of large δ' precipitates because of the presence of Te. The improvement in toughness, however, was believed to be the result of a decrease in stress produced around precipitates due to an expansion in the lattice parameter of α-Al. Alloys containing Te were also found to exhibit superior oxidation behaviour. Therefore, the loss of Li typically encountered during heat treatment [29] was avoided.

Finally, Hagiwara et al [30] examined the effects of Li addition on the behaviour of an aluminum alloy, 2219. Adding Li in amounts ranging from 0.13 to 1.25 wt%, resulted in the highest yield strength reported for such alloys, yet lowest ductility. In assessing fracture toughness, alloying with 0.13 wt% Li proved optimum, and a trend of increasing T_1 precipitate density with increasing Li content was found using TEM. However, θ' precipitation remained unchanged.

As previously mentioned, a homogenous distribution of precipitates is necessary if full strengthening effect is to be realized. However, this is rarely the case. Early in the 1950's it was recognized that narrow zones adjacent to grain boundaries and secondary phases were frequently devoid of precipitates [31]. The presence of such precipitate free

(PFZ) or "denuded" zones (Figure 1.4) is common to a broad variety of alloy systems and has a pronounced, negative influence on mechanical properties. Alloys susceptible to PFZs include carbon steels [32], stainless steels [33], Fe-Mn-based alloys [34,35], Ni-based alloys [36], and Al-based alloys [37-44]. To successfully produce a fully homogenous distribution of precipitates during aging, sources of vacancies (for nucleation and solute atom mobility) and precipitating elements are required. Grain boundaries, however, reduce this possibility since they may act as both a vacancy sink and site for preferential segregation or precipitation of a solute-based phase. Hence, the region immediately adjacent to grain boundaries is often depleted of one or more of the constituents essential for homogenous nucleation, resulting in the formation of a PFZ. Whereas this occurrence is commonly accepted, physical verification remains difficult, since the maximum resolution of most instruments is comparable to the overall PFZ width [37,38]. Being precipitate free, these zones theoretically possess a tensile strength substantially lower than the surrounding alloy (~20 MPa versus ~600MPa respectively) and are thus preferred areas for plastic flow. Failure by this manner (near to but not directly along grain boundaries) is termed "pseudo-intercrystalline failure". Consequently, such alloys exhibit an inherently low fracture toughness, a situation that is characterised by a combination of large grain size and narrow PFZ.

Although this problem has been known to exist for many years, a heightened interest began in the 1960's and 1970's [44] with the advent of Al-Li based alloys. These alloys have excellent stiffness and strength to weight ratio, and thus were initially perceived to be the future materials for aerospace applications. However, these alloys are still plagued by low fracture toughness, and so their usage remains relatively restricted. In an effort to improve fracture toughness extensive studies have been undertaken; however, the general conclusion is still that the formation of precipitate free zones (PFZs) is still a contributing factor. Through these efforts, possible remedies have focused
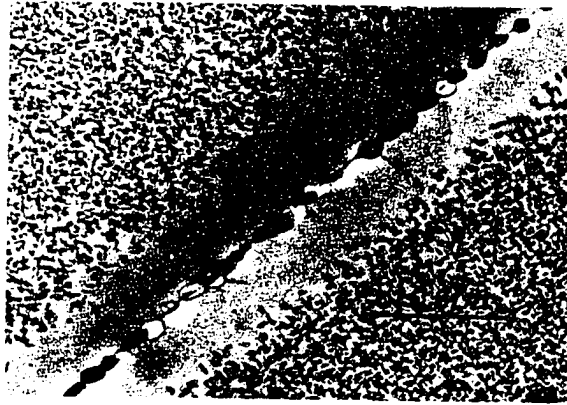
Figure 1.4. Typical appearance of a PFZ in an aluminum alloy [43].

principally on methods to alter the standard precipitation sequence in Al-base alloys such as the provision of suitable non-equilibrium sites for precipitation within the PFZ. The main techniques under development include trace element additions (Figure 1.5), heightened quenching rates, preaging and complicated thermal mechanical treatments [4].
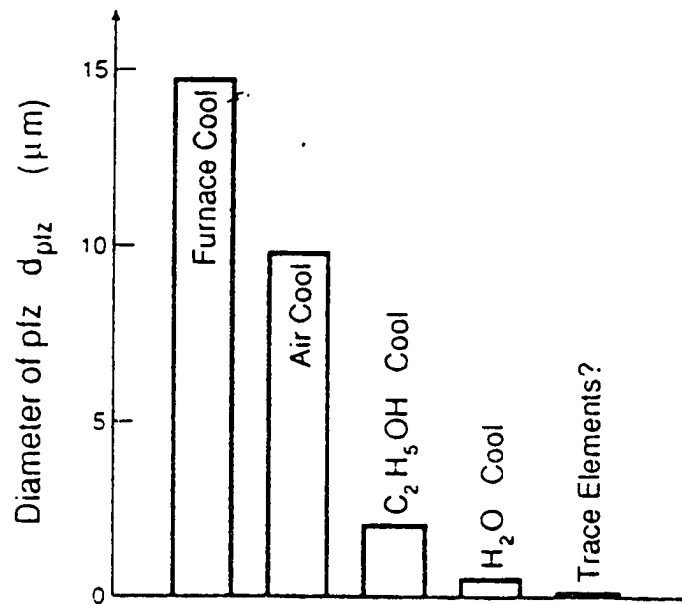
Figure 1.5 Comparison of quenching conditions and trace elements on PFZ size [4].

1.2.2 Grain Size Refinement

When the purpose is to influence a precipitation process in an age hardenable aluminum alloy, trace elements must be finely distributed within the alloy, and typically exist as very small ($\cong 10$ Å) clusters. However, such elements can also exist within the alloy as relatively larger ($\cong 500$ Å) dispersoids in the form of discrete, ordered intermetallics [45]. When present in this manner, the most notable influence is the promotion of recrystallization. In doing so, new grains tend to preferentially nucleate on the dispersoids, thus forming a finer grain size than is otherwise obtainable. Consequently, a strong potential to increase tensile strength and promote superplastic behaviour exists.

As the refining action of trace elements relies on the formation of insoluble intermetallics, the most appropriate elements are those which are highly chemically reactive with, but have limited solubility in aluminum. This serves to preserve the influence of all other alloying elements. Thus, although the required elements are fully dissolved in molten aluminum, once cast, stable intermetallics readily form during solidification.

Among the elements studied and exploited for such a use, Zr is most frequently encountered [45]. In studies conducted by Khatsinkaya et al [46], trace additions of Zr and Sc were added to Al-Li based alloy 1420. Results showed that Zr was indeed effective in reducing overall grain size, while contrary to this, Sc actually promoted grain growth. Despite the influence on grain size, neither was found to alter the precipitation processes occurring while aging. Using 8090, Yong et al [47] explored the effects of adding trace amounts of Zr, Ce or Mg on the susceptibility of the alloys to hot cracking during welding. When alloyed with Zr and Ce, the typical coarse, columnar grains found in the welded region were converted into those of a fine equiaxed morphology. It was postulated that the low solubility of these elements led to precipitation of Al_3Zr and

Al$_3$Ce within the molten weld pool. Since the precipitates acted as preferential sites for grain nucleation, the grain size was reduced. Apart from this observation, Ce and Mg were noted to promote a finer eutectic distribution within both the weld metal and heat affected zone. Through these effects, it was concluded that hot cracking susceptibility was lessened. Working with a more conventional alloy, Nieh et al [48] added various amounts of Zr to alloy 2124. These authors reported that an addition of 0.6 wt% Zr reduced the grain size to ~1 μm, thus enabling the alloy to behave in a superplastic manner. An addition of 0.12 wt%, however, was considerably less effective, and no superplastic behaviour was observed. Thus the conclusion was that the lesser amount of Zr formed an insufficient number of Al$_3$Zr precipitates to significantly reduce overall grain size.

1.2.3 Secondary Phase Modification

A final role trace elements are known to play in aluminum alloys is the modification of secondary phases, including eutectic/intergranular phases and iron-based impurity intermetallics. In numerous aluminum-based alloys known to contain significant amounts of such phases, the structure, nature, size and distribution is very important in determining the overall mechanical properties [49]. Intergranular phases, when in the form of an intermetallic, are often known to form continuous networks within an alloy. Consequently, the alloy tends to behave in a very brittle manner and may be highly susceptible to intergranular corrosion (i.e. 2xxx alloy series). Thus, a modification of the brittle network is essential to circumvent these tendencies.

Although such problems may be reduced by either an increased cooling rate, or use of an appropriate heat treatment [49], careful choice of a suitable trace element may also be a solution. For example, in Al-Si based alloys, primary Si typically precipitates out on cooling as large, sharp, broad, plate-like deposits [50]. Such morphologies frequently lead to high stress concentrations, and thereby a deleterious effect on

mechanical properties. To circumvent this problem, trace additions as low as 0.001 wt % Na or Sr are made, thus changing the Si-based phase to a more rounded, harmless morphology.

Experimenting with Be additions to A357 (an Al-Si-Mg casting alloy), Tan et al [51] observed considerable phase alterations with additions as low as 0.03 wt%. Results revealed that particles of an Si-based phase were converted into small, almost spherical deposits within the alloy matrix. Furthermore, Fe-based intermetallics, commonly associated with a loss of ductility, were also modified into more rounded, less harmful shapes. Since both of the modified phases were concentrated in the eutectic regions of the alloy, the eutectic as a phase was modified, thereby improving mechanical properties of the overall material.

Another secondary phase often encountered in aluminum alloys is a brittle, iron-based intermetallic. Iron, commonly present in aluminum as an impurity from the smelting process, readily forms brittle intermetallics with elements such as aluminum, silicon, magnesium and manganese [49]. Through effective refining practices, iron levels (and in turn iron-based intermetallics) are generally low in aluminum alloys (i.e. <0.15 wt %), yet an embrittling influence is still often noted. Thus, it is not only the amount, but also the shape and distribution of the iron-bearing constituent, which determines the resultant effects. To overcome this problem, appropriate trace elements can be added to transform the brittle intermetallics into a less harmful morphology, usually spherical.

Considering all of the trace elements mentioned thus far, each has been shown to enhance one mechanical property or another, although the improvement was often offset by a reduction in some other property(s). However, for Al-Li alloys in particular, two elements have been shown to cause detrimental effects, namely, Na and K. These elements tend to segregate at grain boundaries, and since the eutectic temperature for the Na-K binary system is reported to be −12 °C, a thin film of liquid tends to form along

grain boundaries. This liquid is believed to persist at ambient temperatures and below. Consequently, fracture toughness, tensile strength and ductility are greatly reduced, even in the presence of quantities as low as 10 to 20 ppm [52,53]. Hence every possible effort is made to minimize Na and K contents within Al-Li based alloys.

1.3 PROPERTIES OF SELECTED ALLOYING ELEMENTS

As shown in the preceding sections, an extensive array of trace elements may serve as beneficial additions to aluminum-based alloys. However, each must also exhibit physical properties that render the element amenable to the new alloying technique developed. Thus, although a review of many elements was completed in this regard, only those believed to be the most feasible and effective (Li, Sn, Ag) are discussed.

From a processing perspective, certain physical properties of any alloying additions must be assessed. Of great concern is the interaction between the additions and Al. In this regard, knowledge of solubility limits, intermetallic formation, and melting points is critical when assessing process feasibility. For example, should an element exhibit an appreciable solid solubility in Al, its introduction may be facilitated since it can accumulate in both the liquid and solid phases present during sintering. Furthermore, should the melting point of a given element be exceeded during sintering, it is also expected that its incorporation will be enhanced.

Aside from the interaction between Al and the alloying additions, knowledge on the interaction among the additions themselves may also be of use. In this respect, the presence of one element may act to reduce the activity of another. Consequently the flux of an element may also be reduced and in some instances, reversed. Unfortunately, a limited amount of experimental data exists for alloys similar to those used in this work.

In response to developing lighter, stronger aluminum alloys for aerospace and military applications, a tremendous amount of research has focused on alloys derived from the Al-Li system. Due to its inherently low density (Table 1.3) [54] for every 1 wt% Li added to Al, a 3% weight savings results [2,3]. Considering the Al-Li system (Figure 1.6) [55] it can be seen that Li reaches a peak solid solubility in Al of ~4.5 wt% at a temperature of 595°C. This, together with an inherently low melting point (Table 1.3) renders Li as an excellent candidate element from a processing standpoint. Although up to 4.5 wt% Li can potentially be dissolved in Al, commercial alloys typically contain <2.8 wt%. Should this value be exceeded, a detrimental effect on mechanical properties may result [2,3].
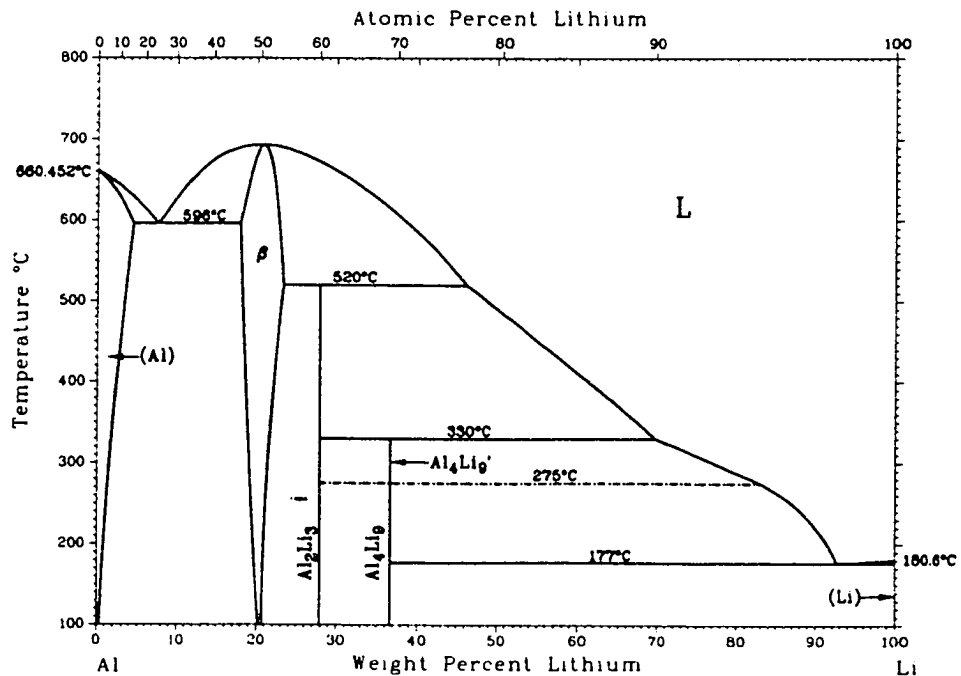
Figure 1.6 Al-Li binary phase diagram [55].

The Al-Sn binary system is presented in Figure 1.7 [56]. As indicated in the figure, Sn has a minimal solubility in solid Al at all temperatures, reaching a maximum of only 0.12 wt% at ~600°C. Although the solid solubility is low at this temperature, that in the corresponding liquid component is ~55 wt%. Despite a limited solid solubility, it is postulated that the introduction of Sn should still be feasible because of its low melting point (Table 1.3).

Of the three elements considered (Li, Sn, Ag), Ag exhibits the highest solid solubility limits in Al (Figure 1.8) [57], reaching ~23 wt% at a temperature of 600°C. At this same temperature, equilibrium dictates that Ag may also exist in the corresponding liquid phase to a concentration of ~48 wt%. As shown in Table 1.3 metallic Ag melts at a temperature higher than that of sintering (600-630°C). However, its substantial solubility qualify it as a highly feasible and effective addition for the process.
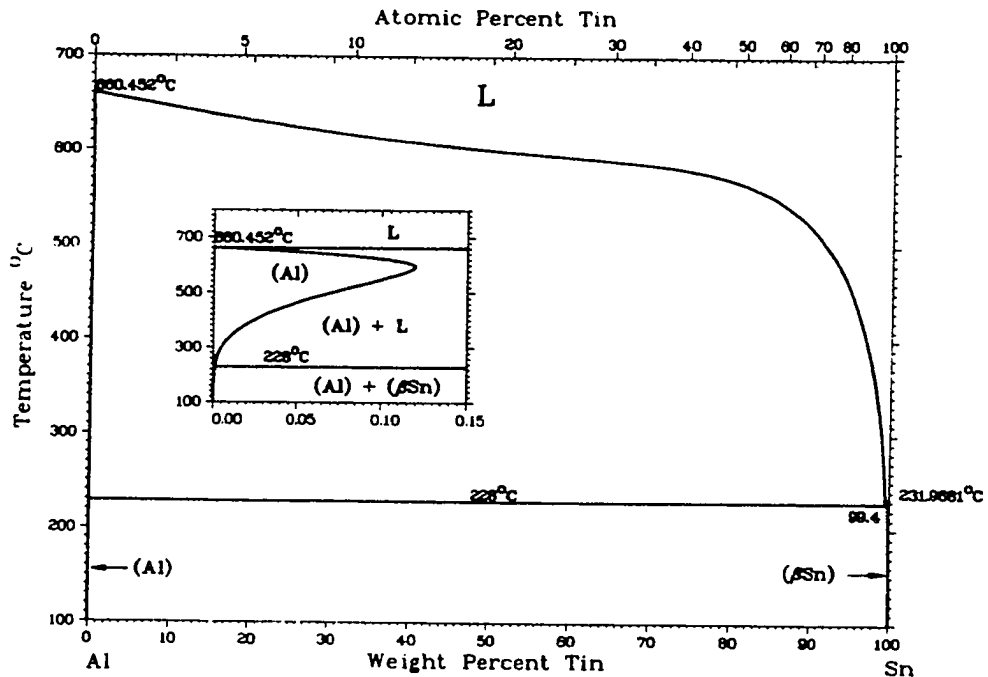
Figure 1.7 Al-Sn binary phase diagram [56].
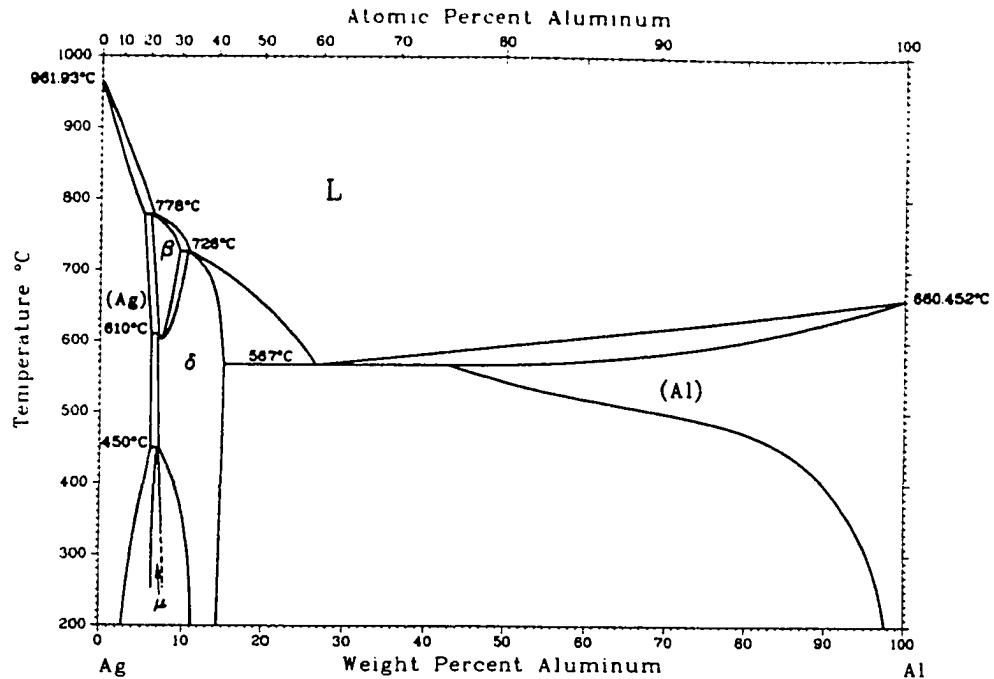
Figure 1.8 Al-Ag binary phase diagram [57].

Aside from the interactions with Al, physical properties such as vapour pressure and specific gravity must also be addressed for each element. A summary of these values is reported in Table 1.3. At a temperature of 873K Sn and Ag should have a low vapour pressure, suggesting negligible losses to volatilization. Although the vapor pressure of Li is also low, it is still appreciable (5.8×10^{-2} Torr). Therefore, a loss of Li could be experienced during sintering.

In many applications, the low specific gravity of Al (2.7 g/cc) [54] promotes it as the material of choice. Depending on the density of alloying elements, their addition to Al may affect this attribute in either a positive or a negative fashion. As shown in Table 1.3, Li may be desirable in this respect, whereas Ag and Sn may be detrimental. The magnitude of these effects depends on the concentration.

Table 1.3 Values for the physical properties relevant to alloying Al with Li, Sn and Ag [54].

Element	MP (K)	ρ (g/cc)	VP (Torr) @ 873K	SS (wt%) 873K	SS (wt%) 903K	LC (wt%) 873K	LC (wt%) 903K
Li	454	0.53	5.8×10^{-2}	4.1	3.4	7.8	5.6
Sn	505	7.3	3.0×10^{-10}	0.12	0.08	55	34
Ag	1235	10.5	4.3×10^{-8}	22.5	10.4	48	23

MP denotes melting point.   VP denotes vapor pressure.   SS denotes solid solubility. LC denotes element concentration in the liquid phase in equilibrium with the solid.

In the alloying technique developed [58-64] the desired elemental additions are used as compounds rather than as metallic forms. Such compounds may be naturally occurring minerals or commonly encountered synthetic compounds. Due to the relative abundance of each, and in the case of minerals a minimal cost of production, cost savings may also be realized. Mineralogical and synthetic forms of Li, Sn and Ag are given in Table 1.4 [65-67]. Principally, metallic Li is derived from two mineral sources (spodumene and petalite) [65]. When extracting Li from these minerals, each is first converted to lithium carbonate. Since this synthetic compound is used extensively in extractive metallurgy, ceramic and pharmaceutical industries, it is readily available.

As a source of Sn, cassiterite is the dominant mineral compound [66]. Used extensively in the extractive metallurgy industry, cassiterite and a purified synthetic version are frequently used in the electronics industry [68]. Thus, SnO_2 may also be considered to be a commonly encountered compound.

Table 1.4 Common mineralogical and synthetic sources of Li, Sn and Ag [65-67].

Element	Mineral Compound		Synthetic Compound	
	Name	Chemistry	Name	Chemistry
Li	Spodumene	$LiAlSi_2O_6$	Lithium Carbonate	Li_2CO_3
	Petalite			
Sn	Cassiterite	SnO_2	Tin Oxide	SnO_2
Ag	Silver Sulphide	AgS	Silver Nitrate	$AgNO_3$
	Silver	Ag		

Currently, Ag is used in the photographic, electronics and decorative industries, among others [67]. Although principally mined in a metallic or sulphide form, the most common compound is synthetic – silver nitrate. Because of its extensive use in the photographic industry, this nitrate is a staple of many chemical companies and can thus be purchased at a reasonable price.

1.4 2XXX SERIES AL ALLOYS

Currently, a variety of commercial aluminum alloys is available, with each alloy tailored to a specific chemistry. To organize this array of alloys, each is conveniently grouped into one of eight possible series in accordance with the principal elements added. For example, those containing Cu as the chief addition are denoted as members of the 2xxx series. Further, yet smaller, additions of elements such as Mg, Si, Mn, and Ni are also encountered. Table 1.5 lists the nominal compositions of several members of the 2xxx series.

Table 1.5 Nominal compositions of several aluminum alloys of the 2xxx series [19].

Alloy	Al	Cu	Mg	Si	Mn	Ni	Fe	Zr
2011†	Bal.	5.5	----	0.4	----	----	0.7	----
2014	Bal.	4.4	0.5	0.8	0.8	----	0.7	----
2018	Bal.	4.0	0.7	0.9	0.2	2.0	1.0	----
2024	Bal.	4.4	1.5	0.2	0.6	----	0.3	0.2

† Additional 0.4% Bi and 0.4% Pb

Similar to the 7xxx and 8xxx series alloys, those in the 2xxx series have also been engineered with the attainment of high strength as an important criterion. This is achieved through the addition of elements such as Cu and Mg [69]. During heat treatment, alloys are first heated at an appropriate temperature whereby alloying constituents are dissolved into solid solution, then quenched to room temperature. Since the solid solubility limit is significantly less at room temperature, a non-equilibrium, supersaturated solid solution results (Figure 1.9) and the alloying elements are rejected from solution as a fine dispersion of intermetallics in an attempt to reach equilibrium. The formation of such phases results in an appreciable increase in mechanical properties and is thus referred to as "age hardening."

When aging, several different precipitates may form depending on alloy chemistry. In 2xxx series alloys that contain Cu and Mg, the most plausible precipitates are θ-type ($CuAl_2$) and S-type (Al_2CuMg) in accordance with Figure 1.10 [70]. Using this figure, the Cu and Mg contents of an alloy such as 2014 (4.4 wt% Cu + 0.5 wt% Mg) imply the co-existence of both precipitates. However, since the Mg content is relatively limited, that of S-type precipitates should be as well. Consequently, it can be expected that θ-type precipitates should dominate. This behaviour has been experimentally confirmed by Gronostajski et al [71].
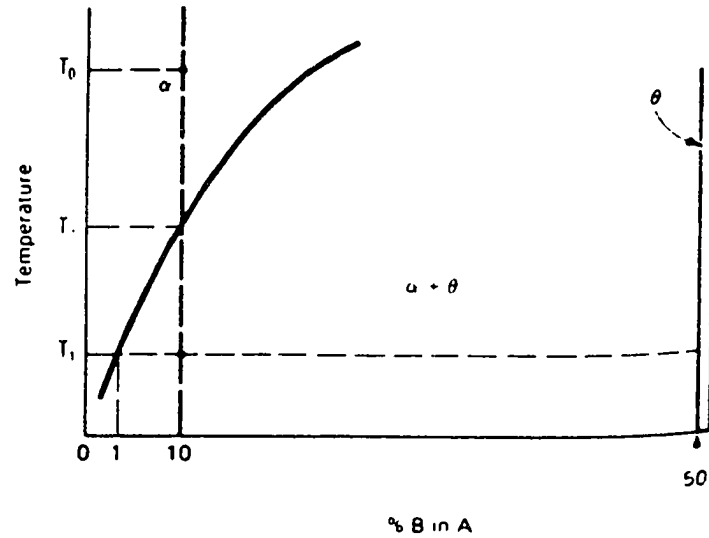
Figure 1.9 A-B phase diagram illustrating the solutionizing treatment of an A-10 % B alloy [69].
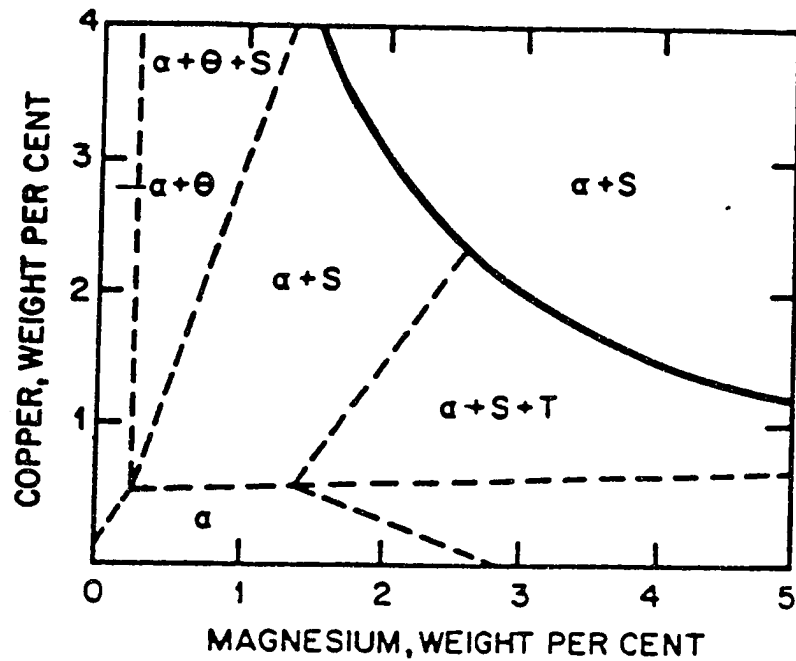
Figure 1.10 Portion of the Al-Cu-Mg phase diagram indicating the phases present at 773K (solid lines) and 463K (dashed lines) [70].

As aging progresses, the aforementioned precipitates form through the following sequence of events [72]:

Supersaturated $\longrightarrow$ GP1 $\longrightarrow$ GP2 Zones $\longrightarrow$ θ' $\longrightarrow$ θ
Solid Solution   Zones (θ'') $(CuAl_2)$

Supersaturated   GP $\longrightarrow$ S' $\longrightarrow$ S
Solid Solution   Zones $(CuMgAl_2)$
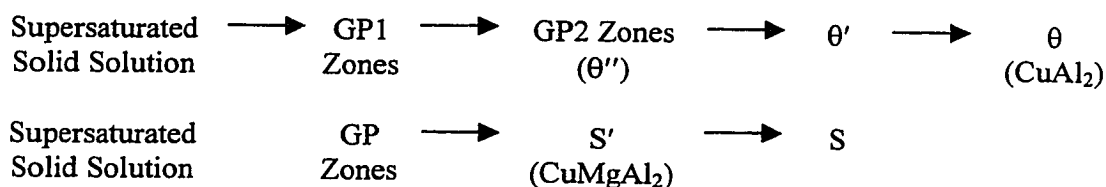
During the precipitation of θ-type precipitates, copper atoms first segregate within the supersaturated solid solution to form GP1 zones. It is believed that the disk-shaped zones have a thickness of a few atoms and a diameter of about 80 to 100 Å and that they form on the {100} planes of the matrix. Since the atomic diameter of a Cu atom is ~11% less than that of Al, the formation of GP1 zones induces strain within the surrounding matrix. Consequently, these precipitates can be studied in a transmission electron microscope, despite their fully coherent nature.

As aging progresses, GP2 zones (θ'') replace their GP1 predecessors, being larger and richer in Cu content and having a tetragonal structure with a c lattice parameter of ~7.65Å. Despite these differences, GP2 zones remain coherent with the {100} planes of the alloy matrix.

With further aging, precipitates undergo a gradual loss of coherency. Becoming semi-coherent at first, such precipitates are denoted as θ'. Although larger and tetragonal in structure, θ' has a reduced c parameter of 5.80Å. When extensively overaged, precipitates eventually become fully incoherent. Such precipitates are ordered intermetallics referred to as θ ($CuAl_2$) and have a body centered tetragonal structure. The overall sequence of θ-type precipitation as a function of aging time and hardness is given in Figure 1.11.
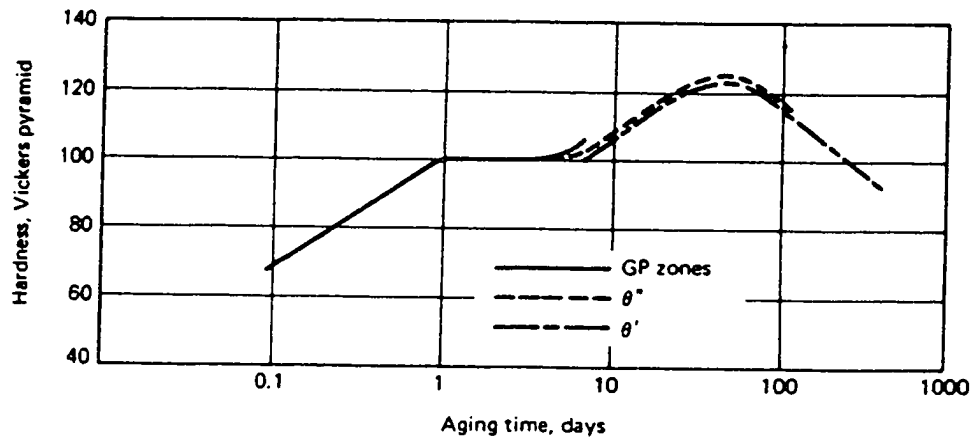
Figure 1.11 Aging curve for an Al-4wt% Cu alloy indicating the sequence of precipitation when aged at 403K [69].

In Al-Cu-Mg alloys that have a low Cu:Mg ratio, the precipitation of S-type intermetallics is commonly encountered. As previously shown, the aging sequence begins with the formation of GP zones that consist of Cu and Mg atoms collected on {110}$_{Al}$ planes. Metastable and incoherent S' then forms on {210}$_{Al}$ planes growing as laths in the <100> direction. Finally, the sequence concludes with the formation of the equilibrium variant of S precipitates.

In the heat treatment of commercial Al alloys, supersaturated solid solutions are typically aged at room temperature (natural aging) or at a moderately elevated one (artificial aging). The former is designated as T4, whereas the latter is designated as T6. Although aging can occur at room temperature, the kinetics of precipitation can be quite slow. To circumvent this difficulty, artificial aging at moderate temperatures (i.e. 423 to 473K) is usually utilized. Consequently, the rate of precipitation is improved and peak hardness is achieved within a reasonable period of time. Several aging curves for AA2014 are illustrated in Figure 1.12 [75]; when aged at 433K, peak hardness is attained

after approximately 18h. Tensile properties for several 2xxx series alloys in the T6 condition are also given in Table 1.6 [76].

With respect to corrosion resistance, many aluminum alloys perform exceptionally well in a variety of operating environments. Relatively speaking, alloys in the 1xxx series (relatively pure Al) offer the best resistance, whereas those in the 2xxx offer the poorest [77]. The rankings of several alloys immersed in a NaCl solution are given in Table 1.7.
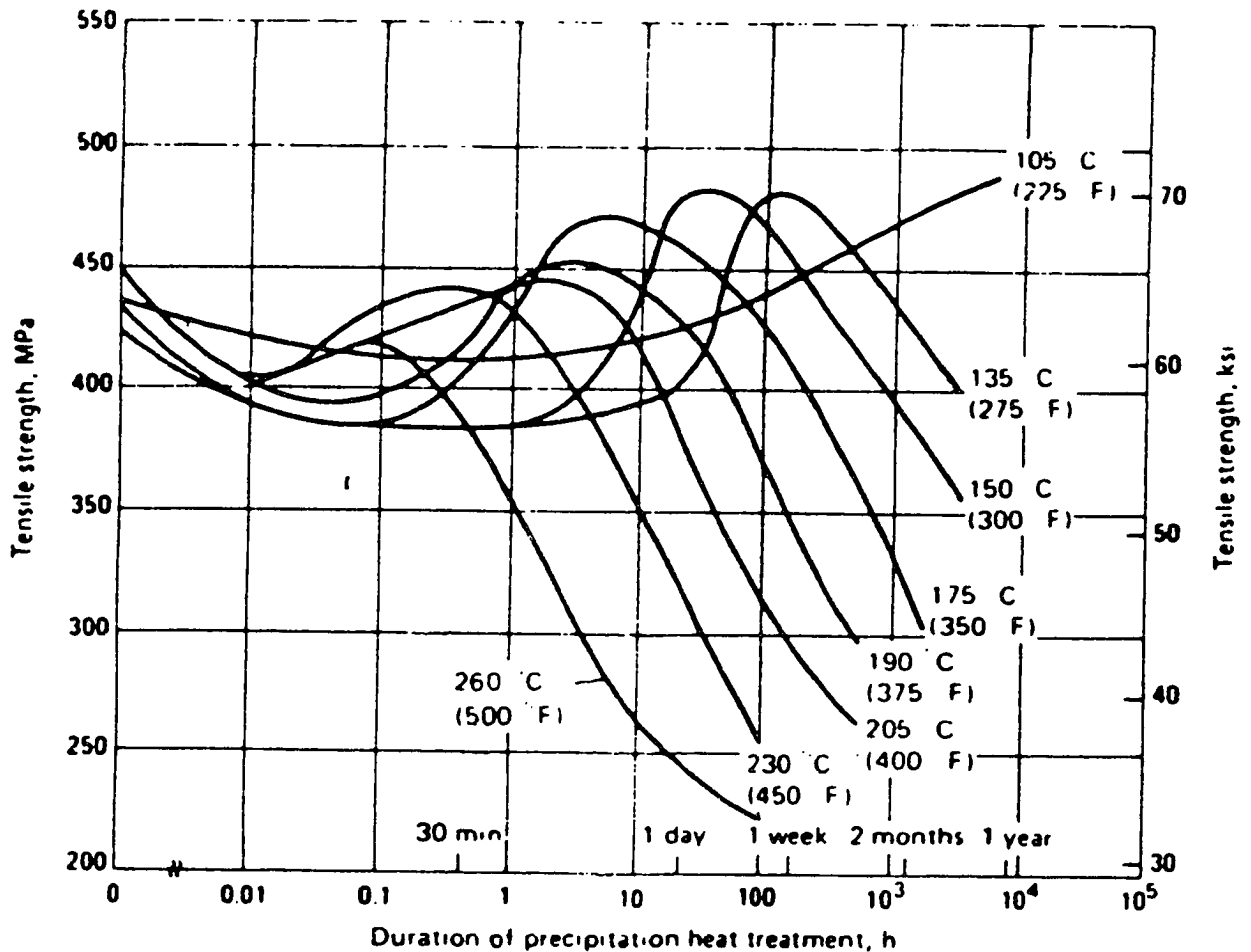
Figure 1.12 Artificial aging curves for AA2014 [75].

Table 1.6 Mechanical properties of several 2xxx series alloys in the T6 condition [76].

Alloy	Yield Strength (MPa)	Ultimate Tensile Strength (MPa)	Elongation to Failure (%)
2014	415	485	13
2018	315	420	12
2024	393	475	10

Table 1.7 Relative ratings of resistance to general corrosion for several aluminum alloys when immersed in a NaCl solution [77].

Alloy	Temper	Corrosion Resistance	Alloy	Temper	Corrosion Resistance
1060	All	A	3003	All	A
1100	All	A	3105	All	A
1350	All	A	5050	All	A
2011	T4	D	6061	T6	B
2014	T6	D	7075	T6	C
2024	T6	D	7178	T6	C

Alloys with A and B ratings can be used in industrial and seacoast atmospheres without protection. Alloys with C, D and E ratings generally should be protected, at least on faying surfaces.

Unlike all other alloy series, it is only those of the 2xxx type that contain Cu as the primary alloying addition. When such alloys corrode, Cu ions that initially go into solution are replated onto the alloy to form minute metallic Cu cathodes, thus forming galvanic cells. Through the reduction of Cu ions and the increased efficiency of O_2 and H^+ reduction in the presence of Cu, the corrosion rate is increased.

Aside from the principal elements that are contained in commercial aluminum alloys, many also contain Pb, Bi, Ni or Sn. Each element tends to form distinct constituent phases within the microstructure due to a limited solid solubility in Al. Since these phases are cathodic to the matrix component, a net decrease in the resistance to corrosion in aqueous saline media results [77-81]. Thus, the applications of such alloys are restricted to those wherein corrosion is of limited concern, otherwise the alloys must be cladded. Although this behaviour can be problematic in certain instances, it can also be advantageous in others. This is particularly true in the case of Al-Sn binary alloys that have found use as efficient sacrificial anodes [78,79].

Although aluminum alloys are noted for their exceptionally high strength to weight ratio, corrosion resistance and formability, they generally exhibit poor resistance to wear [82]. For this reason, many studies have been devoted towards an understanding of the respective phenomena [83-85]. Regardless of the aluminum alloy considered, each is known to exhibit two general types of wear – mild and severe [83]. To determine which mechanism is operative requires extensive experimentation and an assessment of the resultant surface damage. Severe wear typically results in a significant amount of surface damage and a massive transfer of material from the test block to the counterface. In contrast, mild wear generates a worn surface covered in tribological layers and less extensive damage. Due to an increasing extent of surface damage from mild to severe wear, a corresponding increase in the wear rate results. When plotting wear rate vs. applied load, the transition from mild to severe wear is manifested as an abrupt change in slope (Figure 1.13).

To enhance the wear resistance of aluminum numerous methods have been considered. In all of the cases reviewed, each relied on the incorporation of a secondary component or phase in to an aluminum matrix. Such components can be hard, abrasive ceramic materials [86,87] or a soft material such as Sn [88,89], graphite [90,91] or Pb [92].
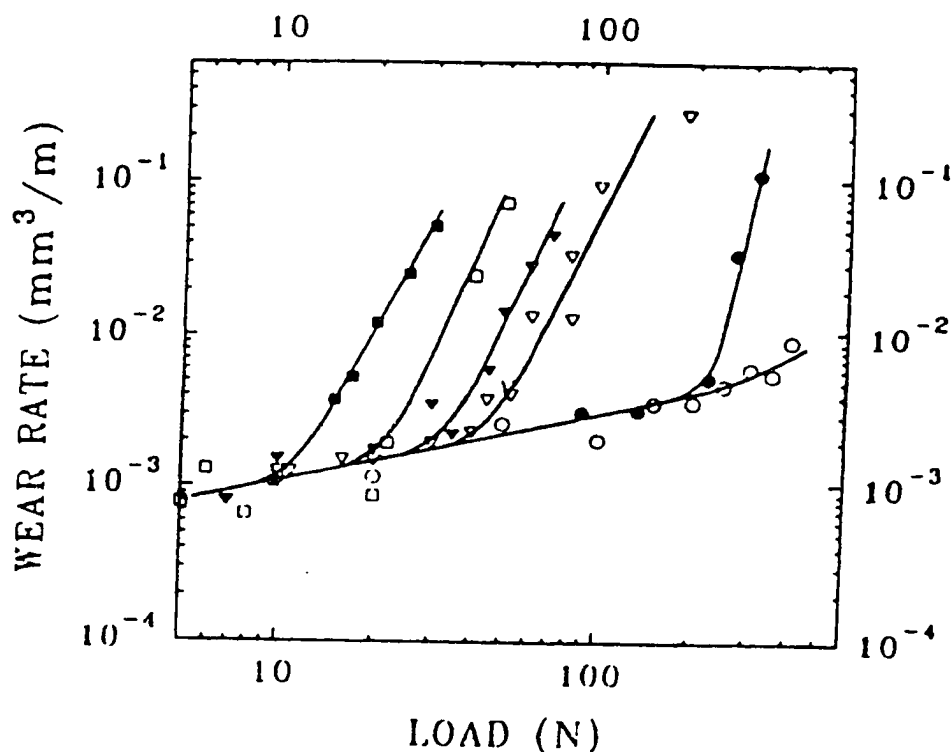
Figure 1.13 Plots of wear rate vs. applied load for Al alloy 6061 measured at different sliding velocities: (O) 0.2 ms^{-1}, (●) 0.4 ms^{-1}, (∇) 0.8 ms^{-1}, (▼) 1.2 ms^{-1}, (□) 2.0 ms^{-1}, (■) 5.0 ms^{-1} [83].

Several Al-Sn bearing alloys have been developed (Table 1.8) which incorporate Sn into an Al alloy base. Typically, the Sn contents of such alloys range from 5 to 20 wt% [93]. Since these amounts are well in excess of the solid solubility limit of Sn in Al (~0.05 wt%), the resulting microstructure contains intergranular regions comprised essentially pure Sn [88,89]. The Sn, being a soft, low melting point metal is readily melted when mated in a rolling/sliding fashion against another metallic surface. The melted Sn subsequently restricts direct metal to metal contact thus reducing friction and in turn, scoring and bearing wear [89]. Thus, although such alloys tend to be soft and of low tensile strength, they have found use as bearing materials [93].

Table 1.8 Nominal compositions of some bearing alloys based on the Al-Sn system [93].

Alloy	Al	Sn	Cu	Si	Ni	Fe	Ti
8081	Bal.	20.0	1.0	0.7	----	0.7	0.1
8280	Bal.	6.3	1.0	1.5	0.5	0.7	0.1

1.5 POWDER METALLURGY PROCESSING

By definition, powder metallurgy (P/M) is *"the art of producing metal powders and utilizing metal powders for production of massive materials and shaped objects"* [94]. Using such practices, an extensive array of alloy systems is used to produce an even greater variety of components. Alloy systems of considerable interest include Fe alloys [95,96], Cu alloys [95], Al alloys [95,97-104], Ni alloys [95] and refractory metals such as W [95,105]. In the application of P/M to Fe, Cu and Ni-based alloys, cost reduction as opposed to an increase in mechanical properties is the main driving force. With Al alloys, however, the principal interest is an improvement in mechanical properties [101]. Currently, substantial research efforts continue for all of these systems. However, further discussion will focus principally on Al alloys.

The study of Al powder metallurgy began in the 1940s, and the first commercially viable process for the production of structural parts was developed in 1962 [97]. From these early beginnings, an interest in the application of this alloy system into P/M practices has risen steadily. This progression has been driven by the advantages P/M processing offers over that of ingot metallurgy (I/M). Such advantages are numerous and will be addressed individually.

Several advantages stem from the usage of atomization and its inherently high solidification rate, to produce alloy powder. By generating powder in this manner, a

significantly finer dendrite cell size, finer constituent particles and less insoluble and undissolved constituent results in the solidified structure [95, 100, 101]. Since the molten metal undergoes rapid solidification, solid solubility limits can be extended, yielding larger volume fractions of fine precipitates and/or the formation of metastable phases that would not normally occur. This benefit is particularly advantageous since so few elements exhibit an appreciable solid solubility in Al under equilibrium conditions. Through these microstructural refinements, P/M products generally exhibit mechanical properties that are superior to the I/M equivalents.

During atomization of Al alloy powders a thin oxide layer is formed on the particles. Unlike metals such as Ti, the oxide form of Al is not soluble in the molten metal. Consequently, the oxide persists through to the final product. This oxide can reduce sintering rates and/or serve as a reinforcing agent of sorts. The latter frequently results in improved mechanical properties. In studies of stress corrosion cracking (SCC) it has been found that the presence of oxide particles along grain boundaries can be beneficial (Figure 1.14) [100]. It is believed that the oxide may cause a shift to a more alkaline condition in the environment at the crack front thereby slowing the rate of attack.

Aside from the advantages related to atomization, several others are also inherent in the consolidation practices. Perhaps the greatest benefit in this regard is an ability to produce near net shapes. By producing components with dimensions that approach those desired in the final product, the amount of machining, forging and material loss are reduced considerably. Consequently, the extent of anisotropic texture is also reduced.
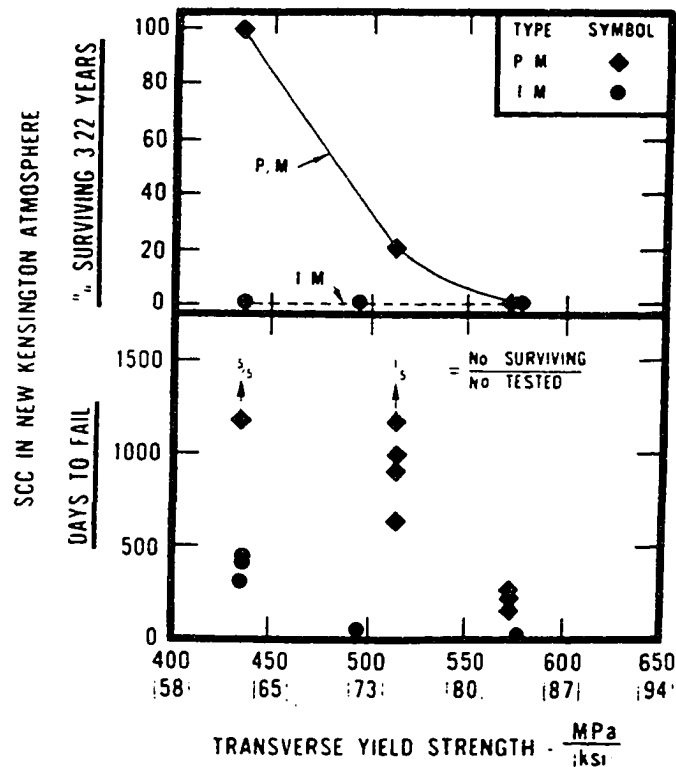
Figure 1.14   Comparison of SCC in an Al-Zn-Mg P/M alloy and an equivalent I/M counterpart [100].

For P/M products which require machining, the existence of a fine grain size can significantly improve machinability. When machining wrought Al alloys, long stringers of awkward material can result. However, when working with an equivalent P/M alloy, machining chips are considerably shorter. Handling such particles becomes less cumbersome and reduces the risk to machinists [95]. Additional advantages of the consolidation practices include the production of intricately shaped parts at a high volume rate and an ability to consolidate refractory metals.

Despite the array of advantages offered by P/M, several disadvantages may surface. Of chief concern is the cost associated with the equipment used for powder production and consolidation. Such machinery is often complicated and specific to the

P/M industry, thus increasing the costs associated with initial purchase and maintenance. Furthermore, due to the practical limits of equipment size, most components produced through P/M are small. The presence of residual porosity in P/M parts can also be problematic and difficult to avoid. In some instances, however, porosity is desirable such as in components used as filters or thermal barriers.

Through diligent research and development efforts, many of the early problems associated with P/M have been overcome. At present, P/M is an industrially accepted means of manufacturing metallic components, with worldwide production facilities. Thus, the number and variety of P/M applications is ever increasing. For Al-based alloys, P/M is currently used to produce parts for the automotive, appliance, aerospace, nuclear, medical, military and farm equipment industries. Components can range from small gears and connecting rods to large load bearing structures.

Recently, an economic study of the P/M industry has been completed [106]. In this report a tremendous surge in growth is revealed with powder shipments of Fe and Al-based alloys reaching record levels. Principally, this expansion was attributed to the increased usage of P/M in automotive applications. To manufacture certain powertrain parts, connecting rods and bearing caps, stainless steel is used, whereas Al alloys are used in engine cam caps and air conditioning compressor parts. Many new applications are presently in the design and tooling stage particularly for Al. At present, there are more P/M parts in automobiles than Zn and Mg cast/wrought components combined. To further the usage of P/M in the automotive as well as other industries, spin off developments in stainless steel and Al P/M have occurred in the fields of warm compaction and metal injection molding.

To this point, many of the fundamental basics of P/M have been reviewed in a general discussion. However, details pertinent to powder production, consolidation and sintering are particularly important and are thus outlined in the following sections.

1.5.1   Powder Production

To produce any component by powder metallurgy (P/M) techniques, an obvious requirement is the production of metal or alloy powder. Currently, a variety of methods can be employed in this regard, each producing metal powder with distinct characteristics. The four methods principally used include:

    a) Chemical Reactions or Decomposition

    b) Electrolytic Deposition

    c) Mechanical Processing

    d) Atomization

The selection of the most appropriate method requires the consideration of several factors. Of great concern is the P/M route to be utilized, since the properties and characteristics of a powder can be reflected to different extents in the final product. As with any engineering application, economic considerations must also be addressed to ensure that the producer and consumer can function in a profitable manner. Furthermore, the purity demanded by the consumer must be taken into account, especially when stringent attention to composition is required.

In the production of powdered metal by chemical reaction [107, 108], a variety of methods is currently in use. For this reason, such reactions are sorted into one of two possible categories – decomposition of solid phases and precipitation from aqueous solution. When using the former, the starting form of the desired metal is typically that of an oxide. The usage of oxides is justified by low production costs, high purity and the ease of handling. Initially, the oxides are heated to a temperature that is below the melting point of both the oxide and metallic form of the given element. After a short isothermal hold, a reducing agent is then introduced into the system. Since the reducing agent (typically solid carbon, or gases of either H_2 or CO) has a greater thermodynamic affinity for the non-metallic element(s) of the compound, such elements are removed as a gaseous product.

When using a gas as the reducing agent, several key stages occur during the reaction between it and the compound to be reduced. These stages include:

1) Convection within bulk gas atmosphere,

2) Diffusion of reactant gas through the surrounding boundary layer,

3) Adsorption of gas onto the surface of compound particles,

4) Reaction between the gas and compound,

5) Desorption of gaseous reaction products from the surface of the solid reaction products,

6) Diffusion of the product gas through the boundary layer, and

7) Convection of product gases through bulk atmosphere.

Careful consideration of all stages is often critical, since any stage may be rate controlling, thus influencing kinetics and in turn, the economics of the process. After processing by this means, the final metallic product is in a hard spongy form that is subsequently ground into a fine powder.

When selecting a process, the advantages and disadvantages must be weighed carefully. The production of metallic powders by chemical reactions is advantageous for several reasons including:

1) The cost of the process can be low when inexpensive solid carbon is used as the reducing agent.

2) The resultant powder particle size can be controlled.

3) Powders that are both porous and easily compressible can be produced.

4) Operations can be carried out in a continuous or a batch type manner.

Despite these advantages, several disadvantages are also inherent in the process:

1) The process can be costly when pure reducing gases are utilized.

2) Large volumes of reducing gases are required together with the associate safety considerations.

3) Resultant powders are not refined and may contain impurities.

4) A very limited selection of alloy powders is producible.

The second method of producing metal powders through chemical reactions is precipitation from aqueous solutions. In this process, the desired metal is first acquired as a water-soluble salt. Once added to water, the desired metal ions are thus forced into solution. To reduce these ions into a metallic, powder form, a reducing agent is then introduced into the system. Those most frequently encountered include H_2 gas or an appropriate solid metal. Provided that the reducing agent is less noble than the metal ions in solution, a net transfer of electrons from the reducing agent to the metal ions in solution will occur, thereby reducing such ions into solid metal powder. Such precipitation processes are utilized extensively in the hydrometallurgical industry. Examples of this application include the precipitation of Cu from solution using Fe, the precipitation of Cu, Ni and Co using H_2 gas and the reduction of Au ions using Zn. Advantages of precipitation-type processes include low cost and the need for a minimal amount of operating equipment. Disadvantages, however, include the susceptibility of powders to oxidation, a minimal amount of flexibility associated with powder characteristics and the inability to produce alloy and reactive metal powders.

As mentioned earlier, another means of producing powders is through electrolytic deposition [107,109], wherein an electrochemical cell is employed. The basic components of the cell include an anode, cathode, electrolyte and a current source. As is the case in chemical reaction processes, the desired metal begins as a compound that is dissolved into solution (the electrolyte). Typically, the electrolyte is either a solution or fused salt mixture. Through the application of a potential between the anode and cathode,

the metal ions in solution are reduced to solid metal at the cathode. The resulting deposit generally exhibits a dendritic fern-like morphology of low apparent density. Once removed from the cathode, the deposit is then ground into a fine powder.

In order to produce powders with specific characteristics (e.g. morphology or size distribution), extensive knowledge of all process variables and their influence on the final product is required. Of these variables, current density is typically the most important. By varying this parameter, the process can directly yield powder, or a final deposit that can be hard and brittle or soft and spongy. Another important variable is the material and condition of the cathode. An essential criterion is that the cathode must be highly polished and made of a material that will ensure and facilitate the complete removal of all of the desired metal. Additional variables to consider include temperature, composition and circulation of the electrolyte as well as the size and arrangement of electrodes.

Advantages of electrolytic deposition include the deposition of high purity powder, the variation in powder characteristics that can be achieved, an ability to control the physical properties of the final powder and the feasibility of using the resultant powder in powder metallurgy practices. Conversely, the process suffers from a difficulty to produce alloy and reactive metal powders, the need to clean powders after processing and the active nature of the product which renders it highly susceptible to oxidation.

As an alternative to the two previously mentioned techniques, metal powders can be produced by mechanical processing [110]. In this procedure, the metal first exists as blocks or ingots that are ground into fine particles. Despite the inherent ability to produce alloy powders and obviously low equipment costs, the characteristics of the final powder render them useless for most powder metallurgy practices. Therefore, this technique is used only in select instances such as the pulverization of metallic sponges or friable metals/alloys.

Of all the processes previously discussed, atomization is by far the process of choice [108-111]. The atomization process begins by melting the desired metal or alloy. The molten metal is then held in a refractory crucible and allowed to flow through a small orifice. Typically, an orifice is designed to ensure that a high level of turbulence is induced into the molten stream. As this stream exits the reservoir, it is instantly disintegrated by jets of high-pressure gas or water. During disintegration, the stream is first broken up into ligaments. Such ligaments are then drawn into particles due to surface tension forces. Depending on the length of time that the ligament remains molten, the resulting particles may be irregular or spherical shaped. Final particles then fall to the bottom of the equipment where they are cooled and collected.

One of the most dominant advantages of atomization is the ability to produce powders of virtually any alloy that can be melted. When producing alloy powders, the situation becomes slightly more complicated than that associated with pure metals. Consequently, additional processing factors that are addressed include:

a) For alloys having a broad temperature gap between the solidus and liquidus for a particular composition, larger drops take longer to freeze and tend to develop a more irregular shape than those produced from smaller drops.

b) Significant segregation can occur within the final particles. This is manifested on a microstructural scale as an outer skin of relatively high melting point phases surrounding a core of lower melting point ones.

c) The gases used for rapid cooling may become entrapped and produce hollow particles.

d) Due to the high cooling rates experienced, high hardness levels are frequently developed in the final powder. In some instances, the hardness is sufficiently high to render the powder unsuitable for powder metallurgy practices unless it is annealed first.

1.5.2 Powder Compaction

Once the required metal or alloy is processed into a powder form, it must then be compacted. Several P/M practices are possible and include (i) cold isostatic pressing [112], (ii) hot isostatic pressing [113], (iii) metal injection molding [114], (iv) the Ceracon process [115], and spray deposition [116]. Due to its relevance to the present investigation, only cold isostatic pressing will be outlined.

In original cold pressing practices, metal powders were consolidated using steel dies and axial pressure. Consequently, considerable density gradients existed within the pressed green body and eventually, sintered bodies. To circumvent this quality issue, cold isostatic presses (CIPs) were developed [112]. Pressing in this manner can be conducted in two principal means – wet bag and dry bag. In wet bag pressing, metal powder is first loaded into a rubber mold that is sealed once filled. The sealed tooling is then loaded into the pressure vessel of the CIP (Figure 1.15) that is then filled with a pressure medium, typically water. The pressure within the vessel is then raised to values that generally range from 50 to 400 MPa. By pressing in this manner, the tooling is pressed isostatically rather than axially as in conventional die pressing. Consequently, density gradients within the green bodies are minimized. After dwelling at pressure for a desired period of time, the vessel is depressurized and the tooling removed. The porous product is referred to as a green body.

Although dry bag pressing also yields a porous green body that must be sintered, the technique of producing it is slightly different. In this process, the rubber mold is actually fixed to the inside of the pressure vessel. Once the mold is filled with powder, pressure is applied by introducing pressurized oil between the mold and pressure vessel wall. As with wet bag processing, pressure is maintained for a given period of time, and eventually the green body is removed.
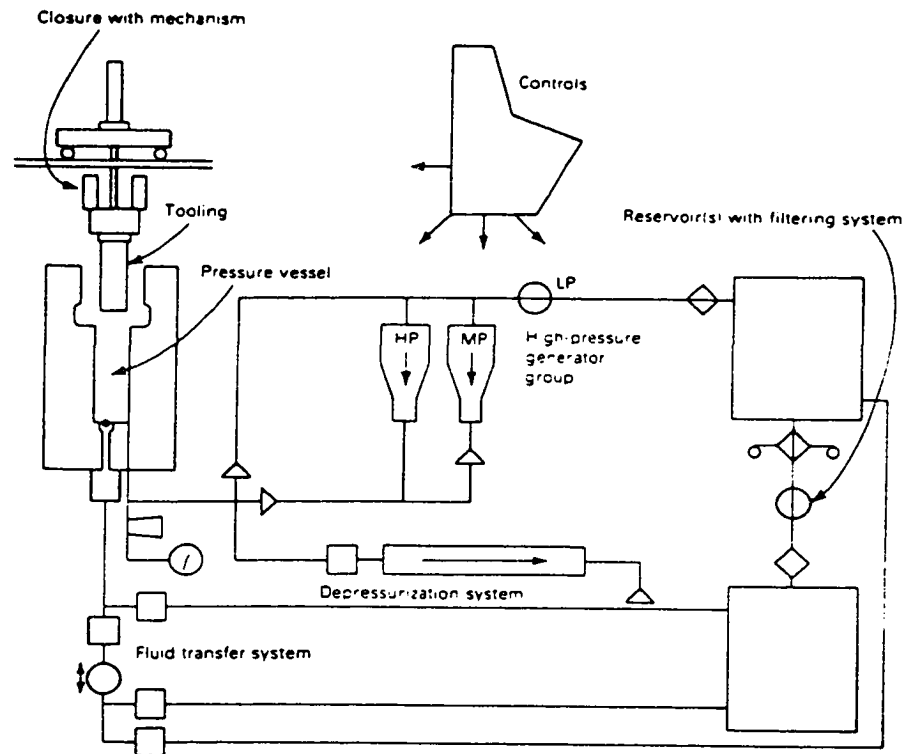
Figure 1.15 Schematic illustration of a cold isostatic press [112].

1.5.3 Sintering

For industries that utilize powdered materials, the compaction of powder into green bodies is followed by sintering [117-123]. When sintering reactive metals such as Al, an essential consideration is the surrounding atmosphere. To avoid any deleterious reactions with oxygen that may impede densification, inert (N_2 or Ar) or reducing atmospheres (dissociated ammonia) are frequently employed. In many instances, green bodies are first heated to an intermediate temperature to facilitate lubricant burn off and/or degassing. Afterwards, the component is further heated to the final sintering

temperature where it is isothermally held for times ranging from several minutes to hours, depending on the alloy of interest. The sintered product is then cooled to room temperature and if required, subjected to post sintering operations such as swaging, machining, forging, and extrusion. A typical sintering profile for an Al-4.4Cu-0.8Si-0.5Mg alloy (A201) is given in Figure 1.16.

Sintering is performed either at a sub-solidus temperature (solid state sintering) or at one that is intermediate between the solidus and liquidus (liquid phase sintering). When sintering elemental powders, solid state sintering (SSS) is typically the standard practice [119]. It is commonly accepted that SSS occurs in several stages [119,120]:

i)   Development of necks between particles,

ii)   Formation of a continuous network of pores and solids,

iii)   Formation of closed, isolated pores.

At each stage, mass transfer by diffusion is the dominant mechanism; thus, the rate of sintering is strongly temperature and time dependent. Aside from these variables, additional factors of concern include the initial particle size distribution, alloy composition, milling practices to reduce agglomerates, and sintering atmosphere as well as temperature and green density gradients.

In mathematical models of sintering, the process is often simplified by assuming spherical powder particles. A common model for the initial stage of sintering is the two-sphere model (Figure 1.17). When green bodies are pressed, particles are forced into intimate, point contact that results in strain hardening. At the point of contact or neck, a small radius of curvature exists relative to that representing the bulk particle. Consequently, a larger concentration of vacancies exists in the contact region. In response to this vacancy gradient, thermodynamics dictates that a flux of vacancies from the narrow contact region to the particle bulk shall result. This is equivalent to a migration of atoms in the opposite direction (towards the neck).
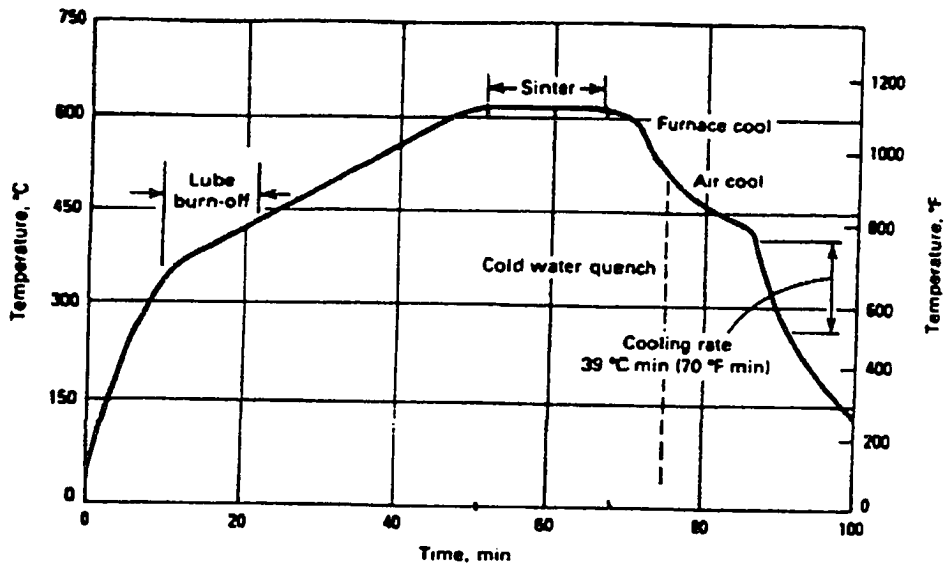
Figure 1.16 Typical sintering profile for Al P/M alloy 201A [117].

Such mass transport by diffusion can occur by two means – volume diffusion and surface diffusion. In Figure 1.17(b), the former is shown as path a, whereas the latter is shown as path b. Although these diffusional flows result in pore rounding and spherodization, they do not explain net compact shrinkage (reduction of the center to center distance between particles).

To account for shrinkage, diffusion along and near the grain boundary that forms at the particle contact must be considered. This is shown in Figure 1.17(b) as grain boundary diffusion (path c) and bulk diffusion (path d). When atoms flow from the grain boundary to the neck, vacancies flow in the opposite direction. Since vacancies are eliminated at the grain boundary, the two particle centers approach each other and shrinkage results. As sintering progresses, the stages (ii) and (iii) occur yielding a final product of improved density and mechanical properties.
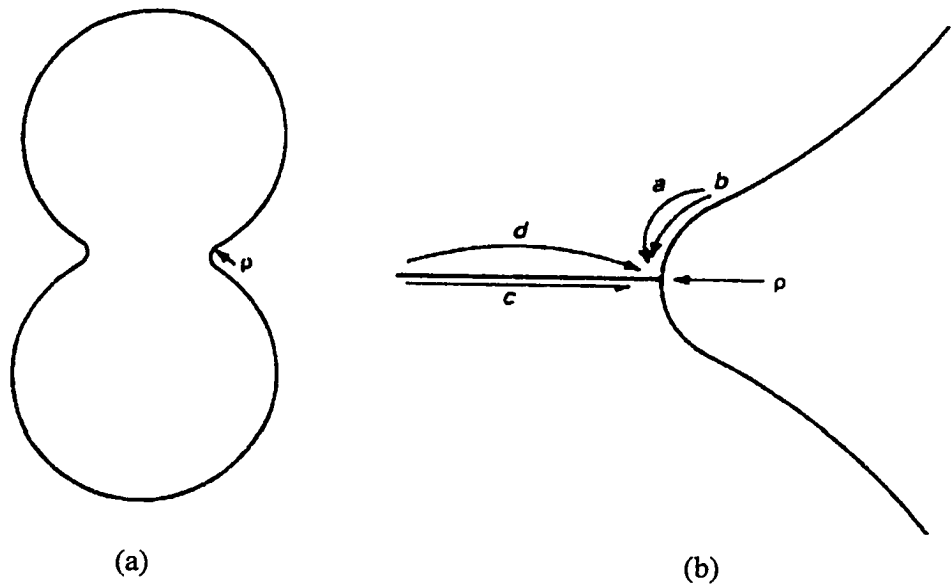
Figure 1.17 Schematic illustration of the two sphere sintering model. (a) Two spheres sintering , (b) material transfer that occurs during sintering [119]. The radius of curvature in each case is designated as ρ.

In many instances within the P/M industry, liquid phase sintering (LPS) is the preferred consolidation practice. Currently, LPS is used extensively with refractory metals such as W [119], reactive metals such as Al [97, 119], prealloyed powders [118] and composite materials [122]. The product of LPS is typically denser and of greater homogeneity than that produced by SSS. Thus, in applications where mechanical, electrical, or magnetic properties are of concern, LPS is generally employed.

Frequently, LPS is used in the consolidation of blended mixtures of elemental powders. When compacts of such mixtures are heated, one of the elements melts. Consequently, a liquid, and in turn capillary force, is developed between the adjacent, more refractory particles. Provided the particle size is small (<1 μm) the magnitude of

this force is sufficient to enhance densification. As the liquid flows, it wets the solid particles promoting rearrangement and densification.

Since the solid and liquid phases of the sintering system are in intimate contact, interaction between them results. With continued heating, the solid phase begins to dissolve in the liquid. As the concentration within the liquid increases, another solidus boundary may be crossed depending on the alloy composition and the applicable phase diagram. By crossing such a boundary, partial solidification of the liquid may result. This process is illustrated in the idealized phase diagram given in Figure 1.18. However, since powder atomization is a process that is far disturbed from equilibrium conditions, accurate predictions require the use of metastable phase diagrams.
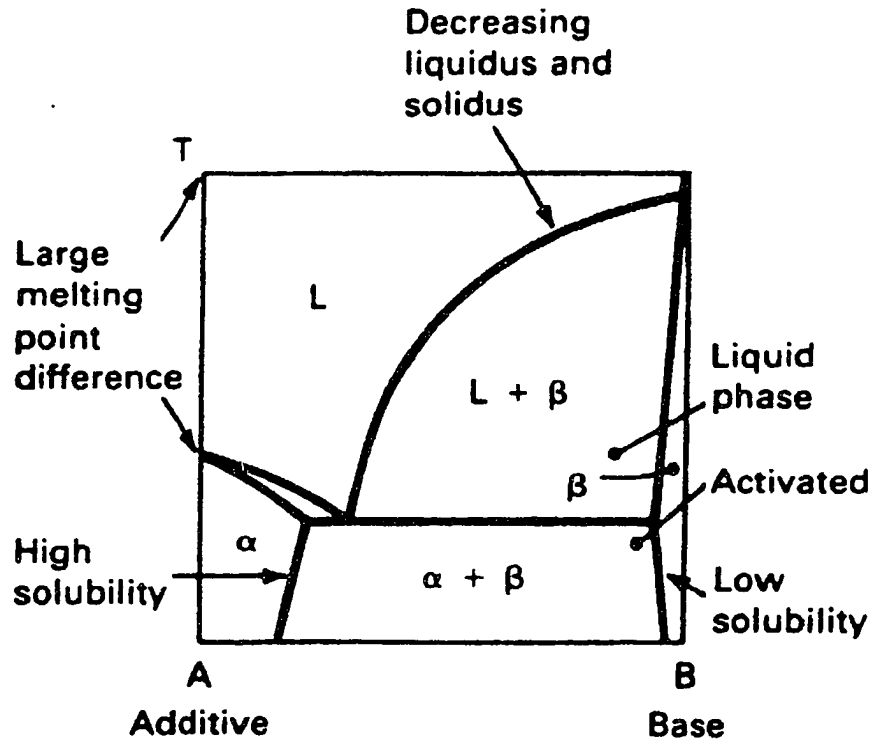
Figure 1.18 Idealized phase diagram showing enhanced conditions for liquid phase sintering [119].

Although LPS of elemental powders is a common practice, it is also used extensively for those that are prealloyed [118]. Such alloy powders are currently produced from many alloy systems including those based on Al, Fe, Ni, and Cu. When sintering these powders, green compacts are first heated to a temperature intermediate between that of the solidus and liquidus. Sintering in this manner is referred to as supersolidus liquid phase sintering (SLPS).

An important criterion in SLPS is the amount of liquid present. Although a greater amount of liquid results in a lower viscosity and in turn increased sintering rate, distortion of the compacts is also increased. Therefore, a balance between these factors must be acquired to optimize processing. Typically, the optimum combination of sintering rate and distortion is achieved when the liquid content ranges between 10 and 40%. To predict an appropriate sintering temperature for a given alloy system, phase diagrams can prove very useful. This is illustrated in Figure 1.19 for the case of an Al-4wt% Cu alloy. By applying the lever rule to several temperatures within the mushy zone (solid + liquid regime) the variation of solid and liquid content can be calculated (Table 1.9). From these data, it appears that SLPS should be facilitated in the range of 873 K to 908 K for this system. Given that a sintering temperature of 873K is intermediate between the liquidus and solidus temperatures of aluminum alloy 2014 [19] the sintering regime in SLPS.

On a microscopic scale, liquid forms at necks between particles, along the internal grain boundaries of particles and at pockets located inside the grains. The liquid at particle necks provides a capillary force to promote densification, whereas that along grain boundaries induces grain sliding. With prolonged isothermal holding, equilibrium is eventually approached, and the microstructure progresses from one of discernable powder particles and interconnected porosity, to a homogenous mixture of liquid and solid phases together with closed isolated pores (Figure 1.20).
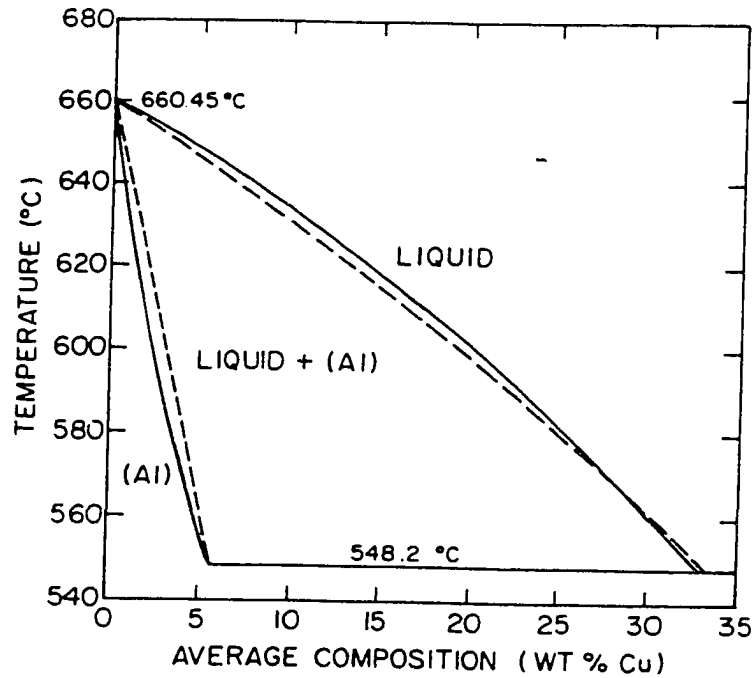
Figure 1.19 Al rich portion of the Al-Cu phase diagram [123].

Table 1.9 Variation in the composition and amount of solid and liquid present as a function of temperature for a Al-4wt% Cu alloy. Data extracted from Figure 1.29 [123].

Temperature (K)	Solid Composition (wt%)	Liquid Composition (wt%)	Amount of Liquid (wt%)
844	Al + 4.0wt% Cu	----------	0
853	Al + 3.3 wt% Cu	Al + 24.4 wt% Cu	3.3
863	Al + 2.7 wt% Cu	Al + 23.0 wt% Cu	6.5
873	Al + 2.1 wt% Cu	Al + 20.3 wt% Cu	9.7
883	Al + 1.7 wt% Cu	Al + 17.5 wt% Cu	14.8
893	Al + 1.3 wt% Cu	Al + 14.3 wt% Cu	20.0
903	Al + 0.9 wt% Cu	Al + 11.3 wt% Cu	30.6
913	Al + 0.6 wt% Cu	Al + 7.9 wt% Cu	50.0
925	----------	Al + 4.0 wt% Cu	100.0
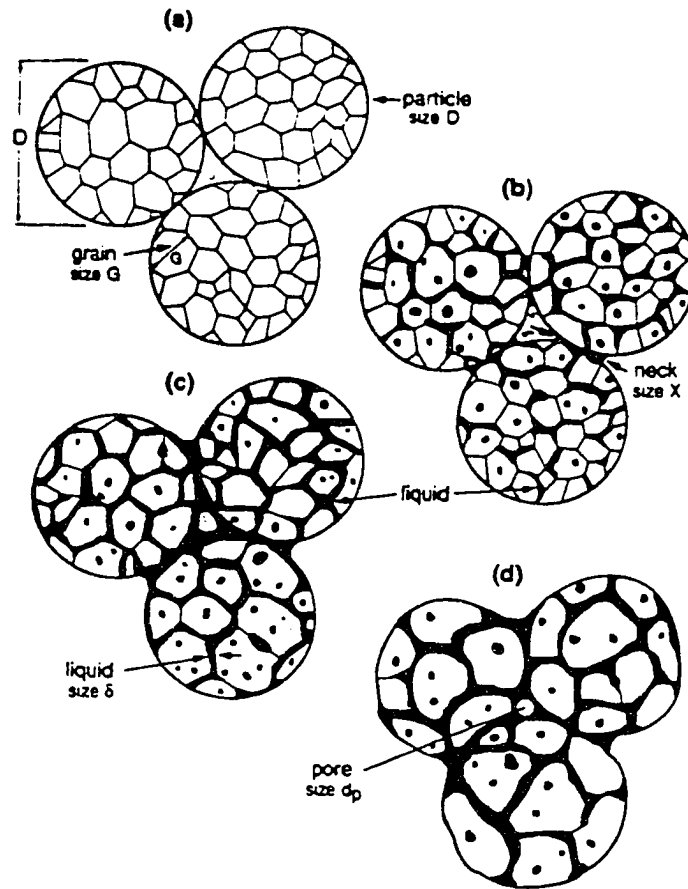
Figure 1.20 Illustration of the events that occur during LPS of three prealloyed powder particles: (a) initial particle packing, (b) formation of initial liquid with insufficient wetting of grain boundaries for densification, (c) viscous flow densification of semisolid particles, and (d) final stage densification with closed, spherical pores [118].

When compared to traditional LPS, SLPS has several advantages. In LPS, powder particles <1µm in size are required. Although this demand can be met, the typical industrial atomization facility produces metal powder with a particle size ranging from 20 to 250 µm. Due to this relatively coarse nature, such powder is unsuitable for traditional LPS, however, it proves ideal for SLPS. Furthermore, the high density and homogenous

microstructure of SLPS products result in improved mechanical properties over those produced by LPS. To take full advantage of this trait, sintering time should be minimized to reduce microstructural coarsening.

1.6 ALLOYING TECHNIQUES

Currently, two principal means are available for introducing alloying additions into aluminum – ingot metallurgy and diffusion-based alloying based on P/M. Each of these techniques is discussed in the following sections.

1.6.1 Ingot Metallurgy

The most common method currently used to add alloying additions to Al is ingot metallurgy (I/M) [72,124]. Typically, the process begins by charging furnaces with large ingots of electrolytic Al and frequently scrap. Once the charge is melted in a refractory lined ladle, the desired alloying elements are then added. Although this concept may seem simplistic, the cost associated with it is substantial. Due to the price of raw materials, yield losses, production costs associated with dissolution times, inventory, and handling, the total cost of alloying amounts to more than 2 billion dollars annually to the worldwide Al industry. Depending on the alloy and efficiency of production, this can range from 30 to 300 $/t.

As previously mentioned, Al can be alloyed on both a macro (1 to 10 wt%) and/or micro (<0.5 wt%) scale. Regardless of the extent of alloying, ensuring that the element is homogeneously distributed throughout the entire melt can be difficult. This becomes exceptionally problematic when microalloying. To enhance homogeneity, elements are added in the form of master alloys rather than that of the pure metal.

In general, master alloys are binary mixtures of the desired alloying addition together with Al. Such alloys can either be concentrated (>50 wt%) or dilute in the respective addition and are used in many forms. Those commonly used include rods, powder, briquettes and tablets. By alloying in this manner, the dissolution rate in molten Al and the homogeneity in the final cast product are increased. After the melt is tailored to the required chemistry, it is either cast into large ingots or directly into a required shape.

1.6.2   Diffusion-Based Alloying/Powder Metallurgy

In accordance with the large number of metallic materials/alloys currently available, broad variations in material properties also exist. Consequently, for any given application, a particular material may behave satisfactorily from one perspective, yet poorly from another. The final material selection typically is one which meets the greatest number and most demanding of operating conditions when considering bulk material behaviour such as tensile/compressive stress, impact resistance or creep; only after these criteria are satisfied are the surface degrading effects of corrosion, oxidation, and wear considered.

To overcome the problems induced by surface-related phenomena, surface alloying/overlaying can often prove to be sufficient. In these coating-type procedures, an outer layer is deposited on the substrate material, the element(s) of which subsequently diffuse inward during the deposition process or a subsequent heat treatment. Some procedures allow for nearly complete diffusion of the deposit, which facilitates deposit adherence, and promotes favorable microstructural changes and chemical reactions between the deposit and substrate. Others, however, need only enough interfacial diffusion to ensure coating adherence, thereby maintaining an outermost composition equivalent to that of the deposited alloy/element. An example of the former is pack

cementation, whereas physical vapour deposition (PVD) is a method of obtaining the latter.

Pack cementation, despite being one of the earliest coating techniques developed, continues to be a frequently employed industrial practice [125-128]. In this batch process, parts to be coated are buried in a "pack" mixture, and subsequently sealed in a chamber to allow heating under a controlled atmosphere (typically Ar or Ar/H_2 mixture). The chamber is then held at temperature for a prescribed period of time, and cooled. Of chief importance to the process is the pack, which contains the coating element/alloy in powder form, a halide salt activator, and inert oxide filler such as Al_2O_3. Variations in pack composition depend on the substrate material being coated (typically plain carbon steels, stainless steels and Ni-based superalloys), and the desired composition and thickness of coating required.

The coating process itself has several essential stages [127,130]. Initially, a halide activator reacts with the metal powder forming volatile metal halides. Although various volatile species are possible, thermodynamic stability typically dictates that one dominates. In response to a negative activity gradient existing between the pack and substrate, gaseous diffusion of metal halides through the porous pack to the substrate results. Upon reaching the surface, the metal halides then decompose through one of several mechanisms, thus forming a metallic coating. With further isothermal heating, inward diffusion of the coating element(s) occurs, resulting in the formation of a surface alloy or compound.

Although a wide range of elemental coatings is possible using pack cementation, those more commonly encountered include Cr, Al, and B. As a means to enhance the corrosion and oxidation resistance behaviour of ferrous alloys, coating with Cr (chromizing) [129-131] or Al (aluminizing) [125] often prove to be viable solutions. Ni-based superalloys that are used extensively in the corrosive environment of gas turbine

engines also require additional protection; this is commonly achieved through aluminizing treatments [127,128, 132-134]. Aside from corrosion resistance, another surface related phenomenon that is addressed is wear. The service life of certain components can be greatly extended [126,127] by deposition of a surface layer of B (boronizing) [135].

Despite their satisfactory performance in many applications, elemental coatings are generally unsuitable in the more demanding operating environments. However, it has been demonstrated that the range of applications can be expanded through the co-deposition of several elements to yield an alloy coating. As previously mentioned, a critical step in pack cementation is the reaction(s) between the metal powder and halide salt activator which forms gaseous metal halides. Having developed a negative partial pressure gradient between the pack and substrate, vapour transport to the latter results. Therefore to simultaneously deposit two or more elements each must be of a similar partial pressure and in turn, pressure gradient. Thermodynamically, however, the free energies of formation for metal halides tend to differ greatly from element to element. Consequently, partial pressures do so as well; thus to achieve similar pressure gradients in practice is typically difficult. To overcome vapour pressure difficulties, possible solutions include the use of binary alloy powders in place of traditional, elemental ones, and multi-stage treatments. Examples of multi-element coatings currently produced by these alternative methods include Si/Ge [136], Al/Si [131], Al/Pd [133], Al/Yt [134], Cr/(Y,Zr) [137], and Cr/Al [138].

Aside from usage in the coating industry, diffusion-based alloying is also encountered in P/M [119]. To produce a given alloy, one practice is to blend appropriate portions of elemental powders, press and then sinter. As the part sinters at an elevated temperature, solid state diffusion occurs between adjacent particles. Although the aim is to produce a homogenous alloy product, this can be difficult to achieve in practice.

Consequently, the mechanical and physical properties are often inferior to those for components made from prealloyed powder.

1.7 TEM CHARACTERIZATION OF PRECIPITATES

Although numerous effects of microalloying are possible, each results as a distinct microstructural alteration of the unmodified base alloy. Whereas several changes are possible, alterations to the age hardening response are most frequently studied. The precipitates that form during aging occur on a microscopic scale and are relatively small (i.e. <100 nm). Their characterization requires knowledge of:

1) Habit planes (the crystallographic planes of the matrix metal that precipitates preferentially lie on),

2) Orientation with the surrounding matrix metal,

3) Morphology,

4) Size,

5) Chemistry,

6) Distribution (grains, grain boundaries), and

7) Crystallographic structure,

To complete such an analysis, researchers typically utilize electron microscopes of the scanning or transmission type. Whereas the former is of some use, it is the transmission electron microscope (TEM) that is by far the instrument of choice, due to its ability to examine the chemistry, crystal structure, and orientation relationships. Although both microscopes use a focussed beam of electrons to form the desired image, a scanning electron microscope (SEM) is limited to surface studies of relatively large areas. However, the TEM is used to actually look through a very small thin area. Looking through the sample, one can then generate images of internal structures such as precipitates.

Of great benefit to TEM users is the ability to view a sample in many different ways. The most common are bright field imaging and electron diffraction patterns. When using the former, the image observed is formed in the "image plane" by the portion of the incident beam which passes through the sample (transmitted beam). The contrast in such an image results from the incident beam being absorbed/diffracted to various degrees by features of different crystallography, chemistry or thickness. An example of a bright field image (BFI) is shown in Figure 1.21.

In contrast to BFIs, diffraction patterns (DPs), are exactly that - patterns (of spots) rather than an image. As some electrons pass through the sample to form a BFI, they are also diffracted, forming a pattern in what is referred to as the "back focal plane" of the microscope. Depending on the orientation of the sample relative to the incident beam, a unique, characteristic pattern is produced. The crystallographic direction that lies parallel to the incident beam is referred to as the "zone axis", and is used as the means to designate DPs. For the sake of simplicity and clarity, most studies rely on the use of low order zone axes, since the resulting DPs frequently exhibit a high degree of symmetry. For example, aluminum, having a face centered cubic structure, is typically studied using zone axes that are members of the <100>, <011>, and <111> families of directions (Figure 1.22). Each spot in the DP also represents the sum intensity of diffracted electrons from a particular plane. The vector running from such spots to the centre, brightest, spot (transmitted beam), represents a direction normal to this plane. Hence, one can superimpose crystallographic directions on a given BFI, provided the accompanying DP has been properly indexed.
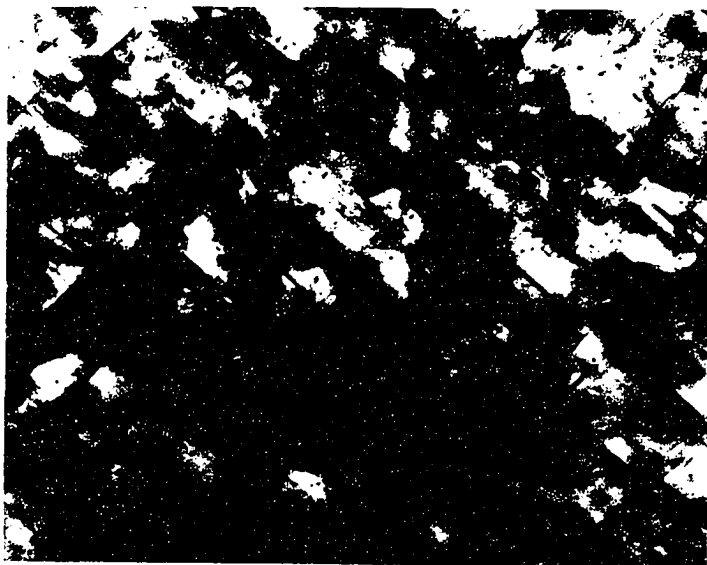
Figure 1.21 BFI of precipitates found in a sample of P/M aluminum alloy 2024 in an overaged condition [72].

(a)   (b)   (c)
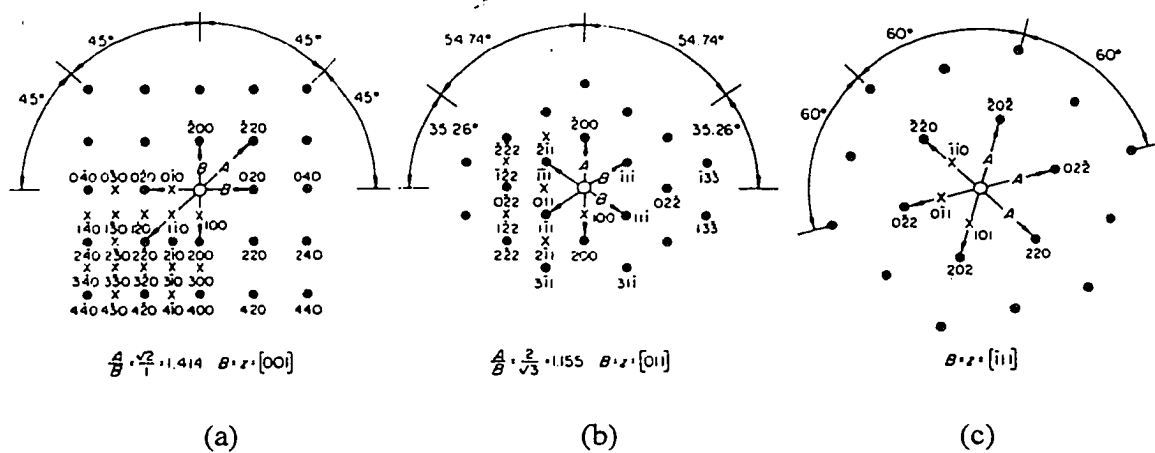
Figure 1.22 Sample DPs for an FCC crystalline material (i.e. aluminum). (a) <100>, (b) <110>, and (c) <111> [139].

Using BFIs and DPs in conjunction with appropriate sample tilting allows the user to orient a given grain to permit observation along a specific zone axis. Repeating this procedure for several different axes allows the various characterizing criteria for precipitates (other than precipitate chemistry) to be determined. Once the crystallographic structure of a desired precipitate and the surrounding matrix are known together with their respective orientation relationship, a common technique is to calculate theoretical diffraction patterns. Due to the time consuming nature of such an analysis, appropriate software packages are frequently employed. Calculated patterns for BCT θ' viewed in a <100> zone axis [140], orthorhombic S' as observed in a <100> zone axis [141] and orthorhombic Ω as observed in a <111> zone axis [142] are presented in Figure 1.23.
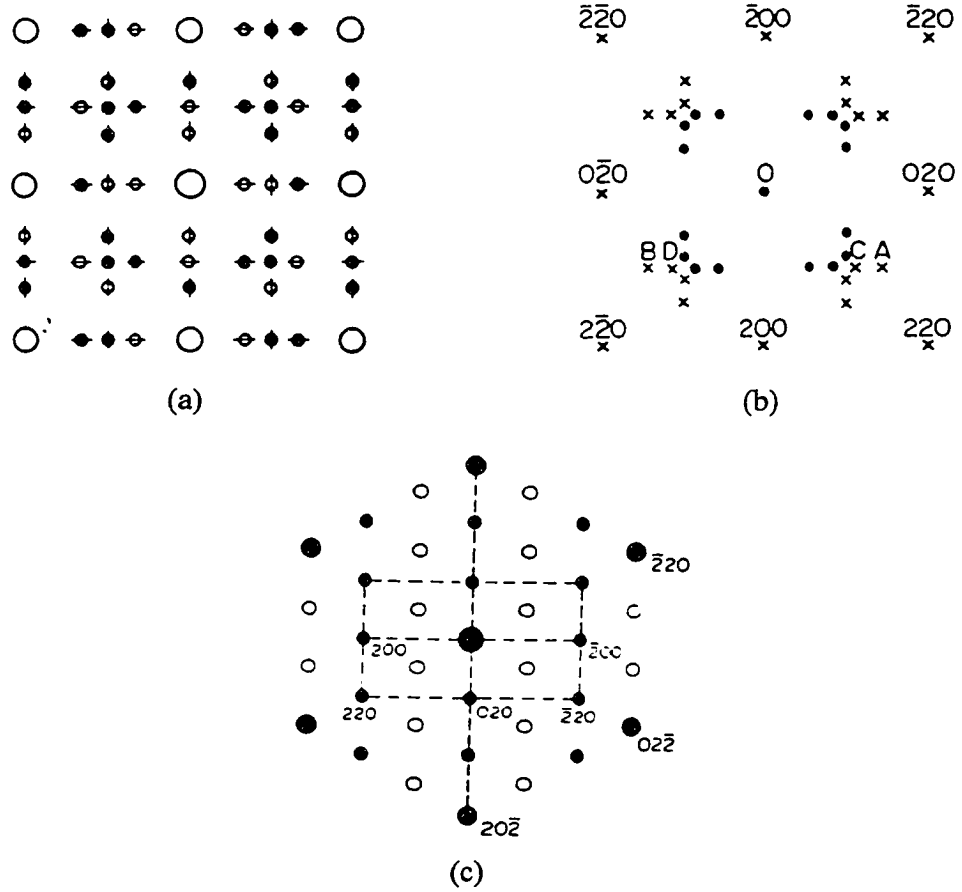
Figure 1.23 Calculated DPs for (a) θ' viewed in a <100> orientation [140], S' viewed in a <100> orientation [141] and (c) Ω viewed in along a <111> orientation [142]. Al (FCC) is the matrix in each instance.

1.8 RESEARCH OBJECTIVE

Microalloying, as applied to steels, has had a significant effect on the steel industry as a whole. By adding trace levels of elements such as V, Nb and Cb, a fine dispersion of extremely small carbides and/or carbonitrides may be formed, thereby enabling extremely high strengths to be realized. As such, an entirely new branch of high strength low alloy steels (HSLA) has been developed [4]. In light of these developments, many researchers have applied the same approach to aluminum-based alloys.

By experimenting with a broad variety of elements/combinations and heat treatments, several positive effects of microalloying have been discovered. Principal accomplishments include a modification of age hardening response, grain size, and secondary phase morphology. Despite the extensive data base that has thus far been developed, in almost every case, ingot metallurgy has been the means of microalloying. Hence, the possibility that the mode of alloying might influence net material properties has not been addressed. It is from this point that the objective of this research stems - the development of an alternative approach to traditional ingot metallurgy techniques for improving the mechanical properties of Al alloys through microalloying.

Conceptually, a powder metallurgy (P/M)-based process has been envisioned. Termed "core/shell" processing, the process consists of (a) the in-situ reduction of a microalloying element compound, followed by (b) the subsequent diffusion of the liberated element(s) into the desired substrate material. The entire process occurs while the material is isothermally held in a semi-solid condition. Thus, the process has the advantages of near net shape forming, higher tensile and yield strengths and enhanced machinability common to P/M produced components [95,100,101].

Many of the Al alloys presently used in industry contain multiple alloying additions. To further the performance of these alloys, microalloying is one possibility. However, determining the precise role of trace additions is often hidden or dampened

through the complicating effects of the many elements that are already present in the alloy. To avoid this difficulty, many researchers utilize simpler alloy systems that are representative of commercial counterparts. The results of these studies are then used as a guide to the potential effects that may arise in the more complex alloys. Following this approach, two Al alloys have been considered in this investigation - a complex commercial alloy (AA2014, Al-4.4Cu-0.8Si-0.8Mn-0.5Mg) and a simpler, yet representative a ternary alloy (Al-4Cu-0.5Mg). Specifically, the feasibility of adding trace (micro) additions of Li, Sn and Ag to these alloys was investigated. Thus, the overall intent was to establish a new procedure based on the attributes of P/M for microalloying Al alloys, and relate the findings to a traditional ingot metallurgy approach.

2 THEORETICAL CONSIDERATIONS

In the development of any materials processing technique, a theoretical understanding of the applicable underlying principles is required. With this in mind, several key points relevant to the process under development have been identified and are individually detailed in the following sections.

2.1 THERMODYNAMIC CONSIDERATIONS

The trace element of interest must first be dissociated from its source compound prior to diffusing into the alloy. Thus, any insight into the tendency for this reduction is invaluable, and as a means of assessment, one must consider the governing thermodynamic principles.

A thermodynamic software package, F*A*C*T*™ (Facility for the Analysis of Chemical Thermodynamics) [143] has been employed to provide the thermodynamic calculations. Using this package, the user is prompted to input the appropriate reactants in their respective amounts together with temperature and pressure. As output, the most plausible reaction products, together with a variety of thermodynamic data (including a calculation for the overall free energy change) are given. Based on these data, one can readily identify which of the candidates is/are most likely to be reduced into a form suitable for subsequent diffusion.

Using F*A*C*T*™, the dissociation of each compound in the presence of AA2014 was studied, assuming 100g of AA2014 together with 0.1 moles of the mineralogical, oxide or nitrate compounds for each system. The results are shown in Figure 2.1 and Table 2.1. As shown in Figure 2.1, thermodynamic predictions indicate
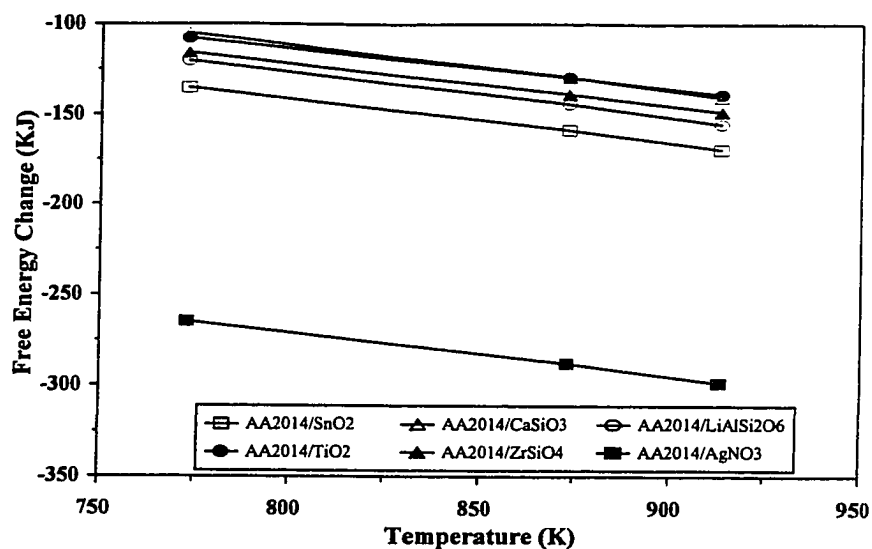
Figure 2.1 Calculated values of free energy change for the compound dissociation as a function of temperature using various alloy/compound mixtures.

Table 2.1 Summary of main reaction products predicted by F*A*C*T™ for selected AA2014/mineral, oxide or nitrate systems.

Trace Element Source	Predicted Reaction Products		
	Gaseous	Liquid	Solid
Rutile (TiO_2)	None	Al-Cu-Mn-Si	Al, $TiAl_3$, Al_2O_3, $MgAl_2O_4$, TiSi
Zircon Sand ($ZrSiO_4$)	None	Al-Cu-Mn-Si	Al, ZrSi, Al_2O_3, $MgAl_2O_4$
Spodumene ($LiAlSi_2O_6$)	None	Al-Cu-Si-Mn-Li	Al, Al_2O_3, $LiAlO_2$, Si, $MgAl_2O_4$, $Mn_{10}Si_{17}$
Wollastonite ($CaSiO_3$)	None	Al-Ca-Cu-Si-Mn	Al_2O_3, $MgAl_2O_4$, Si
Cassiterite (SnO_2)	None	Al-Sn-Cu-Mn-Si	Al, Al_2O_3, $MgAl_2O_4$
$AgNO_3$	None	Al-Ag-Cu-Mn-Si	Al, Al_2O_3, AlN, $MgAl_2O_4$

that all of the chosen minerals/compounds have a reasonable tendency for dissociation (i.e. negative free energy change); relatively speaking, $AgNO_3$ possesses the largest, cassiterite is intermediate, whereas wollastonite and rutile display the weakest.

Aside from predictions on the tendency to react, those pertaining to the anticipated reaction products (Table 2.1) are also of use. Intuitively, one may expect that should the liberated alloying element react to form a stable solid compound(s), its ability to diffuse into the central alloy core would be lessened. Conversely, if this element tends to concentrate within the liquid phase in a soluble manner, the formation of stable solid compounds is avoided, and an increased amount is available for diffusion. Using this information, it appears that once liberated, Ca, Sn, Li, and Ag should be readily available for diffusion into the central core.

2.2 DIFFUSION RATES

Once the element of interest has been liberated from its starting compound, the existence of a concentration gradient coupled with elevated temperature promotes diffusion-based alloying of the central alloy core. Hence, knowledge of diffusion rates in aluminum is required. Furthermore, since liquid phase sintering is employed, one must consider solid and liquid phase diffusion. A compilation of experimentally determined diffusion rates in solid aluminum has been established from literature and is shown in Table 2.2 [144]. Although no experimental data were found for the diffusion of Ca and Ti in Al, calculated values from the model developed by Burachynsky and Cahoon [145] are included. As shown in the Table, Ca appears to possess the fastest rate whereas that of Sn is second. Ag, Ti and Li are all about six times slower than Sn, and Zr is about five orders of magnitude slower again. As the anticipated diffusion rates differ by some six orders of magnitude, the rate of introduction of the required element into the solid constituent during sintering should vary considerably by element. It is well known that diffusion rates in molten metals are much higher than those in solids and typically

Table 2.2 Summary of diffusion coefficients in solid aluminum at temperatures of interest [144].

Element	D_{773K} (m^2/s)	D_{873K} (m^2/s)	D_{913K} (m^2/s)
Al[1]	4.06×10^{-14}	5.10×10^{-13}	1.20×10^{-12}
Ca[2]	2.63×10^{-11}	1.68×10^{-10}	3.14×10^{-10}
Sn[1]	8.13×10^{-13}	6.73×10^{-12}	1.38×10^{-11}
Ag[1]	1.56×10^{-13}	1.26×10^{-12}	2.56×10^{-12}
Li[1]	1.07×10^{-13}	1.01×10^{-12}	2.16×10^{-12}
Ti[2]	1.13×10^{-13}	$1.35 \times 10\text{-}12$	3.12×10^{-12}
Zr[1]	3.23×10^{-18}	2.41×10^{-16}	1.04×10^{-15}

1 Experimental   2 Calculated

range between 10^{-9} to 10^{-8} m^2/s, regardless of the element under consideration [146]. Thus, it is expected that the preferential diffusion path would be through the liquid component, with all elements having a similar likelihood of being alloyed into the central alloy core.

2.3   MASS BALANCE MODELING

To quantitatively model the results of microalloying, a computer program was developed which allowed input of all pertinent process variables. Modeled on the basis of a cylindrical component, values of core diameter, shell thickness, aluminum alloy, microalloying element, and element source compound/concentration were all required for the simulation. Each of these parameters is outlined in Figure 2.2. To accurately model this situation, data on the activity and activity coefficients of the desired microalloying elements in the base alloys of interest are thus required. However, due to a limited availability of such data, the program was written assuming ideal behaviour.

Consequently, the activity of any given element is assumed to be equal to its respective mole fraction, thus defining equilibrium as the point of equal concentrations rather then chemical potentials. Ideally most of the alloying addition should diffuse into the core after reduction; however, some must remain in the shell to satisfy equilibrium conditions. To model this situation, plots of core and shell concentration versus the fraction of alloying addition diffused into the core were produced for Ca, Ag, and Sn (Figure 2.3) using measured dimensions and starting concentrations corresponding to actual samples. The intersection point of the two lines represents the equilibrium concentration expected together with the efficiency of alloying element usage.

Rc   = Core Radius
Rnet = Overall Product Radius
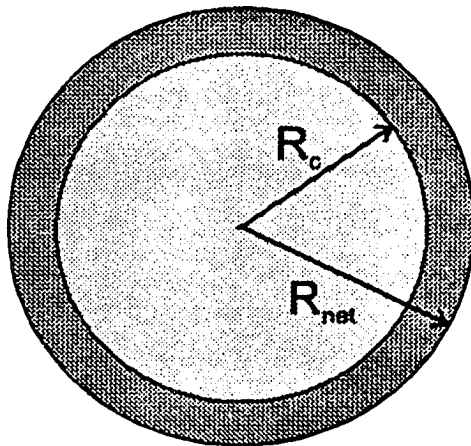
Core Variables:
1) Alloy
2) Size
3) Shape

Shell Variables:
1) Thickness (Rnet-Rc)
2) Mineral/Oxide Addition
3) Mineral/Oxide Concentration
4) Location

Sintering Variables:
1) Temperature
2) Time

Figure 2.2 Schematic illustrating the process variables input into the computer model.
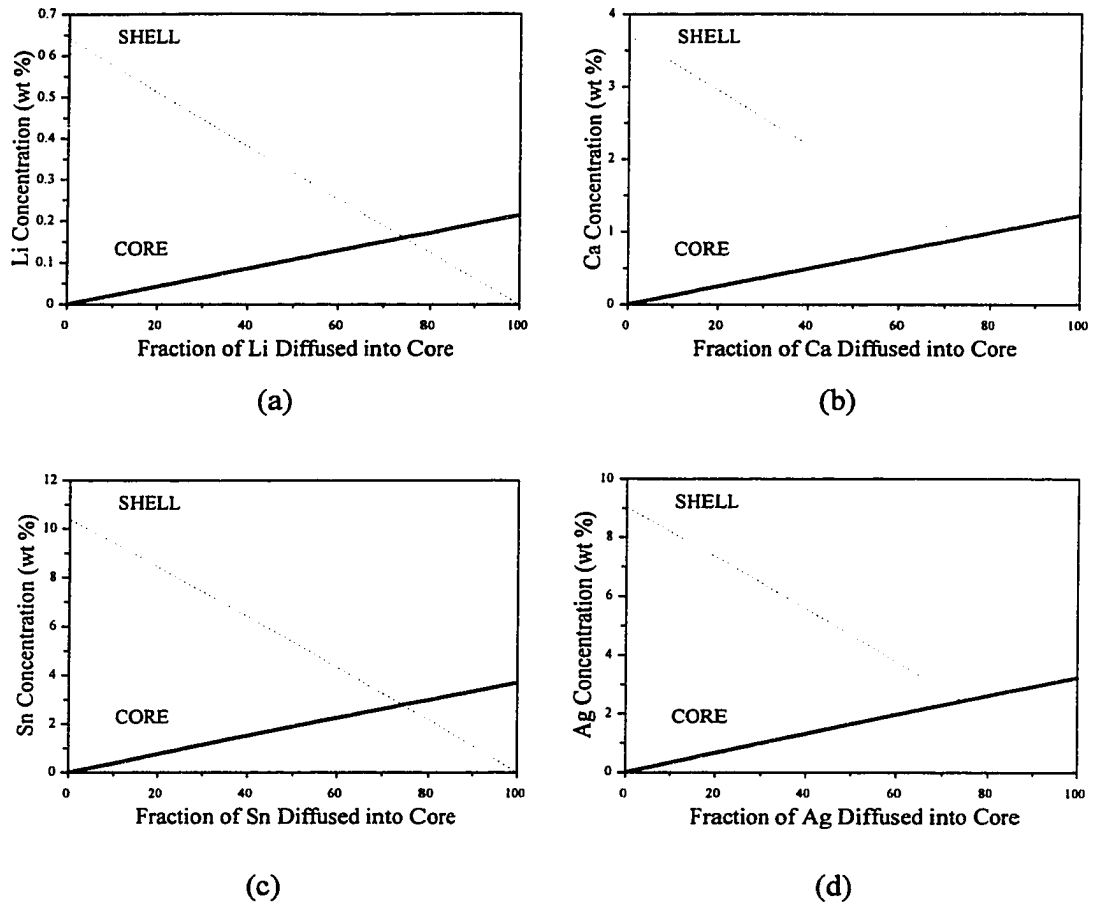
Figure 2.3   Calculated concentrations of microalloying addition in core and shell components as a function of the fraction of element diffused. (a) Li, (b) Ca, (c) Sn, and (d) Ag. In all cases a 25mm diameter core and a 2mm thick shell were assumed.

3 EXPERIMENTAL PROCEDURES

The following sections detail the experimental procedures and techniques employed in the work.

3.1 MATERIALS

As a basis for all experiments, two Al-based alloys were considered, one an Al-4Cu-0.5Mg wt%) ternary alloy, and the other a commercial alloy - 2014 (Al-4.4Cu-0.8Si-0.8Mn-0.5Mg wt%). To accommodate the processing technique developed, powder forms of each alloy were produced by Valimet, located in Stockton, CA, using inert gas atomization and sieved to -200 mesh. The resulting powder particles were encased in a thin (approximately 50nm thick) shell of Al_2O_3. Because of the exceptionally high affinity that Al has for O_2, the formation of such a layer is unavoidable regardless of gas purity or the atomization process utilized. However, because of the residual stress generated from pressing and the formation of a liquid phase during SLPS, this layer is fractured. This facilitates densification and eventually leads to a fully dense product.

For comparison in wear and corrosion experiments, a wrought version of 2014 was obtained. This material was subjected to chemical (atomic adsorption) and tensile property analyses; all results were found to lie within the acceptable limits cited for AA2014 [19].

As sources of trace elements, three compounds were used. Spodumene was used as a mineralogical source of Li, and synthetic SnO_2 and $AgNO_3$ were used when adding Sn or Ag. The spodumene ($LiAlSi_2O_6$) used was originally in a lump form that was subsequently ground in-house to a fine powder using a ceramic shatter-box and several drops of a 50/50 v/o mixture of acetic acid and methanol [147]. Naturally occurring

cassiterite (SnO$_2$) was originally selected as a source of Sn. However, the mineral proved difficult to obtain after closure of the only North American operation in Nova Scotia, Canada. Hence, reagent grade SnO$_2$ was purchased from Fisher Scientific, having a purity of 99.9% (metals basis) and a particle size of -200 mesh. Silver nitrate (AgNO$_3$) was likewise purchased from Fisher Scientific, it too having a purity of 99.9 %.

Due to the reactive nature of Al, an inert atmosphere was required for all sintering and heat treatment practices. In each instance, ultra high purity Ar gas (99.99%) supplied by Canadian Liquid Air was utilized.

3.2 SAMPLE FABRICATION

To produce standard and microalloyed samples, certain techniques fundamental to P/M processing were employed; blending, cold isostatic pressing (CIPing), sintering, machining and swaging. Flowcharts of processing routes are given in Appendix A. In the production of P/M alloy standards, the process began by loading the selected powder into a cylindrical rubber mold, 25mm in diameter and 25 cm in length. Once capped with a rubber top, the fixture was then sealed with electrical tape and placed in the CIP (Loomis™). The pressure within the CIP was then raised to 190 MPa using a solution of water and mineral oil (20:1), held for 30s and then slowly reduced back down to atmospheric conditions. The once loose powder was thus formed into a single coherent cylinder, having a diameter of 20mm. The integrity of these "green bodies" was then enhanced through SLPS.

In the pressing of "core/shell" samples, the sequence noted in the previous paragraph was used twice; first to produce the "core" component and second to encase this core in the thin "shell" constituent. Whereas alloy powder alone was used to form the "core" component, the "shell" was formed from a mixture of the same alloy powder milled together with a mineral/compound source of the desired microalloying addition.

Such mixtures were milled in a ceramic ball mill for 24h under a rotational speed of 60 RPM in air. To deter agglomeration, 10-15 drops of an acetic acid/methanol (50/50) solution was added immediately prior to milling [147]. A summary of all mixtures produced is shown in Table 3.1. After pressing alloy powder to form the "core" component, the space that remained between it and the rubber mold was then filled with

Table 3.1 Summary of the milled mixtures utilized.

Base Alloy	Mineral/Compound Added	Quantity of Addition (Moles/100g of Alloy)
Al-4Cu-0.5Mg Ternary	$AgNO_3$	0.1
Commercial 2014	$LiAlSi_2O_6$	0.04
Commercial 2014	SnO_2	0.08
Commercial 2014	$AgNO_3$	0.1

the milled mineral/alloy mixture. Once sealed, this system was then re-pressed under the same conditions initially used, leaving a composite body composed of a central alloy core surrounded by a thin (1-2mm thick) shell of the milled mixture. Termed "core/shell" processing, the technique is a powder metallurgy approach that incorporates reaction sintering and diffusion in response to an activity gradient.

The density and mechanical integrity of all isostatically pressed products were subsequently enhanced by liquid phase sintering. Each green body was set in an alumina crucible and then loaded into a quartz sintering tube. After flushing with Ar (UHP) and evacuating (mechanical vacuum pump) three times, the quartz tube was then evacuated for 1h. Prior to sintering, each green body was de-gassed under mechanical vacuum at 673K for 0.5h. Once the degassing time had elapsed, the evacuated tube was then back filled with Ar and left to flow under a slightly positive pressure. Sintering was then carried out at either 873K or 903K for the commercial (2014) and ternary (Al-4Cu-

0.5Mg) alloys, respectively. Sintering within the semi-solid regime, a small portion of liquid enriched in alloying elements (principally Cu) was then formed within the specimen. Samples were held at temperature for times ranging between 0.5 and 16h and then cooled to room temperature at a rate of approximately 3K/min. In "core/shell" products, the shell layer was then chipped free of the microalloyed "core", and like alloy standards, was then lightly machined to a uniform diameter.

To reduce residual porosity, sintered bodies were processed by one of two means - hot or cold swaging. In the hot process, the sintered body was first pre-heated to a temperature of ~693K and isothermally held at this temperature for 1h. Using consecutively smaller dies, the diameter of a given sample was reduced over a span of 12-14 passes with intermittent re-heating for 3-5 minutes. Sections were reduced to a final diameter of 8.6mm (5:1 reduction ratio) and subsequently used in the measurement of age hardening response and tensile properties. In cold swaging practices, sintered bodies were alternately annealed for 2h at 693K and swaged at room temperature to ~15% reduction in area (RA). This cycle was repeated until a total RA of 50% was achieved (2:1 reduction ratio). Samples processed in this manner were then used in the evaluation of wear and corrosion resistance.

3.3 SINTERED BODY CHARACTERIZATION

Once a sintered product was produced, each was examined by several means in an effort to determine the success or failure of microalloying prior to further processing. The methodology for each is discussed in the following sections.

3.3.1 Mercury Densitometry

Since the microalloying technique developed was based on P/M principles, the presence of porosity is to be expected. Furthermore, since such internal voids can

influence many material properties, the extent of porosity must be quantified. To accomplish this, the specific gravity was measured and compared to that of an equivalent, wrought product of the same material. One technique commonly employed to perform this measurement is mercury densitometry.

In this procedure the sample of unknown specific gravity is first weighed in air, and then again when fully immersed in mercury. Whereas the first measurement represents the mass of the sample, the second represents a measure of the amount of Hg displaced by the respective volume of the sample. Knowing the density of Hg at the temperature of the measurement allows the second value to be converted into an equivalent sample volume. Finally, the specific gravity is calculated, by dividing sample mass by volume.

3.3.2   X-Ray Diffraction (XRD)

In many instances throughout this research, the identification of the chemistry and crystalline structure of a material was of great importance. Although such an analysis can be completed by many means, X-ray diffraction (XRD) analysis was that principally used in this research. All specimens were examined under Cu Kα radiation using a Rigaku™ XRD unit with operating parameters of 40KV, 40mA, and scan speed of 4 deg/min.

Each material to be analyzed was prepared in a finely dissociated form (powder, filings) and mixed with acetone to form a thick slurry. Subsequently, the slurry was applied to the frosted depression in a glass microscope slide, allowed to dry, and finally placed in the instrument for analysis. Using the accompanying spectrum analysis software (Jade 3.0), a list of the most plausible elements or compounds present was produced. Simulated patterns of these phases were then overlaid on each data spectrum for comparison.

3.3.3 Scanning Electron Microscopy (SEM)

To conduct in-depth examinations of sintered microstructures a JEOL JSM 840 scanning electron microscope (SEM) operating at 25 kV and a probe current of 0.3 nA was used. Chemical analyses were conducted with the accompanying energy dispersion spectrum (EDS) unit employing a NORVAR™ window and standardless correction. Prior to examination, each section was mounted in bakelite, consecutively ground on 240, 320, 400, and 600 grit SiC abrasive papers, and then polished with 1 and 0.05 μm Al_2O_3 powders on canvas and billiard cloths respectively. Final polishing was carried out using a colloidal suspension of SiO_2 applied to Buhler "Microcloth". After thorough rinsing in water, samples were dried with ethanol and examined in the SEM.

To gain an understanding of the extent of microalloying, several means of analysis were considered. In an effort to determine the net amount of microalloying element introduced, numerous, low magnification EDS analyses were conducted and the results averaged to obtain an approximation of the bulk alloy chemistry. On a microscopic scale, the chemistry of certain individual features of interest (grains, intergranular regions) was also quantified, but using spot analysis (dwell time of 120s). The general distribution of elements within the microstructure was determined by X-ray mapping.

3.4 HEAT TREATMENT

To harden age hardenable aluminum alloys they are first subjected to a solutionizing treatment, during which time most alloying additions dissolve into solid solution. Following this, the alloy is then quenched and subsequently re-heated (aged) at a lower temperature (typically <473K), thus promoting a change in hardness with time. Initially, hardness rapidly increases up to a maximum, followed a relatively slow, consistent decrease. Since both the base alloys and microalloyed materials produced in this work also harden in this manner, their age hardening response must be determined.

From such data, heat treatment parameters that lead to peak hardness (and in turn tensile strength) can be established and applied to all samples prior to mechanical testing.

To determine hardness data and respective age hardening curves, the procedure detailed in the following paragraphs was developed and followed. Several short (~1cm) lengths were cut from rods previously hot swaged at 678 K. During swaging samples were subjected to an 80 % reduction in area (RA), equivalent to a reduction ratio of approximately 5:1. Using a Southbend™ lathe, the ends of each cylinder were then machined such that they were parallel. To avoid excessive oxidation during heat treatment, all samples were encapsulated in glass tubing under ultra-high purity Ar gas. When encapsulating, 2 or 3 samples were loaded into a glass tube sealed at one end. At a distance of some 10 cm from the samples, the tube diameter was reduced to approximately 1mm using an acetylene torch. The entire tube was then evacuated using a mechanical vacuum pump, followed by Ar flushing. After repeating the evacuate/flush cycle 4 to 6 times, ternary Al-Cu-Mg and 2014-based samples were then sealed off and solutionized in a horizontal tube furnace using temperatures of 793±2 K and 775±2 K, respectively. Finally, after an elapsed time of 4200s, samples were water quenched and dried with ethanol. Each was then individually re-encapsulated and aged in a box furnace at temperatures of either 393K, 433K or 473K (±2.5K in all cases) for times ranging between 300 and 3.6×10^5s.

3.5 HARDNESS TESTING

Although the hardness of a given alloy can be measured by many means, it is the service environment that typically dictates which method is chosen. For example, in a laboratory type setting hardness data is usually gathered using an accurate, yet time consuming, Vickers hardness machine whereas in an industrial situation hardness is measured using a Rockwell hardness tester because of its efficiency and simplicity. Since the ternary alloy under consideration is primarily used within a laboratory environment,

hardness measurements were conducted using the former means. However, because 2014 is used in industrial applications, data were collected using the Rockwell tester. This facilitated comparison of the data found in this work to that published elsewhere.

A Leco hardness tester was used to measure Vickers hardness. Prior to hardness measurement, the surface of each sample was first ground with 600 grit SiC abrasive paper, followed by consecutive polishing with 1 μm Al_2O_3 powder on a canvas and 0.05 μm Al_2O_3 on billiard cloth. In each hardness measurement, a diamond pyramid indentor was forced into the surface using an applied load of 1 kg. The diagonals of each square indentation were then measured, averaged, and the corresponding hardness determined from tabulated conversion charts. To produce a single data point, the overall process was repeated 5 or 6 times and the results averaged.

When measuring Rockwell hardness, a digital hardness tester was used. Operating in the "B" scale (HRB), a steel ball with a diameter of 1/16" was pressed into the surface of a sample with an applied load of 100 kg. Prior to testing, the surface of each specimen was ground using 600 grit SiC abrasive paper. Each data point was based on an average of 5 or 6 measurements in the same manner as Vickers hardness testing.

3.6 TEM SAMPLE PREPARATION

When analyzing samples in a TEM, the most critical, and often difficult, procedure is sample preparation. With this in mind, two means of preparation were considered - electropolishing and ion milling. For both methods, samples were first heat treated to the T6 condition and a disc approximately 1mm thick disc was removed using a Buhler low speed diamond saw. Subsequent grinding on consecutively finer abrasive papers of 320, 400 and 600 grit SiC was continued until disc thickness was reduced to approximately 100 μm. Using a mechanical punch, discs 3mm in diameter were then removed from the thinned disc and subjected to one of the two following procedures.

In the case of electropolishing, the 100μm thick discs were subjected to twin jet electropolishing using a Struers™ Tenupol-3 polisher. Process variables included the polishing solution, flow rate, voltage, current, temperature and photosensitivity. Several polishing solutions were considered (Table 3.2). For each solution, the temperature and flow rate were held constant while various combinations of other processing parameters were considered. Once electropolishing was complete, samples were thoroughly rinsed in a bath of distilled water, followed by 3 consecutive baths of ethanol. Once rinsed, each sample was dried and then briefly examined in the TEM to determine whether the sample was thinned enough to permit analysis. Frequently, the most suitable samples were produced using the acetic acid-based solution and settings for applied flow rate and photosensitivity of 5 and 7 respectively.

Table 3.2 Electropolishing solutions considered for the preparation of thin foils.

Polishing Solution	Temperature (K)	Voltage (V)
33 v/o HNO$_3$ + 67 v/o Methanol	248	12
20 v/o HNO$_3$ + 80 v/o Methanol	253	15
40 v/o Acetic Acid + 30 v/o Orthophosphoric Acid + 20 v/o HNO$_3$ + 10 v/o H$_2$O	298	12

Ion milling was also considered as an alternative to electropolishing. Small discs approximately 100 μm in thickness were further ground on 600 grit SiC paper down to a final thickness of about 50 μm. Dimples were then ground into each face of a specimen using a Model 656 Gatan dimple grinder. Rough dimpling was conducted to a depth of 15 μm on each face using 6 μm diamond paste followed by final polishing with 1 μm Al$_2$O$_3$. Once cleaned and dried with ethanol, samples were then ion milled using a Gatan ion milling machine operating at 6kV and 100 mA. Coarse milling was first conducted

for 1h with the sample inclined at an angle of 15° to the ion beam, followed by 1h at 12°. Fine milling was then performed at 10° until a hole was detected in the sample. During each milling stage the specimen holder was cooled using liquid nitrogen. Prior to examination samples were dried with ethanol to remove any condensation that may have formed on the sample as it was heated to room temperature.

3.7 TENSILE TESTING

To determine the influence of microalloying additions on overall alloy strength, tensile tests in accordance with ASTM standard E8M-93 [148] were conducted. A schematic diagram of a test specimen is shown in Figure 3.1. Samples were machined from hot swaged rods heat treated into a T6 condition and tested using an Instron™ test frame under a constant strain rate of 0.01 s^{-1}. The resulting data were then analyzed using accompanying software to determine engineering values of yield strength (YS), ultimate tensile strength (UTS) and elongation. To assess the general mechanism of failure, fracture surfaces were examined using a JEOL JSM 840 SEM operating under an applied voltage of 25kV.
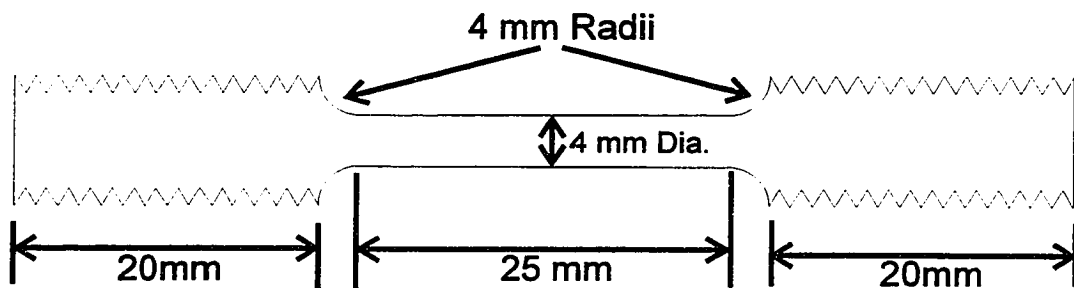
Figure 3.1 Schematic illustration of a tensile test specimen.

3.8   WEAR TESTING

Wear tests were conducted following ASTM standard G77-93 [149] (block on ring) using a ring of M2 tool steel heat treated to a hardness of 63-65 HRC. All tests were conducted on samples in the T6 condition polished with 600 grit SiC abrasive paper. Prior to testing, each sample was ultrasonically cleaned in acetone, dried, and weighed using a digital balance to the nearest 0.1 mg. Test parameters included a sliding speed of 0.5 m/s, sliding distance of 1000 m, and applied loads of 10, 20, 40, and 98 N. After testing, samples were ultrasonically cleaned in methanol, rinsed with acetone, dried, and re-weighed. Wear scars were examined using the JEOL JSM 840 SEM. Chemistry and morphology of wear debris were also determined using the SEM. Debris from samples worn under the largest applied load was analyzed by X-ray diffraction (XRD) using a Rigaku diffractometer and Cu-Kα radiation.

3.9   CORROSION TESTING

In the measurement of corrosion rates, potentiodynamic polarization curves were established using a EG&G Parc Model 350A corrosion measurement console. Disc-shaped samples (16mm dia., 3mm thick) were cut from cold swaged rods (50 % R.A.) and heat treated to the T6 condition. Immediately prior to testing, samples were lightly ground on emery paper, followed by water cleansing. Measurements were then conducted at room temperature in a solution of 0.6M NaCl (3.5 wt %) buffered to a pH of 6.0.

4 RESULTS

4.1 MATERIALS

Prior to conducting actual processing experiments, a chemical analysis of each alloy powder was completed using wet chemical analysis. The actual and reported composition for each alloy is given in Table 4.1. As shown, the composition is in close agreement with that specified in each case.

Table 4.1 Comparison between the reported and measured chemical compositions of P/M alloys used in this research.

Alloy	Al	Cu	Si	Mn	Mg
Commercial 2014	Bal.	4.4	0.8	0.8	0.5
Measured P/M 2014	Bal.	4.19	1.39	0.48	0.44
Reported Ternary	Bal.	4.0	0.02	---	0.48
Measured Ternary	Bal.	4.04	0.037	---	0.52

Since the processing technique developed is one based on P/M principles, both the size and shape of alloy powders must also be considered. Micrographs of each powder are shown in Figure 4.1; the spherical morphology resulting from atomization is evident. Particle size analyses for both powders are presented in Figure 4.2 as measured in a water-based slurry using a Malvern™ particle size analyzer. An average particle size (50% finer) of approximately 20 µm was noted for both alloys.

(a)   (b)
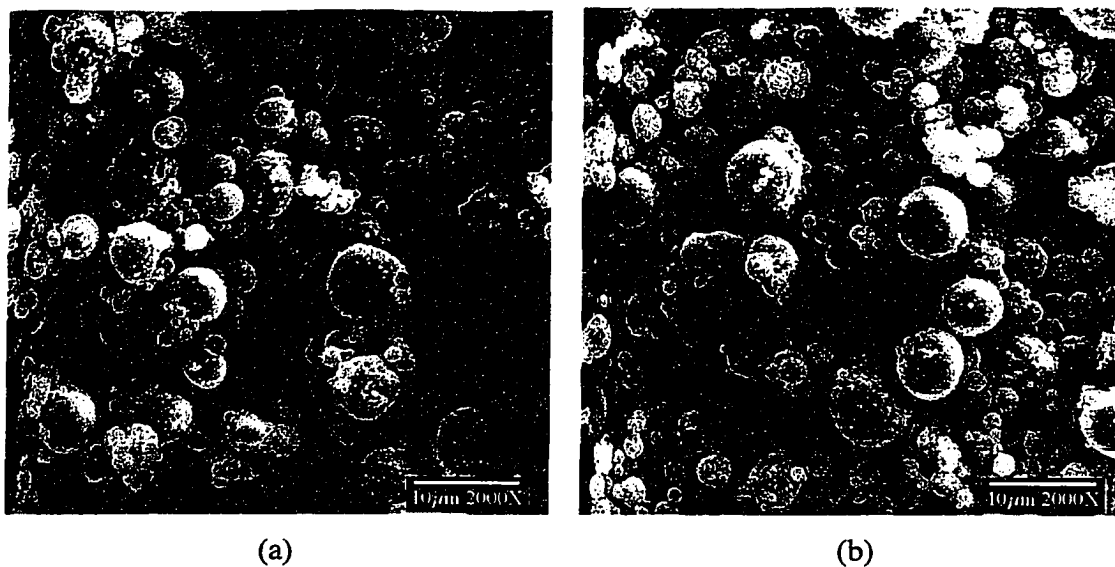
Figure 4.1 Morphology of alloy powders produced through inert gas atomization.
(a) ternary Al-Cu-Mg alloy and (b) alloy 2014.
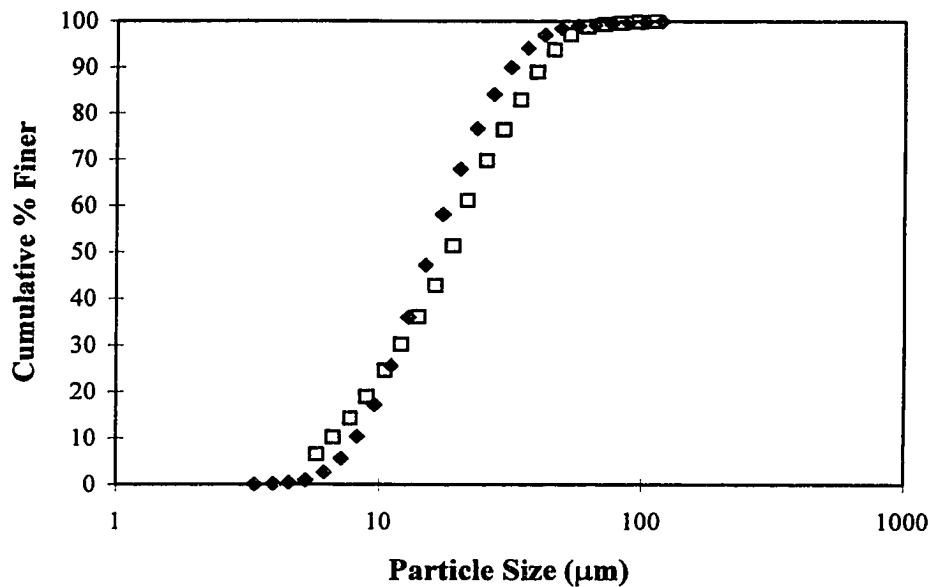
Figure 4.2 Particle size analysis of (a) ternary Al-Cu-Mg alloy (□) and (b) alloy 2014 (♦)
powders.

To verify the identity of those compounds used as sources of microalloying additions (SnO_2, $AgNO_3$, and $LiAlSi_2O_6$), each was analyzed using XRD after ball milling with alloy 2014 powder. The resulting spectra from these unsintered mixtures are shown in Figures 4.3 to 4.5. The location and intensity of the peaks present in each spectrum are measured with the accompanying software package and compared to an extensive database of known substances. An output of the most likely phases present is then generated and a simulated pattern for each substance identified is superimposed beneath the raw data. In each instance, the anticipated compounds were confirmed to exist and thus it was assumed that milling practices had minimal impact on chemistry/phases.
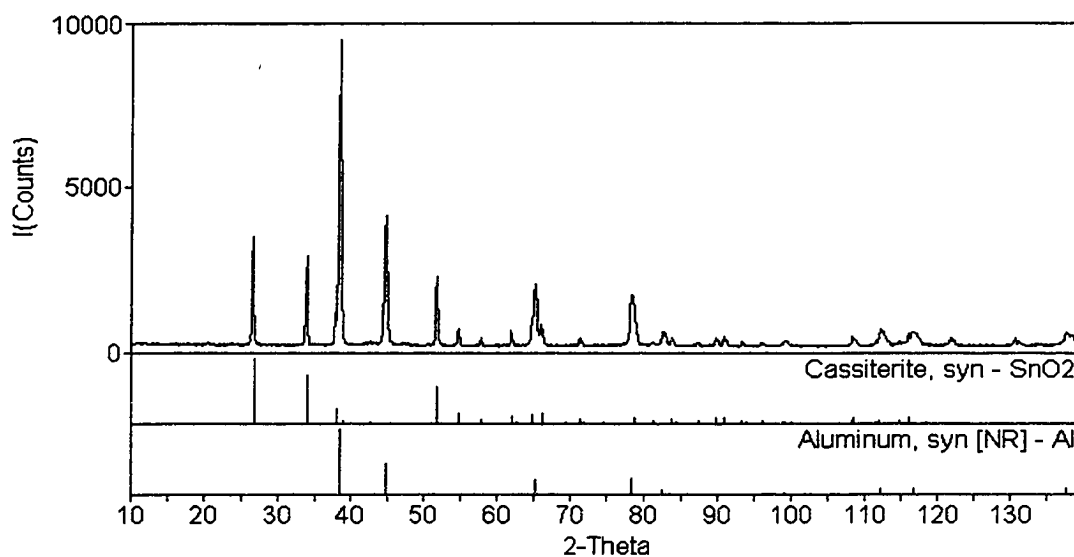
Figure 4.3 XRD spectrum for ball milled mixture of P/M alloy 2014/ SnO_2.
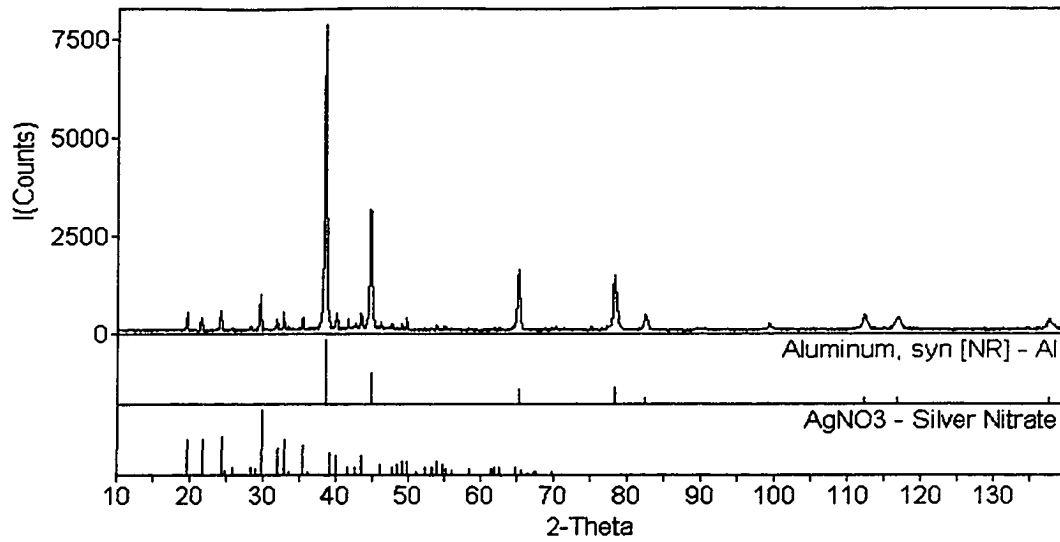
Figure 4.4 XRD spectrum for ball milled mixture of P/M alloy 2014/ AgNO3.
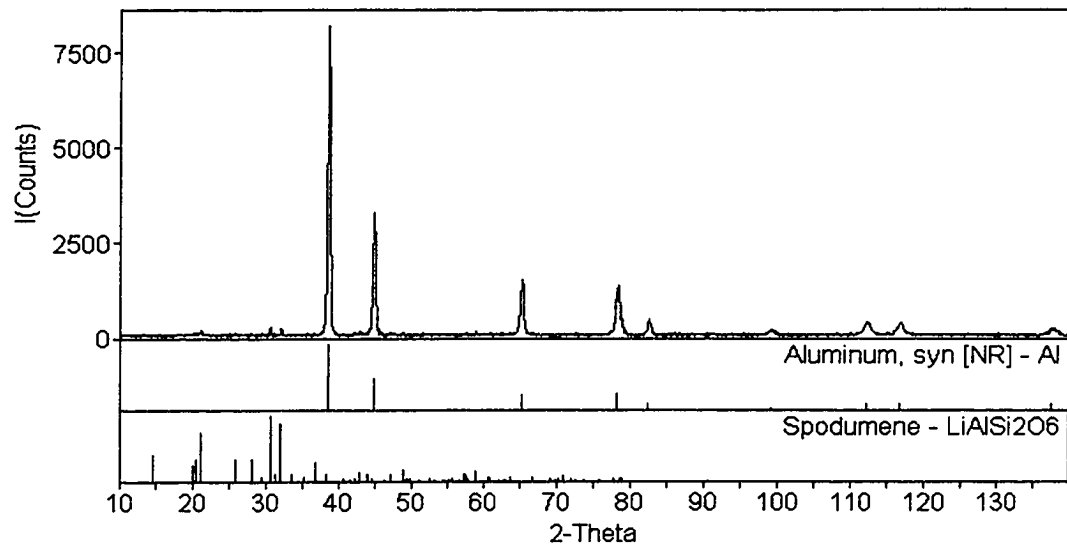
Figure 4.5 XRD spectrum for ball milled mixture of P/M alloy 2014/ LiAlSi2O3.

4.2 DENSITY MEASUREMENTS

Density measurements performed on all relevant P/M samples in green, sintered, hot swaged and cold swaged conditions are presented in the following sections. In each case, measured densities are compared to the theoretical density of wrought 2014 (2.8 g/cc) [19]. Values cited in Tables 4.2 to 4.4 are the average of two ore more measurements. A complete listing of all data is given in Appendix A.

4.2.1 Ternary and 2014 Alloy Standards

Results of density measurements for the two alloy systems of interest are given in Table 4.2. Although each system differed in chemistry and sintering temperature, both densified appreciably during sintering. After swaging, final densities for hot swaged products were typically 97 to 99% of theoretical. These values decreased slightly for cold swaged products due to a lower RA.

Table 4.2 Measured densities of ternary alloy and 2014 standard samples. The percentage of theoretical density is given in brackets.

Alloy System	Green (g/cc)	Sintering Time (h)	As-Sintered (g/cc)	Hot Swaged[1] (g/cc)	Cold Swaged[2] (g/cc)
Ternary	2.25	2	2.31 (83%)	2.71 (97%)	----
		4	2.55 (91%)	2.71 (97%)	----
2014	2.32	0.5	2.65 (94%)	2.77 (99%)	2.68 (96%)
		2	2.68 (96%)	2.77 (99%)	2.74 (98%)
		16	2.59 (93%)	2.75 (98%)	2.73 (98%)

1 Total RA of ~ 80%   2 Total RA of ~ 50%

4.2.2 Microalloyed Samples

Density measurements of core/shell processed samples microalloyed with Ag and Sn are presented in Tables 4.3 and 4.4 respectively. All core components experienced considerable densification when sintered, reaching densities ~90% of theoretical. In attempts to reach full density, hot and cold swaging practices were considered. When swaged at room temperature, final densities were typically ~96-98% of theoretical, whereas final densities for hot swaged samples were ~98-99% of theoretical. Despite the success of these post-sintering operations, cracking was encountered during the hot swaging of certain samples microalloyed with Sn. Although this difficulty was only observed in a few instances for those samples sintered 8h or less, after a 16h sinter the problem became very acute and resulted in a shattering of the specimen. Consequently, densification to near full density could not be achieved by this means. When examined in an SEM, fracture surfaces clearly revealed an intergranular mode of failure (Figure 4.6).

Table 4.3 Measured densities of ternary alloy and 2014 samples microalloyed with Ag. The percentages of theoretical density are given in brackets.

Alloy System	Green (g/cc)	Sintering Time (h)	As-Sintered (g/cc)	Hot Swaged[1] (g/cc)	Cold Swaged[2] (g/cc)
Ternary/Ag	2.25	2	2.56 (91%)	2.75 (98%)	----
		4	2.60 (93%)	2.76 (99%)	----
2014/Ag	2.32	2	2.59 (93%)	2.75 (98%)	2.73 (97%)
		4	2.56 (91%)	2.77 (99%)	2.76 (99%)
		16	2.63 (94%)	2.72 (97%)	2.71 (97%)

1 Total RA of ~ 80%   2 Total RA of ~ 60%

Table 4.4 Measured densities of alloy 2014 samples microalloyed with Sn or Li. The percentages of theoretical density are given in brackets.

Alloy System	Green (g/cc)	Sintering Time (h)	As-Sintered (g/cc)	Hot Swaged[1] (g/cc)	Cold Swaged[2] (g/cc)
2014/Sn	2.32	0.5	2.60 (93%)	2.77 (99%)	2.73 (98%)
		1	2.57 (92%)	2.75 (98%)	2.71 (97%)
		2	2.77 (99%)	2.65 (95%)	2.77 (99%)
		4	2.58 (92%)	2.78 (99%)	2.71 (97%)
		16	2.55 (91%)	Too Friable	2.70 (96%)
2014/Li	2.32	16	2.63 (94%)	2.76 (98%)	----

1 Total RA of ~ 80%   2 Total RA of ~ 60%
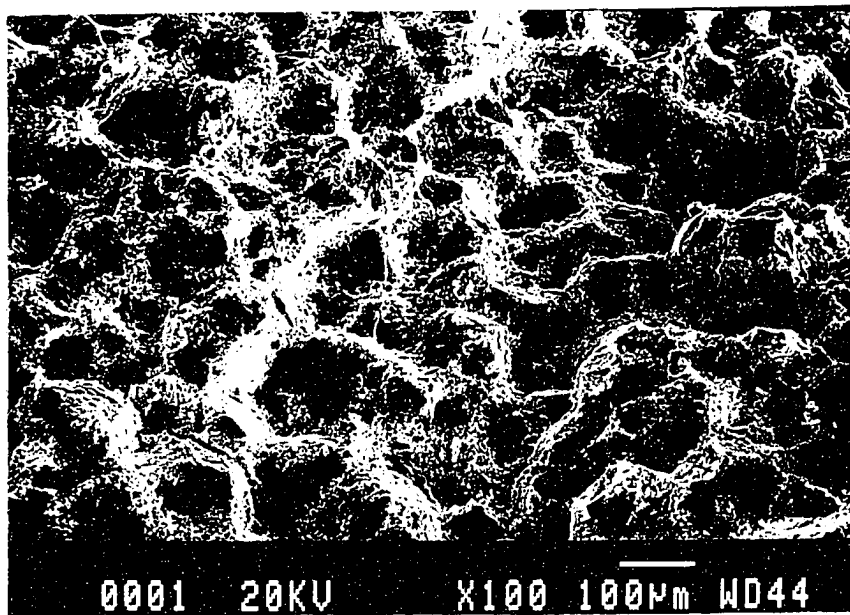
Figure 4.6 Fracture surface produced in a Sn modified sample (16h sinter) when hot swaged.

4.3   MICROALLOYED SAMPLE CHARACTERIZATION

4.3.1   XRD

During core/shell processing, it is vital that the selected microalloying element source compound be reduced. Although thermodynamics indicated that this was indeed possible, such analysis is, however, theoretical and fails to address the kinetics of a reaction. Thus, a more direct means is required to assess the extent of mineral/compound reduction during sintering. The method chosen for such an analysis was XRD.

4.3.1.1   Lithium Microalloying

In an attempt to microalloy alloy 2014 with Li (mineral source spodumene), sintering times of up to 16h were examined. In all spectra, it was demonstrated that spodumene underwent little, if any, reduction even after the 16h sinter (Figure 4.7). The dominant phases present were determined to be Al, $CuAl_2$, and spodumene, with an apparent absence of other Li-based compounds such as $LiAlO_2$.
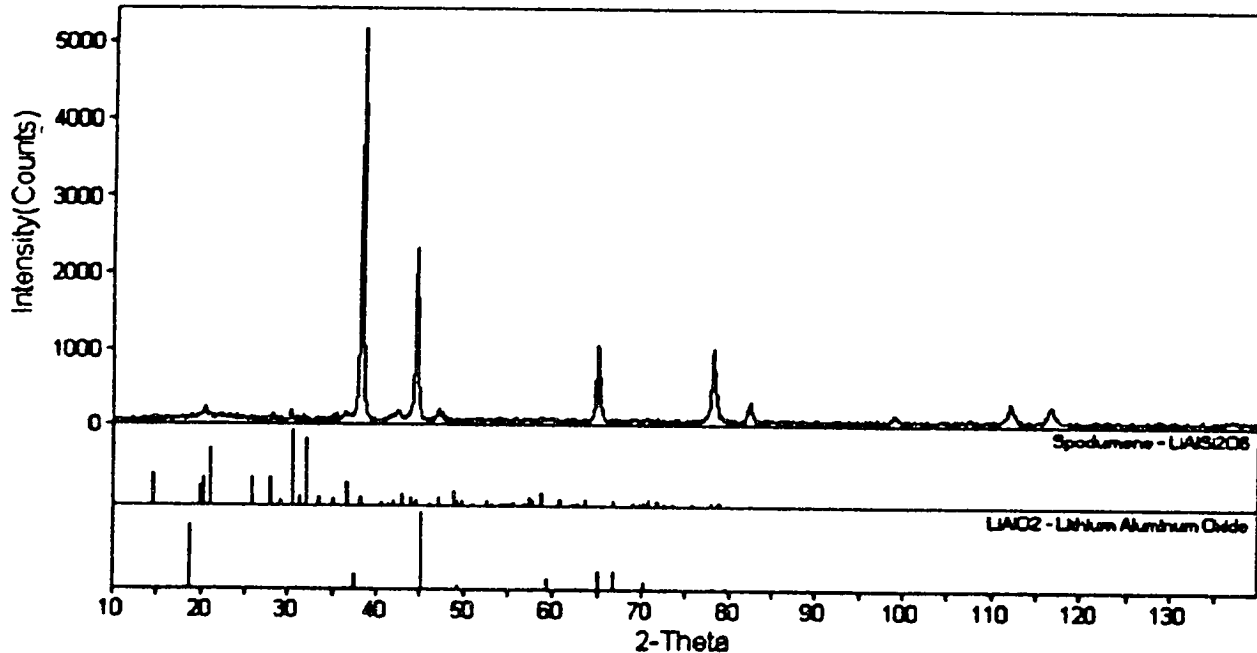
Figure 4.7 XRD spectra for a mixture of 2014/ 5v/o spodumene sintered for 16h at 873K.

4.3.1.2 Tin Microalloying

To introduce Sn as a microalloying addition (source, SnO_2), sintering times ranging between 0.5 to 16h were considered. After each trial, filings were taken from sections of the shell and subjected to XRD analysis. Spectra were then arranged in a 3-D format with the longest sintering time (16h) positioned in the foreground and that of the unsintered mixture farthest in the background (Figure 4.8). As is evident by the emergence of peaks associated with metallic Sn, there is an immediate dissociation of SnO_2 even after a sintering time as short as 0.5h. However, this reaction slows appreciably and the reduction remains incomplete even after 16h.
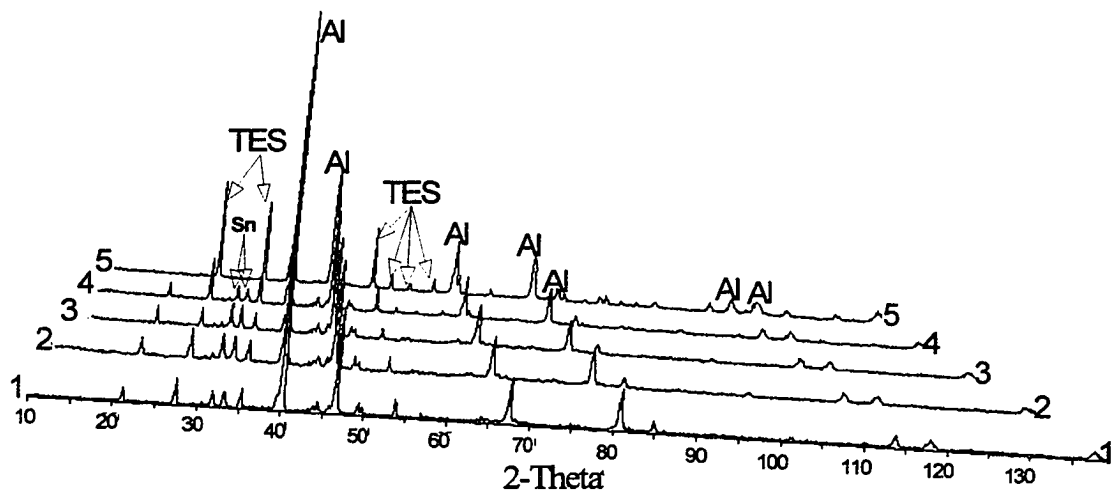
Figure 4.8 XRD scans conducted on AA2014/SnO_2 mixtures sintered for increasing lengths of time (scans 1-5 denote sintering times of 4, 2, 1, 0.5, and 0h respectively). Nomenclature - "Al" indicates aluminum peak, "Sn" tin peak, and "TES" trace element source, in this case - SnO_2.

4.3.1.3 Silver Microalloying

Using the same approach as outlined in the previous paragraph, the extent of $AgNO_3$ dissociation was also considered. An examination of shell components after sintering for 4 and 16h (Figure 4.9) showed that the nitrate was completely reduced after sintering for these times. Unfortunately, the presence of metallic Ag could not be distinguished from the surrounding Al-based matrix as each has a nearly identical characteristic spectrum.
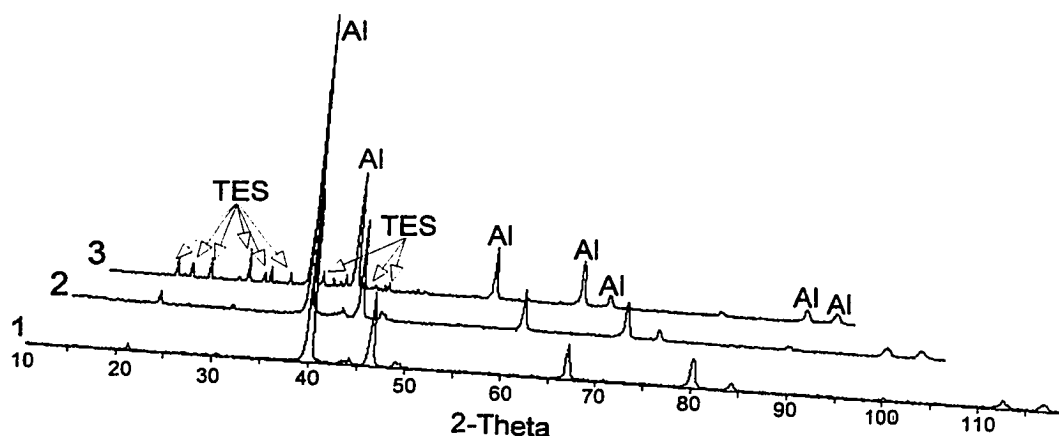
Figure 4.9 XRD scans for $AA2014/AgNO_3$ mixtures sintered for 16h (scan 1), 4h (scan 2), and unsintered mixture (scan 3). Nomenclature - "Al" indicates aluminum peak, "TES" trace element source in this case - $AgNO_3$.

4.3.2   SEM/EDS

Previously, XRD of sintered shell components determined that a considerable reduction of the microalloying element source compounds of Sn and Li occurred during sintering. Using core sections that were associated with the shells subjected to XRD, the extent of diffusion-based microalloying was measured through SEM/EDS analysis. Unfortunately, analysis of light elements such as Li was impossible using the SEM

available; thus, only those samples potentially microalloyed with heavier elements (Ag, Sn) were considered.

A net quantification of bulk core chemistry as a function of sintering time was obtained through macroscopic scans. Averaged concentration measurements of randomly selected areas are shown in Figure 4.10. Although some measurements approached the lower limit of detection for the instrument, these results were reproducible and deemed reasonable since more accurate, wet chemical analyses of several of the same samples indicated similar elemental concentrations.
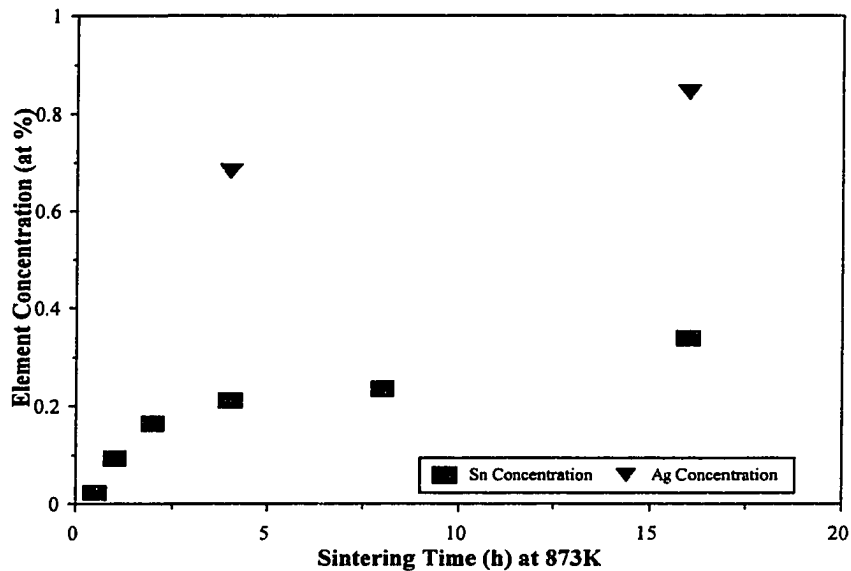
Figure 4.10 Approximate concentrations (at %) of Sn and Ag in modified and unmodified alloy AA2014 samples determined by wet chemical analyses and large scale energy dispersive EPMA scans.

Similar tests were also conducted on unmodified 2014 samples which had been previously analyzed using wet chemical means and found not to contain an appreciable (<0.05 wt%) amount of Sn or Ag. SEM/EDS results likewise determined a Sn concentration to be <0.05 wt%; however, that measured for Ag was typically about 0.4 wt%.

Although the presence of alloying elements may be verified on a macro scale, the respective microstructural location typically dictates the net influence on bulk material properties. In general, the microstructure of standard P/M 2014 is comprised alloy grains and an intergranular component. Alloy grains had a composition similar to that of the bulk alloy, whereas the intergranular regions were enriched in alloying elements in accordance with solubility limits as predicted from binary phase diagrams. The intergranular segregation of Cu was the most extensive, with typical concentrations of 30 wt%. All other alloying elements were also segregated to the intergranular regions, but were typically concentrated at levels of 1 to 3wt%.

To determine the location of diffused species, samples of 2014 microalloyed with Ag and Sn were examined using X-ray mapping and more in-depth spot analysis techniques. Regarding the Ag modified sample, X-ray mapping results (Figure 4.11) suggested a homogenous distribution of Ag between alloy grains and intergranular regions. Spot analyses of the same area verified the presence of Ag in both regions, but indicated that a modestly higher concentration of Ag existed within alloy grains (Table 4.5). For the Sn modified sample, mapping results showed that Sn was concentrated in the intergranular regions only, although the distribution of Cu was similar to that found in Ag modified samples (Figure 4.12). Spot analyses at higher magnifications confirmed these results as no Sn was detected in alloy grains, yet concentrations ranging from 6 to 8 wt% were measured in intergranular regions (Table 4.6).

(a)

(b)

(c)
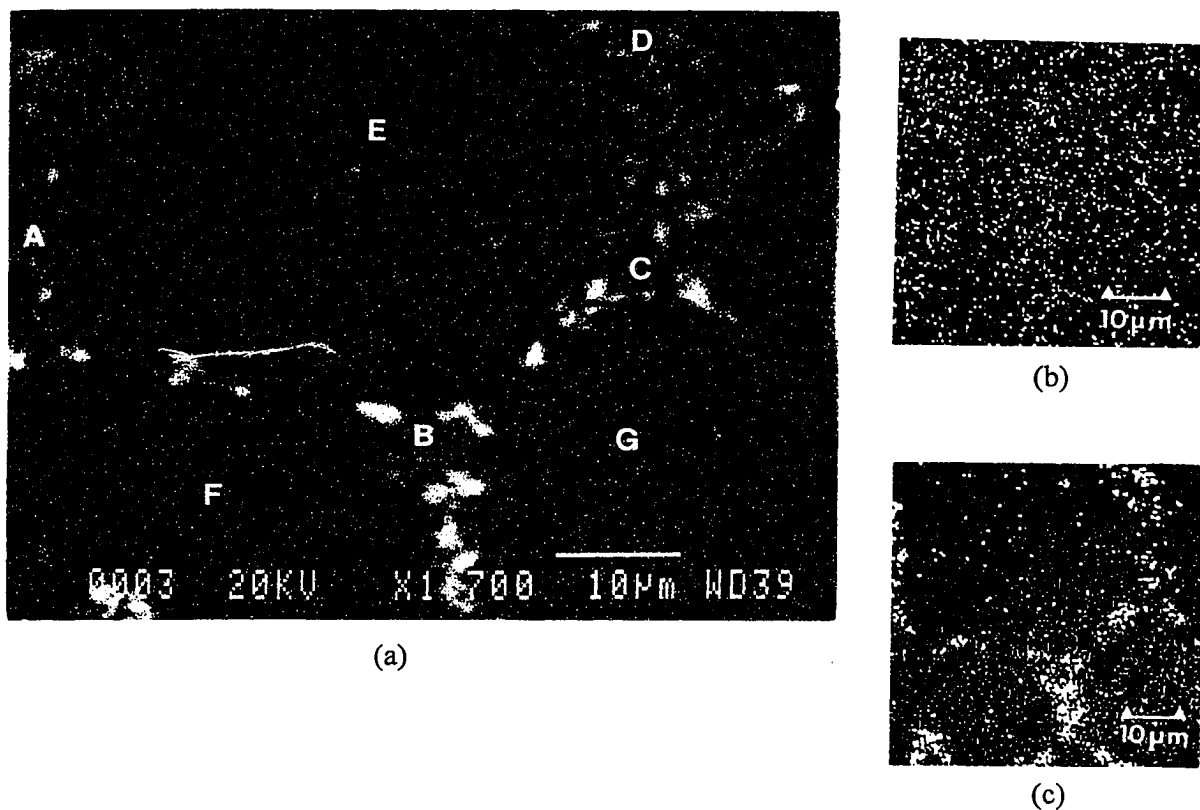
Figure 4.11 Ag modified 2014 (16h sinter) analysed through X-ray mapping and point analyses. (a) SEI image, (b) Ag scan, and (c) Cu scan.

Table 4.5 Results of EDS analyses (wt %) for regions labeled in Figure 4.11.

					Regions			
	Bulk	A	B	C	D	E	F	G
Al	Bal.	Bal.	Bal.	Bal.	Bal.	Bal.	Bal.	Bal.
Cu	4.93	18.04	13.92	10.08	8.17	3.40	3.04	2.52
Si	0.39	1.60	1.65	0.98	0.81	0.00	0.00	0.00
Mn	1.23	2.41	3.17	2.95	3.31	0.49	0.29	0.43
Mg	0.68	3.87	2.43	2.34	2.28	0.46	0.33	0.51
Ag	2.67	1.15	1.35	2.18	1.94	2.69	2.82	3.20

(a)

(b)

(c)
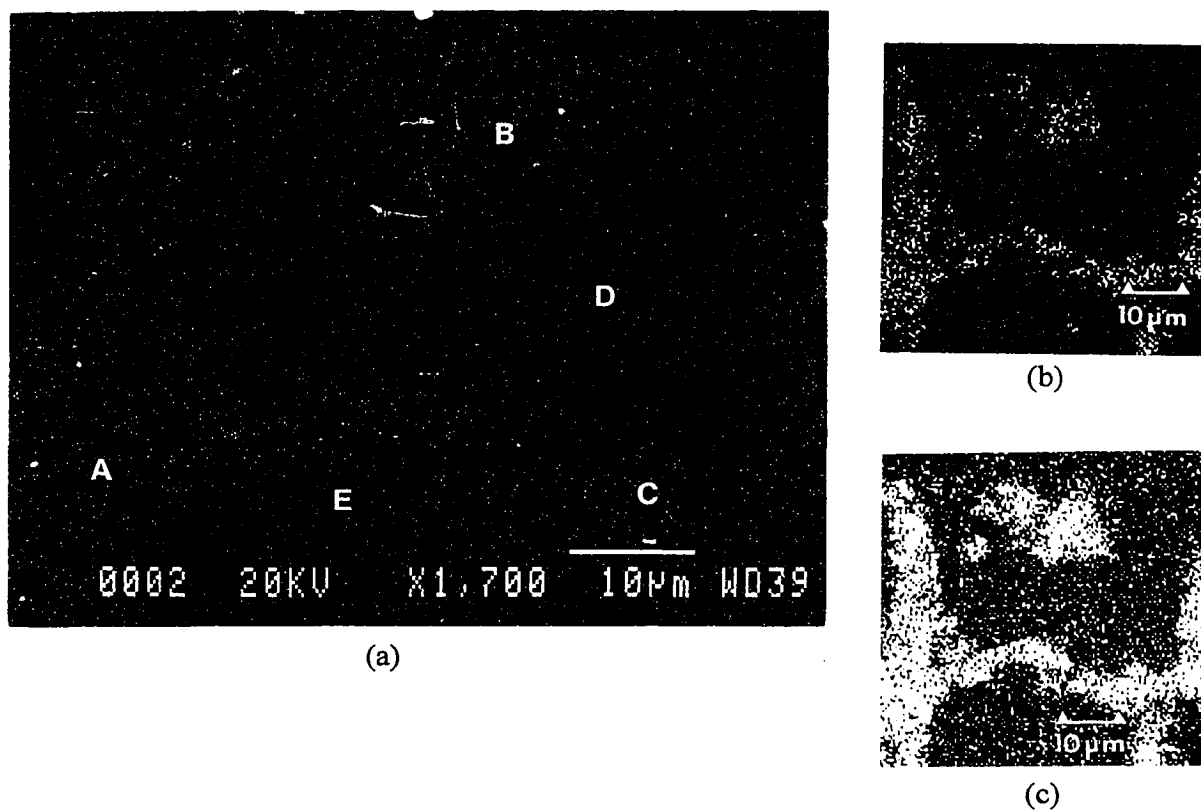
Figure 4.12 Sn modified 2014 (16h sinter) analysed through X-ray mapping and point analyses. (a) SEI image, (b) Sn scan, and (c) Cu scan.

Table 4.6 Results of EDS analyses (wt %) for regions labeled in Figure 4.12.

	Bulk	A	B	Regions C	D	E
Al	Bal.	Bal.	Bal.	Bal.	Bal.	Bal.
Cu	13.17	41.28	30.02	35.85	3.38	4.41
Si	1.62	0.26	0.43	0.82	0.00	0.00
Mn	0.94	0.92	1.37	1.34	0.11	0.31
Mg	1.44	3.64	3.54	3.36	0.33	0.50
Sn	4.41	8.39	8.35	5.95	0.00	0.00

4.4 AGE HARDENING RESPONSE

Due to their inherent chemistry, each of the alloys considered was age hardenable. To study this behaviour, samples were solutionized at an appropriate temperature, water quenched and then aged. The hardening response of numerous samples was determined as a function of aging time and temperature as detailed in the following sections. The values cited in Figures 4.13 to 4.21 represent the average values calculated from several measurements. A complete listing of all hardness data is given in Appendix B.

4.4.1 Ternary Alloy Standards

As a starting point, aging behaviour for the ternary alloy standards was determined. The aging response at 433K of samples sintered for 2 and 4h is shown in Figure 4.13. From the figure, it is apparent that each responds in a similar manner, with peak hardness reached after aging for approximately 18h. Apparently, the 2h increase in sintering time has minimal influence.

4.4.2 Ag Microalloyed Ternary

Using the same sintering times as applied to ternary alloy standards, Ag microalloyed samples were also produced. The aging response of each is shown in Figure 4.13. These samples aged to a peak hardness level of some 30 points higher than their standard counterparts, although the time to peak hardness (18h) seemed consistent. Furthermore, it again appears that the sintering time has a minor impact on the peak hardness reached; this implies that an amount of Ag, sufficient to enhance hardness, is introduced during both sintering times considered.
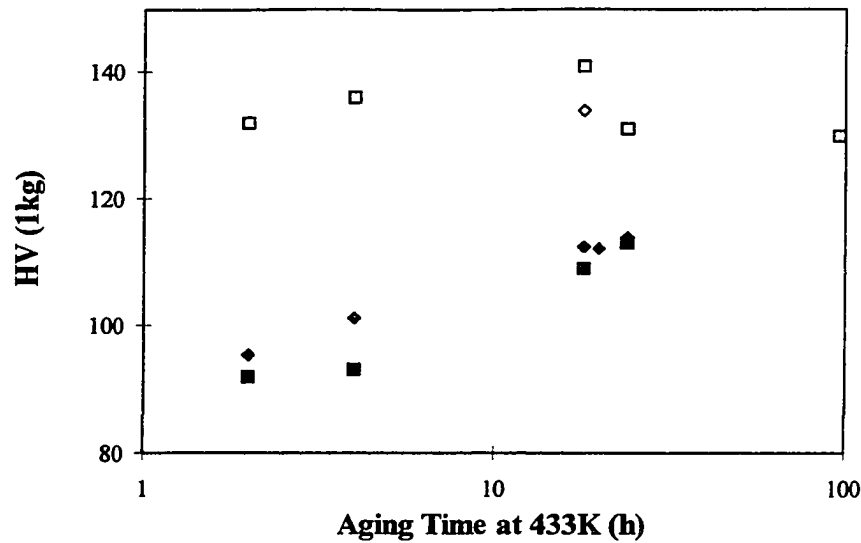
Figure 4.13 Age hardening response for ternary alloy-based samples. Ternary alloy standards sintered 2 and 4 h denoted by (◆, ■) respectively. Ag microalloyed samples sintered for 2 and 4h denoted by (◇, □) respectively.

4.4.3   2014 Alloy Standards

Using a heat treatment practice similar to that applied to commercial wrought 2014 (solutionize at 502°C for 70 min, water quench, and age [18]), aging curves were generated for a variety samples. Those considered included P/M alloy 2014 standards as well as specimens potentially microalloyed with Ag, Sn, Li, or Ca. Although the principal variable of interest was sintering time, aging temperature was also considered in select cases.

Age hardening curves for P/M alloy standards sintered for times ranging from 0.5 to 16h are shown in Figure 4.14. As can be seen in the figure, an increase in the sintering time promotes a general decrease in the age hardening response; this leads to lower peak hardness. This decrease is relatively minor between samples sintered for shorter periods of time (0.5 and 2h), but becomes significant when considering times as long as 16h.
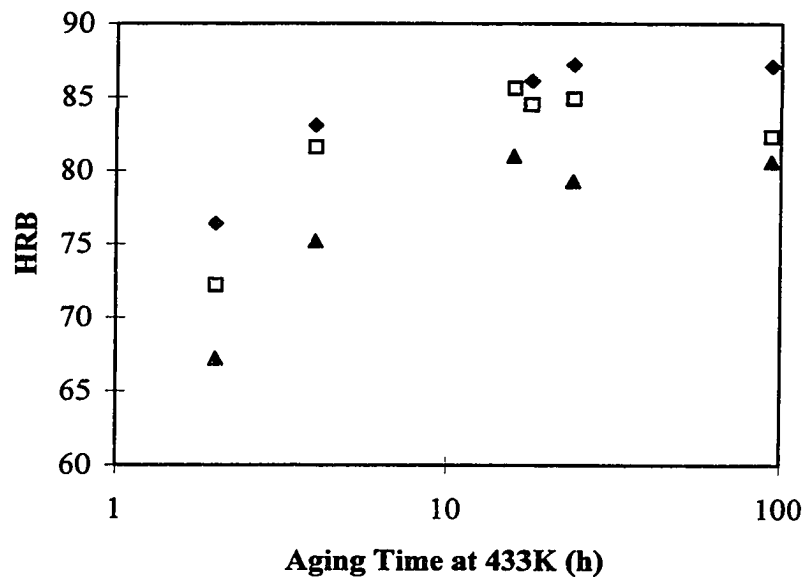
Figure 4.14 Age hardening response at 433K of alloy standards sintered for times of 0.5h (◆), 2h (□), and 16h (▲).

4.4.4 Ag Modified 2014

For Ag modified samples, sintering times of 2, 4 and 16h were considered; their aging responses are presented in Figure 4.15. As shown, the peak aged hardness reached for samples sintered for 2 and 4h are very similar to those measured for the equivalent alloy standards. Further similarities, both in overall curve shape and reduced peak hardness with increased sintering time were again noted.
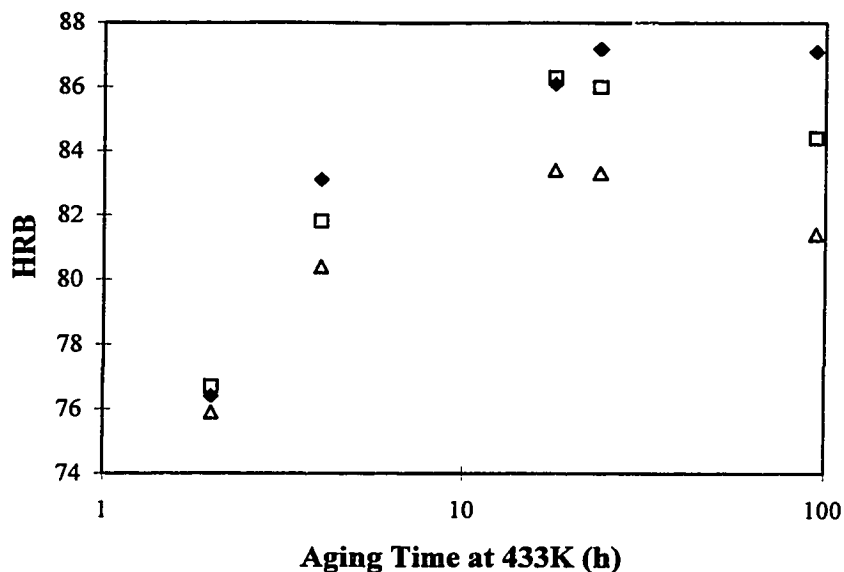
Figure 4.15 Aging response at 433K of Ag modified samples of 2014 sintered for times of 4h (□) and 16h (△). For comparison, the response of a 2014 standard sintered for 0.5h (♦) is also included.

However, when the sintering time was increased to 16h, a distinct difference was apparent whereby Ag modified samples were consistently harder than an equivalent alloy standard (Figure 4.16). Hence Ag has dampened the detrimental effect of increased sintering time on hardness. Such an effect was not apparent in samples sintered for shorter periods of time, despite the introduction of a similar quantity of Ag.
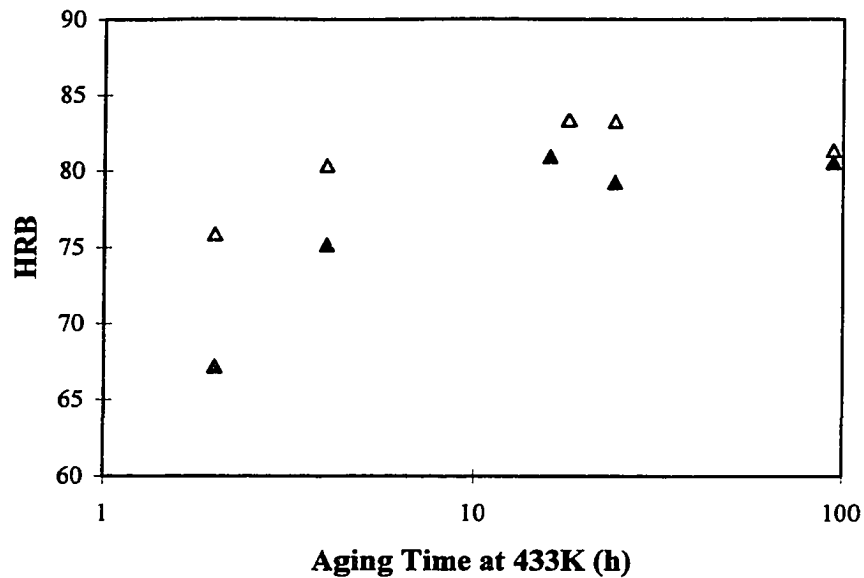
Figure 4.16 Comparison of aging response for an alloy 2014 standard (▲) and a Ag modified sample of 2014 (△) previously sintered for 16h.

4.4.5 Sn Modified 2014

For the case of Sn modified P/M samples, the consistent trend of decreased hardness response with sintering time was again noted. However, unlike samples containing Ag, the peak aged hardness values were typically below those of similar alloy standards (Figure 4.17). This became more pronounced as sintering time increased and Sn modified samples sintered for only 8h were actually softer than alloy standards aged twice as long (16h) (Figure 4.18). At no time was a dramatic increase in hardness observed as was the case with Sn additions to an Al-4 wt. Cu alloy [6,7].
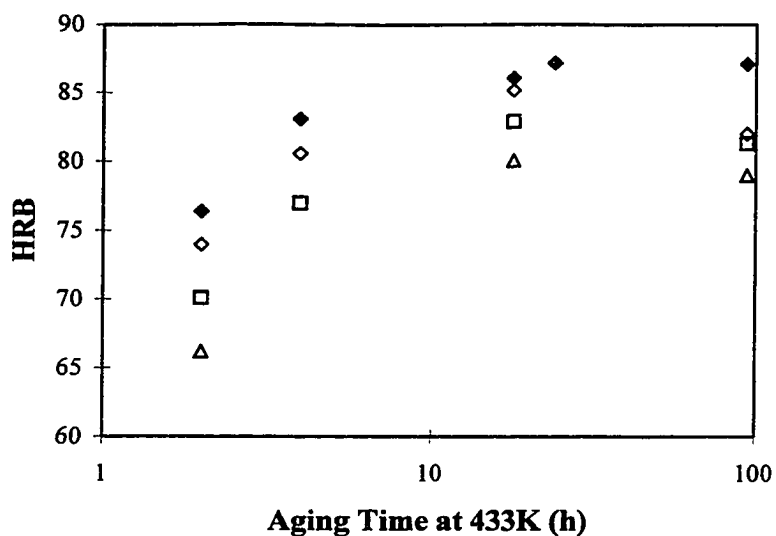
Figure 4.17 Aging response at 433K for Sn modified 2014 samples sintered for 1h (◇), 2h (□), and 4h (△). For comparison, data for an unmodified 2014 standard sintered 0.5h (◆) is also included.
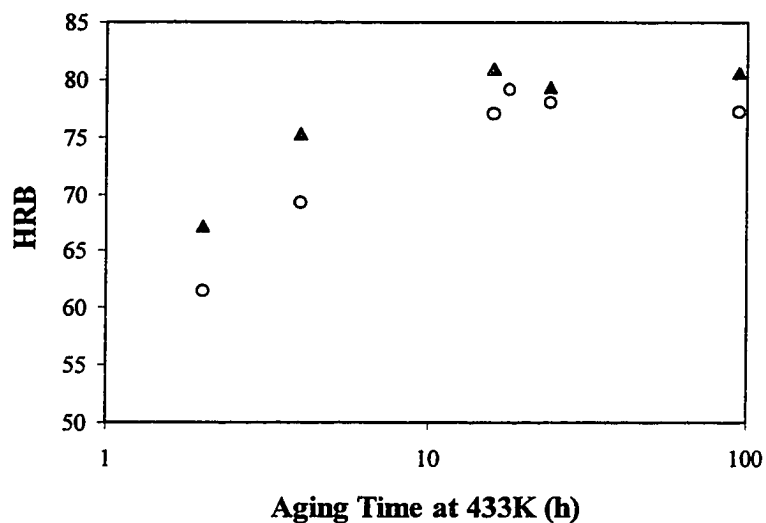
Figure 4.18 Aging response at 433K for Sn modified 2014 sintered for 8h (○) and unmodified 2014 standard sintered 16h (▲).

4.4.6   Li Modified 2014

Thus far, there has been considerable evidence presented to suggest that Li microalloying was unsuccessful. However, due to the difficulties of detecting Li, the age hardening response was nonetheless characterized. Using a sintering time of 16h, the age hardening response of standard alloy samples as well as those potentially microalloyed with Li were assessed and compared for aging temperatures of 393, 433, and 473 K (Figures 4.19 to 4.21). As is indicated, little difference in age hardening response occurred at each aging temperature considered.
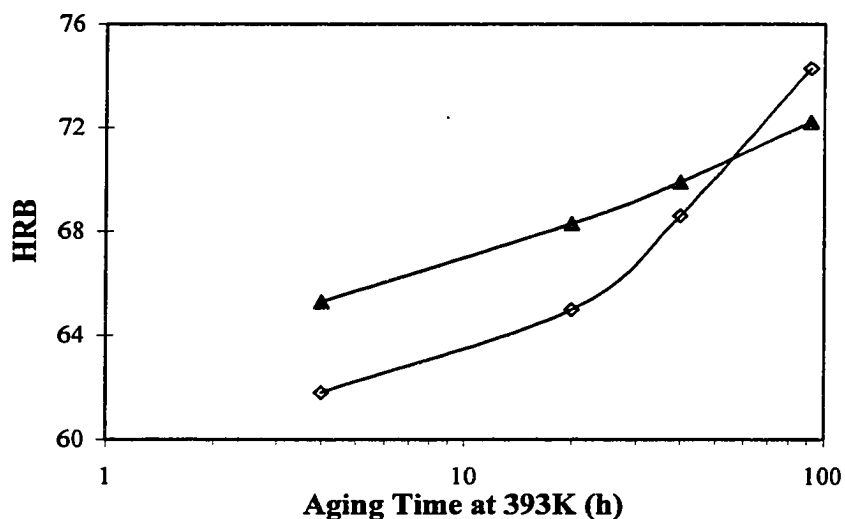
Figure 4.19   Aging response at 393K for an unmodified 2014 standard (▲) and one potentially microalloyed with Li (◇).   A sintering time of 16h was used for each.
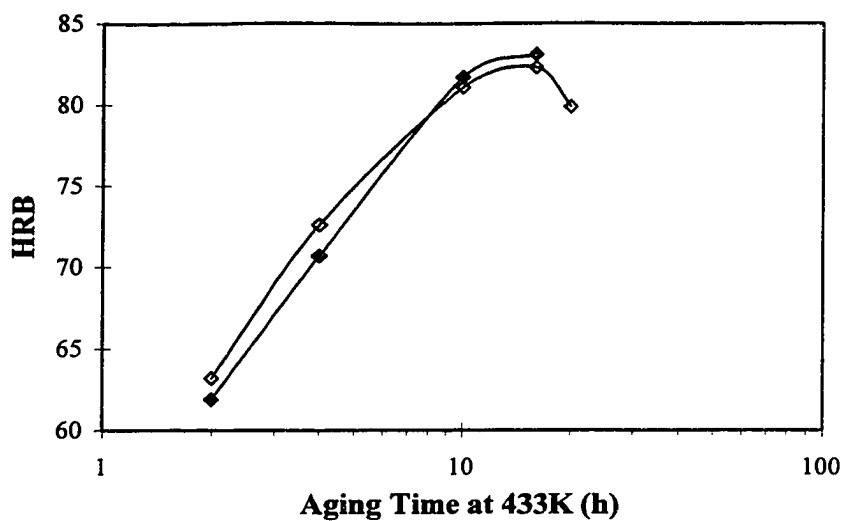
Figure 4.20   Aging response at 433K for an unmodified 2014 standard (♦) and one potentially microalloyed with Li (◇).   A sintering time of 16h was used for each.
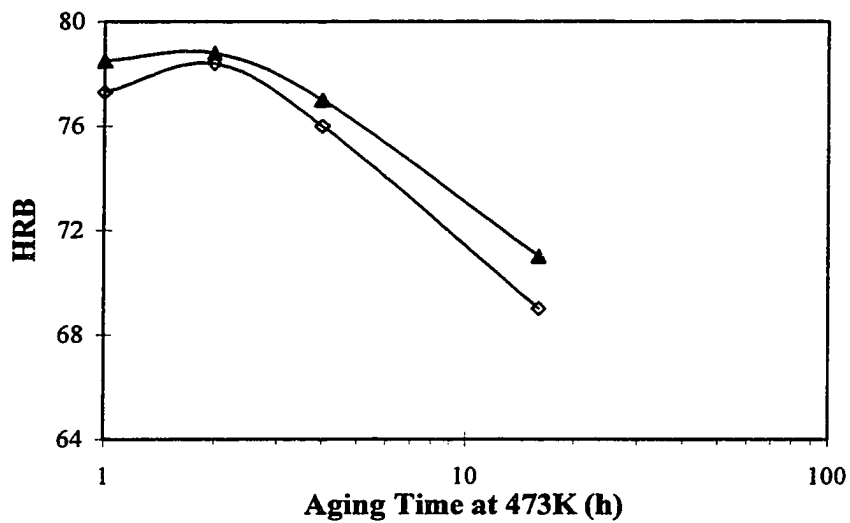
Figure 4.21   Aging response at 473K for an unmodified 2014 standard (▲) and one potentially microalloyed with Li (◇).   A sintering time of 16h was used for each.

4.5   TEM CHARACTERIZATION

In order to determine the dominant precipitate formed in samples aged to the T6 condition (peak hardness) selected samples were prepared and examined using a TEM. The results found for each sample are outlined in the following sections.

4.5.1   Ternary Alloy Standards

Initially, a sample of the ternary alloy sintered for 4h and heat treated to a T6 condition was examined. Using a <100> zone axis, a diffraction pattern (DP) and bright field image (BFI) together with EDS analysis were recorded (Figure 4.22). From the BFI, it is evident that precipitates of uniform thickness (edge-on plates) lie on {100}-type planes. The corresponding DP also gives evidence of such precipitates through the occurrence of streaking in all <100> directions, implying the existence of precipitates on {100} planes. Furthermore, small, faint crosses in the centre of each square unit of four bright diffraction spots were also present. When subjected to EDS analysis, no Ag was detected. DPs were also recorded in <011> and <111> zone axes (Figure 4.23). In the former pattern, streaking is again evident, along the <100> directions, but absent in <111> directions.

Using the same procedure, ternary standards sintered for 2h were examined. All results were very similar to those acquired for samples sintered for 4h and thus, are not included. To illustrate this point, a BFI recorded in a <100> type of zone axis is given in Figure 4.24 together with the respective DP.
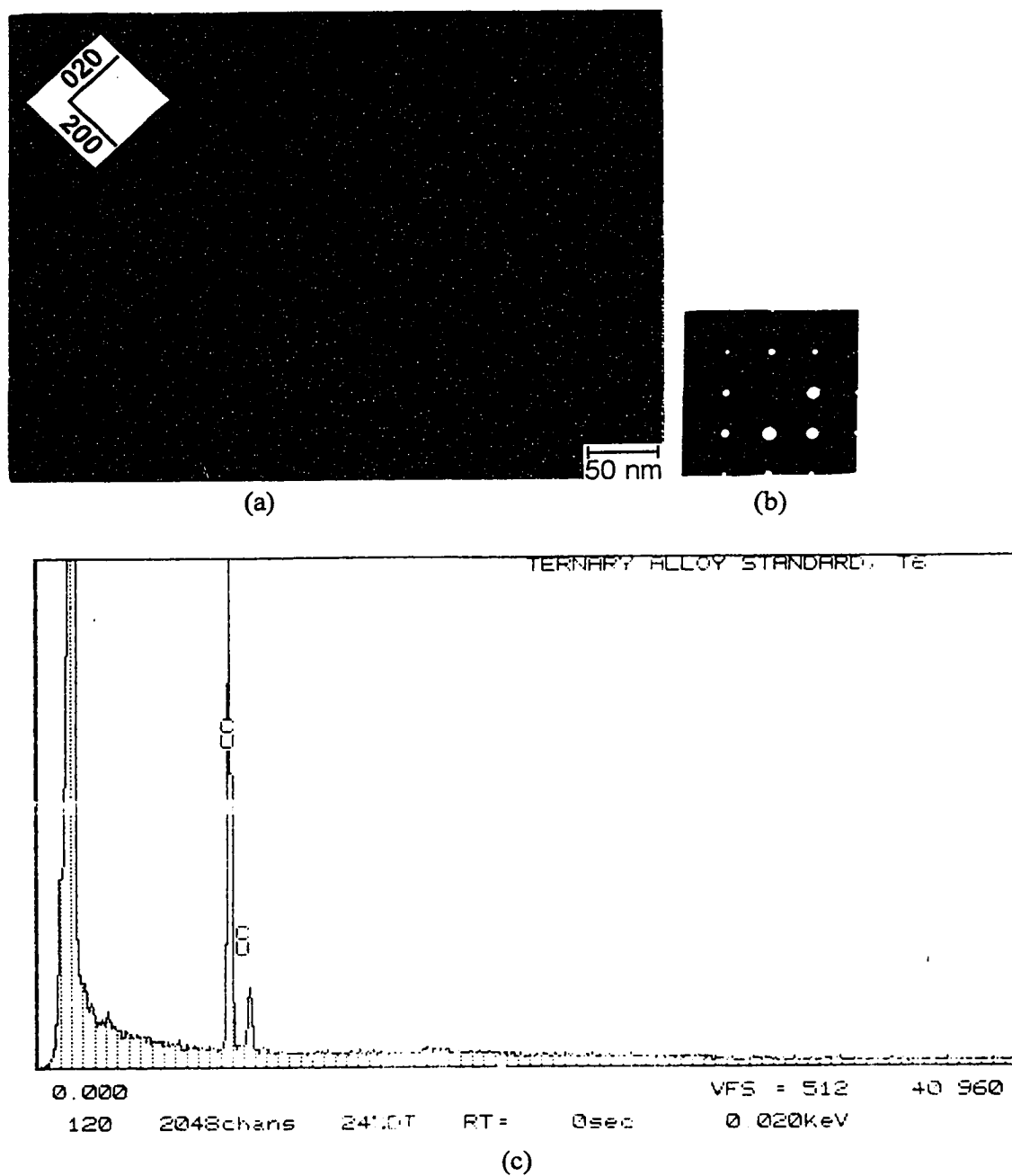
Figure 4.22 Ternary alloy standard sample (4h sinter) examined in a <100> orientation. (a) BFI (b) DP and (c) EDS spectrum for the area.

(a)   (b)

Figure 4.23 DPs recorded near (a)<110> and (b) <111>-types of zone axes for a ternary alloy standard sample sintered 4h.

(a)   (b)
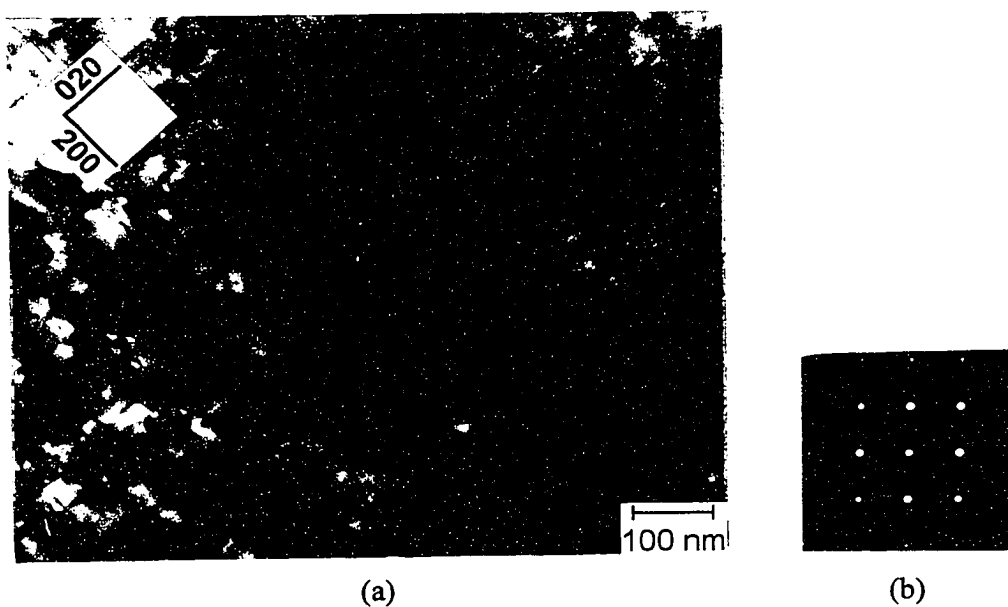
Figure 4.24 Ternary alloy standard (2h sinter) examined in a <100> orientation. (a) BFI and (b) DP.

4.5.2 Ag Modified Ternary

Relative to ternary alloy standards, samples microalloyed with Ag (4h sinter) exhibited significant differences in precipitates. When orienting the sample into a <110> zone axis, the resulting DP exhibited intense streaking along <111> directions with little along a <100> direction (Figure 4.25). By superimposing {111} and {100} planes on the corresponding BFI it is clear that the majority of precipitates lie on the former planes, with few observed on {100} planes. EDS analysis of the region verified the presence of Ag, as required for the θ' to Ω transformation. DPs recorded along <111> and <100> zone axes are given in Figure 4.26. When the <111> diffraction pattern generated from this sample was compared to a recently published computer generated pattern for Ω [142] a strong match was observed. Finally, using a <100> zone axis (Figure 4.26) a small square arrangement of spots within the larger square of bright spots produced from the Al matrix was noted. Also of interest is the recurrence of features found in similar patterns taken from the sample free of Ag (streaking in <100> directions together with faint crosses at the centre of each square of matrix spots).
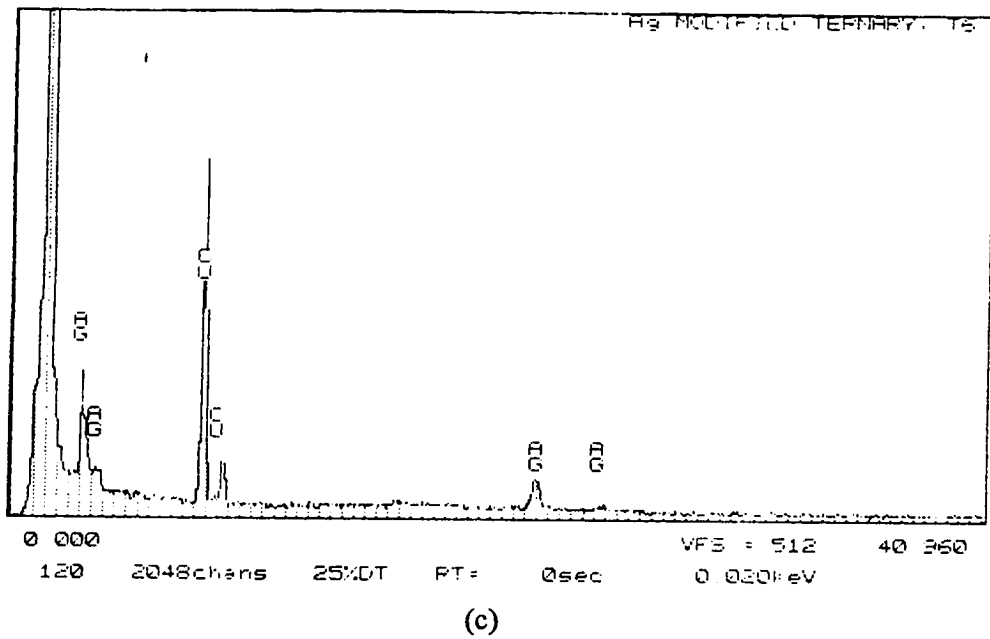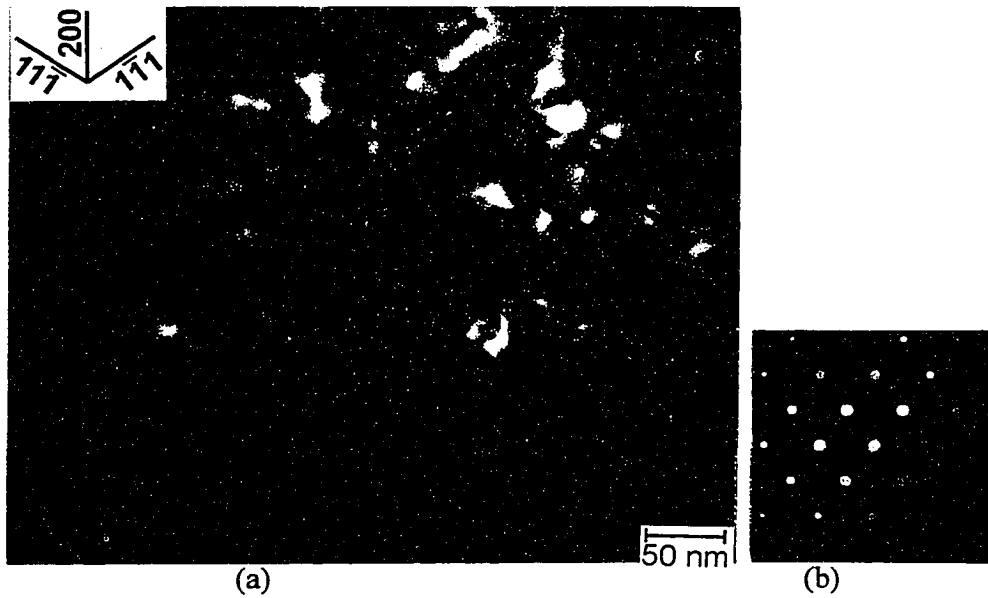
Figure 4.25 Ag modified ternary alloy sample (4h sinter) examined in a <110> orientation. (a) BFI (b) DP and (c) EDS spectrum for the area.

Figure 4.26 DPs recorded near (a)<100> and (b) <111>-types of zone axes for a Ag modified ternary alloy sample sintered 4h.

As a final means of study, precipitates were examined under dark field conditions. The sample was tilted into a <110> orientation, and a BFI and corresponding DP were recorded (Figure 4.27). Centered dark field images (CDFIs) were then formed (Figure 4.28) with the portion of the diffracted beam responsible for the streaks denoted as (a) and (b) in the DP. Evidently, each streak is associated with precipitates that lie on a particular variant of {111} planes. Aside from streaking, an array of two uniformly spaced diffraction spots is also present. Unfortunately, CDFIs generated from these spots were very faint with no discernable details.

When a Ag modified sample sintered for a shorter period of time (2h) was examined, TEM analyses (BFIs, DPs, CDFIs, EDS) were essentially identical to those observed for Ag-containing samples sintered for 4h. To avoid unwarranted duplication, these results are not included.
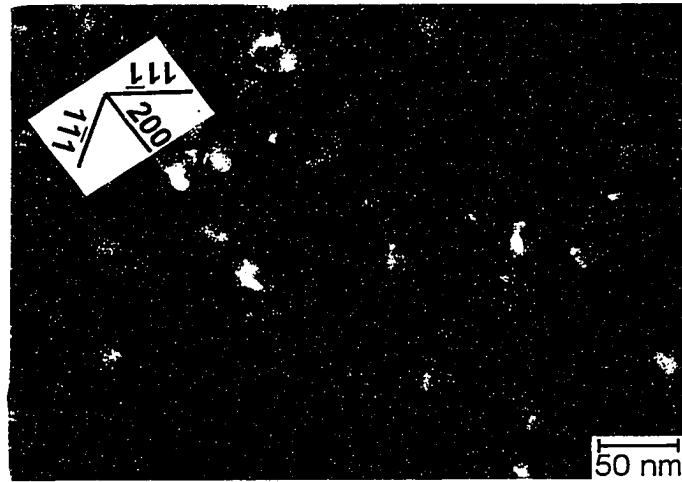
(a)
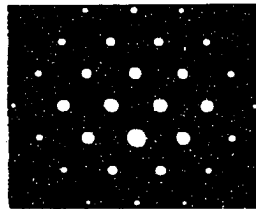
(b)

Figure 4.27 <110> analysis of the precipitates formed in the ternary alloy microalloyed with Ag (4h sinter). (a) BFI, (b) DP.
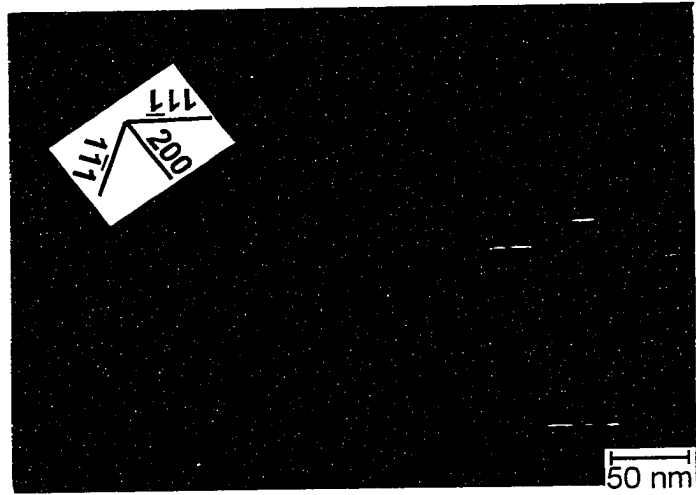
(a)
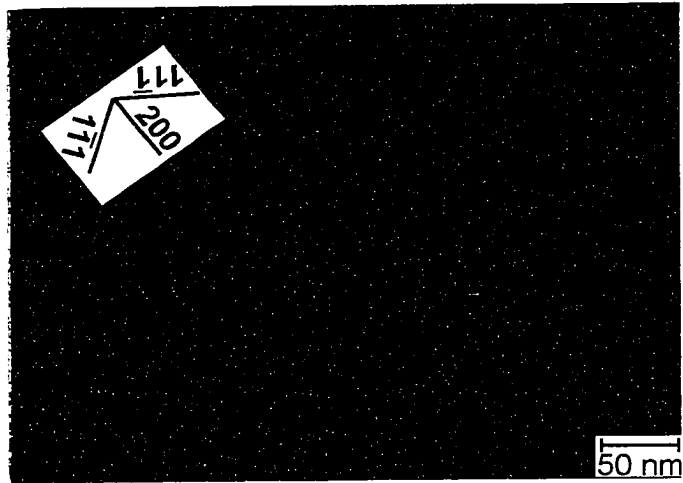
(b)

Figure 4.28 CDFI images corresponding to Figure 4.27. Image generated from (a) streak a and (b) streak b.

4.5.3   2014 Alloy Standards

For P/M 2014 standards, sintering times of 2, 4, and 16h were considered. When examined in a <100> orientation, precipitates of uniform thickness that were parallel to {100} planes were observed.   This morphology was postulated to be plate-like precipitates viewed edge-on and was confirmed by those lying normal to the incident beam. A BFI illustrating an example of this analysis is given in Figure 4.29. Streaking in <100> directions was noted in the corresponding DP as were faint crosses at the centre of each square quadrant of bright matrix reflections.   Additional diffraction patterns recorded in <110> and <111> orientations also indicated the presence of precipitates along {100} planes through streaking in <100> directions (Figure 4.30).

100 nm

(a)   (b)
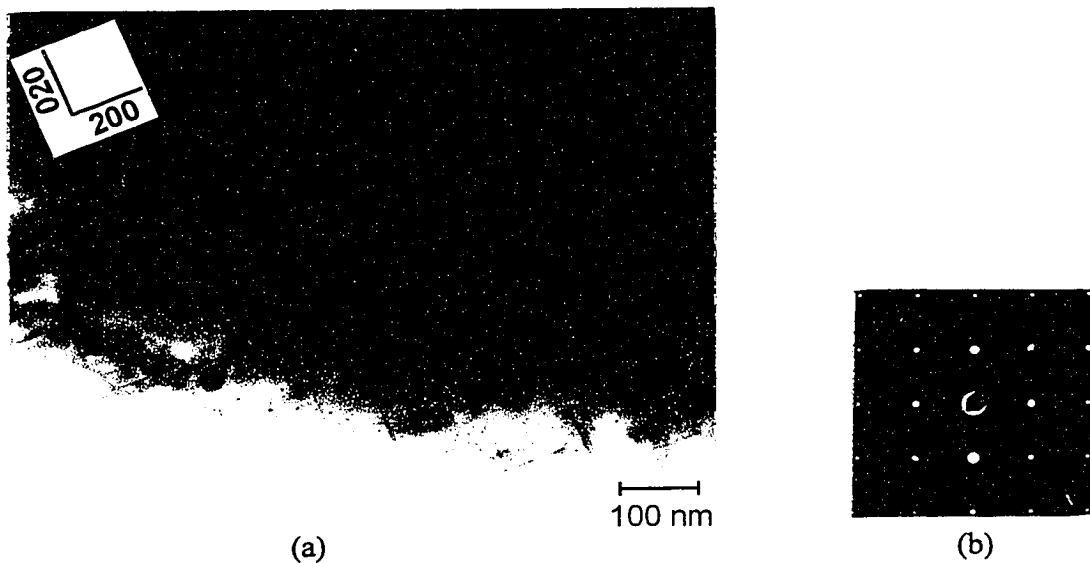
Figure 4.29 P/M 2014 alloy standard (16h sinter) examined in a <100> orientation. (a) BFI and (b) DP.

(a)   (b)
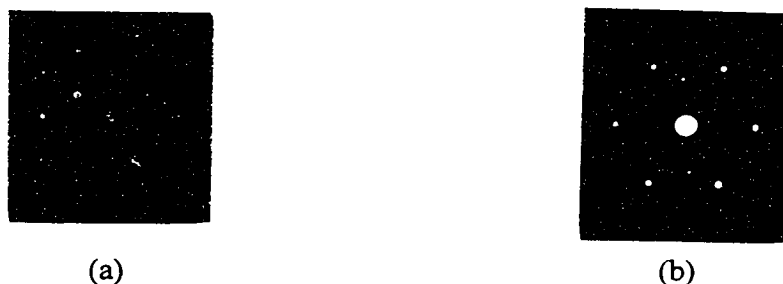
Figure 4.30 DPs recorded near (a) <110> and (b) <111>-types of zones axes for a P/M 2014 alloy standard sample sintered 16h.

4.5.4   Ag Modified 2014

In the analysis of Ag modified samples of P/M 2014, those sintered for 2, 4, and 16h were considered. For the shorter sintering times, analyses in a <100> orientation produced results that were very similar to that found in P/M 2014 standards (Figure 4.31). Additional examinations in <110> and <111> orientations were also similar. For samples sintered 16h, this trend was again apparent in a <100> orientation (Figure 4.32). However, when viewed along <110> (Figure 4.33) and <111> (Figure 4.34) zone axes, evidence suggested that more than one type of precipitate might be present. As shown in the <110> DP, faint streaking in <111> directions was evident. Morphologically, the presence of irregular, hexagonal precipitates were noted (Figure 4.34) when the sample was in a <111> orientation. Only in ternary alloy samples containing Ag were such streaks and precipitate morphologies observed.

(a)   (b)
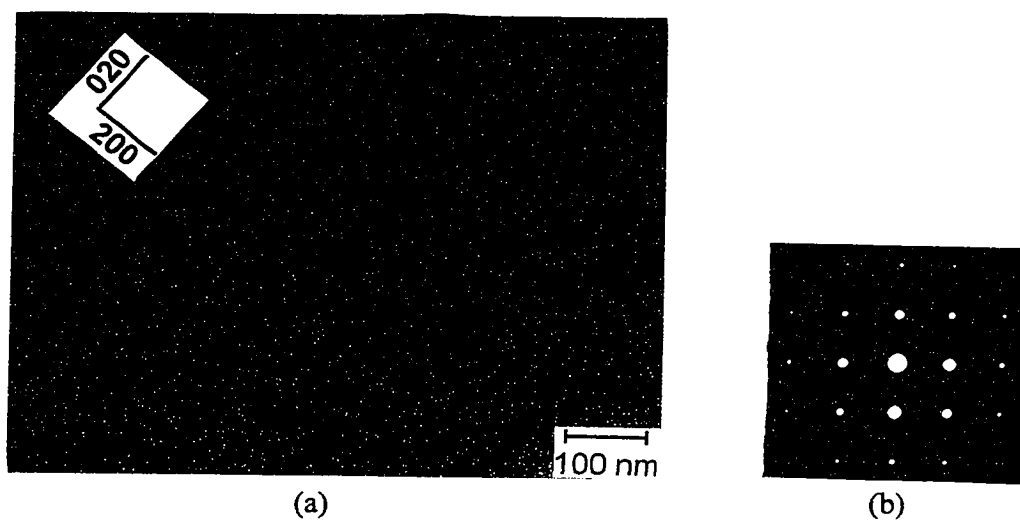
Figure 4.31 Ag modified P/M 2014 (2h sinter) examined in a <100> orientation. (a) BFI and (b) DP.

(a)   (b)
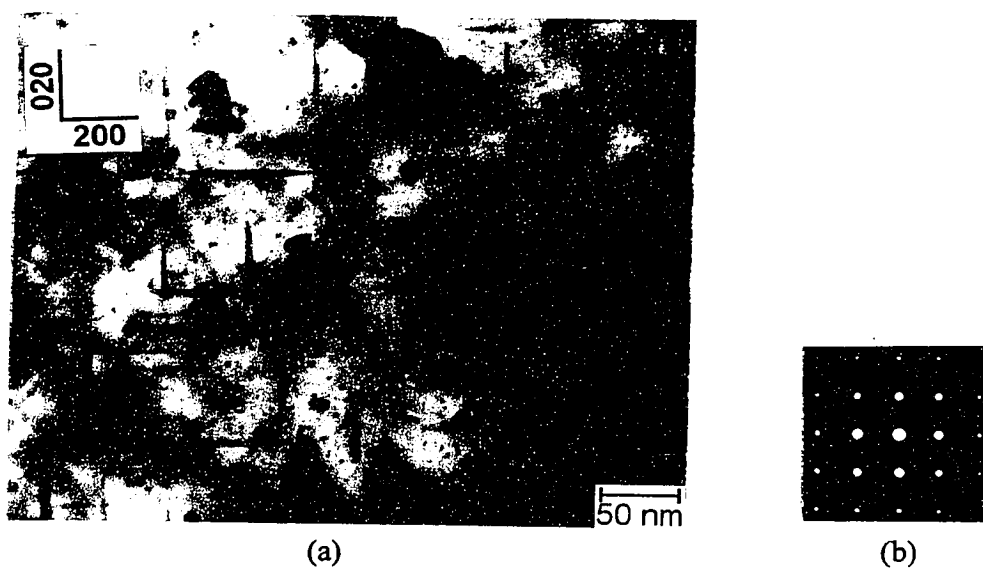
Figure 4.32 Ag modified P/M 2014 (16h sinter) examined in a <100> orientation. (a) BFI and (b) DP.
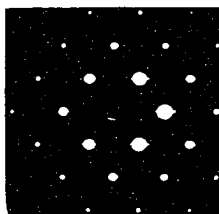
Figure 4.33 DP recorded near a <110> zone axis from a Ag modified P/M 2014 alloy sample (16h sinter).
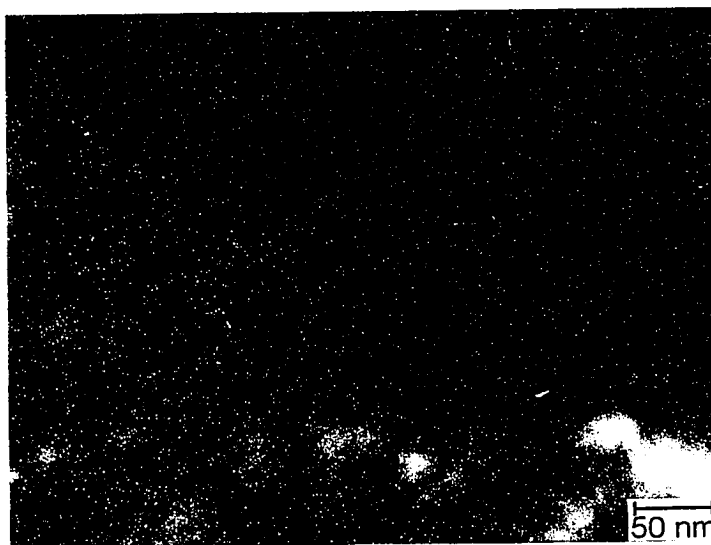
Figure 4.34 Hexagonal shaped precipitates observed in a Ag modified P/M 2014 alloy (16h sinter) when examined in a <111> orientation.

4.6 TENSILE TESTING

To determine the influence of microalloying additions on tensile properties, numerous samples were heat treated into the T6 condition and machined into specimens of suitable geometry. Due to the small dimensions of the sample, the usual procedure of first machining and then heat treating could not be followed. The following sections detail the findings of these tests. Data cited in Tables 4.7 to 4.11 are average values and the complete listing of all data is given in Appendix D.

4.6.1 Ternary Alloy Standards

Engineering stress vs. strain data for ternary alloy standards are given in Table 4.7. As shown, increasing the sintering time from 2 to 4h has a minimal influence on tensile properties. When the appearance of fracture surfaces was examined, extensive dimpling was noted in all samples, indicative of a ductile mode of failure (Figure 4.35).

Table 4.7   Summary of engineering tensile properties measured for ternary alloy standards sintered for 2 and 4h.

	HV (1kg)	Yield Strength (MPa)	UTS (MPa)	Elongation at Fracture (%)
2h Sinter	112	340	406	15.5
4h Sinter	109	342	410	14.8
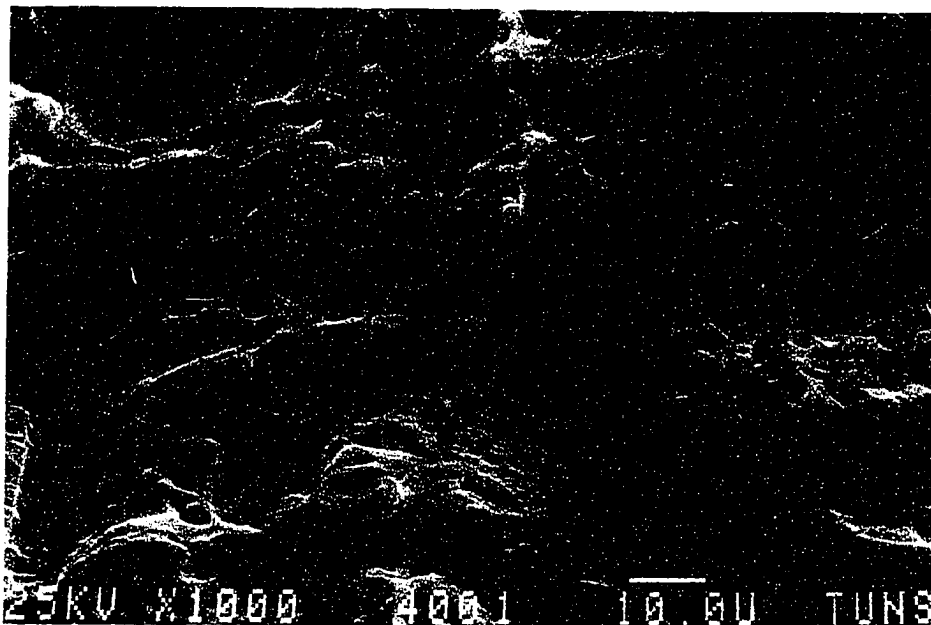
Figure 4.35   Appearance of a fracture surface produced in a ternary alloy standard sintered for 4h.

4.6.2 Ag Modified Ternary

Results of tensile tests conducted on Ag modified samples of the ternary alloy after sintering for 2 and 4h are given in Table 4.8. Relative to the unmodified ternary alloy data, those containing Ag exhibit a significant improvement in both yield strength and ultimate tensile strength at the expense of a reduction in ductility. Such samples are, however, similar to their standard counterparts in that the sintering time again had minimal influence. SEM analysis of fracture surfaces (dimpled) indicated a ductile mode of failure (Figure 4.36).

Table 4.8 Summary of engineering tensile properties measured for Ag modified ternary alloy samples sintered for 2 and 4h.

	HV (1kg)	Yield Strength (MPa)	UTS (MPa)	Elongation at Fracture (%)
2h Sinter	134	394	429	12.7
4h Sinter	141	401	446	12.3
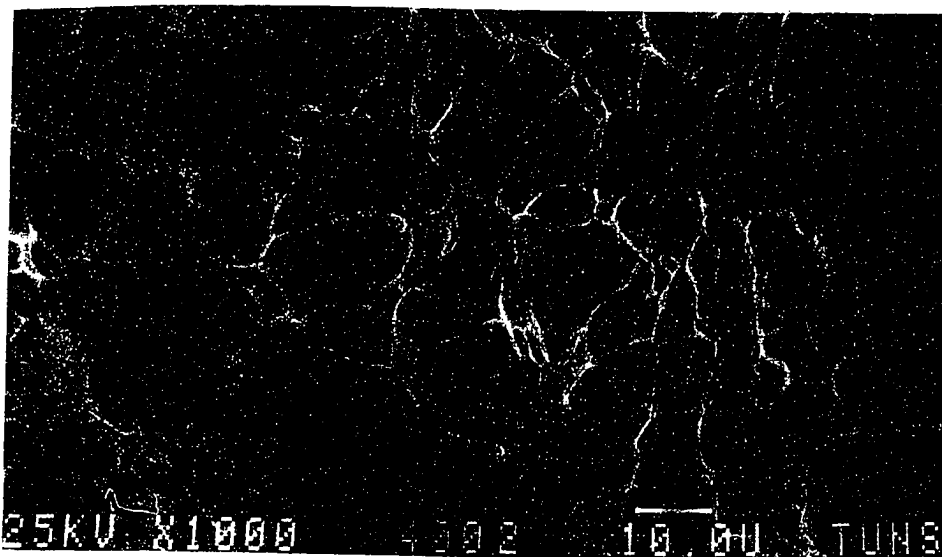
Figure 4.36 Appearance of a fracture surface produced in a Ag modified ternary alloy sample sintered for 4h.

4.6.3   2014 Alloy Standards

Because is was suspected that P/M 2014 might behave differently with respect to mechanical properties relative to the standard P/M ternary alloy, initial testing again focused on alloy 2014 standards and the influence of sintering time (0.5, 2, and 16h) on tensile strength. The results of these tests are summarized in Table 4.9. For comparison, literature data for wrought 2014 are also given. The slight decrease in elongation for the P/M samples may be due to the presence of the thin oxide layer formed on the aluminum alloy particles. As sintering time is prolonged, it is evident that a decrease in yield and tensile strengths occurs. Although this is not significant amongst samples sintered for shorter lengths of time (0.5 and 2h), extending this time to 16h promotes a significant reduction. This is likely due to grain coarsening during sintering. There is, however, a slight improvement in ductility with sintering time. When examined in an SEM, a ductile mode of failure (dimpling) was prevalent in all samples. An example of this behaviour is given in Figure 4.37.

Table 4.9 Comparison between engineering tensile properties of P/M alloy 2014 standard samples sintered for various times and wrought 2014.

Sample	Sintering Time (h)	HRB	Yield Strength (MPa)	UTS (MPa)	Elongation at Fracture (%)
Wrought 2014[1]	----	80-86	415	485	13
P/M 2014	0.5	86	454	513	10.6
P/M 2014	2	85	465	502	9.7
P/M 2014	16	81	436	488	11.4

1 Data as cited in [19]
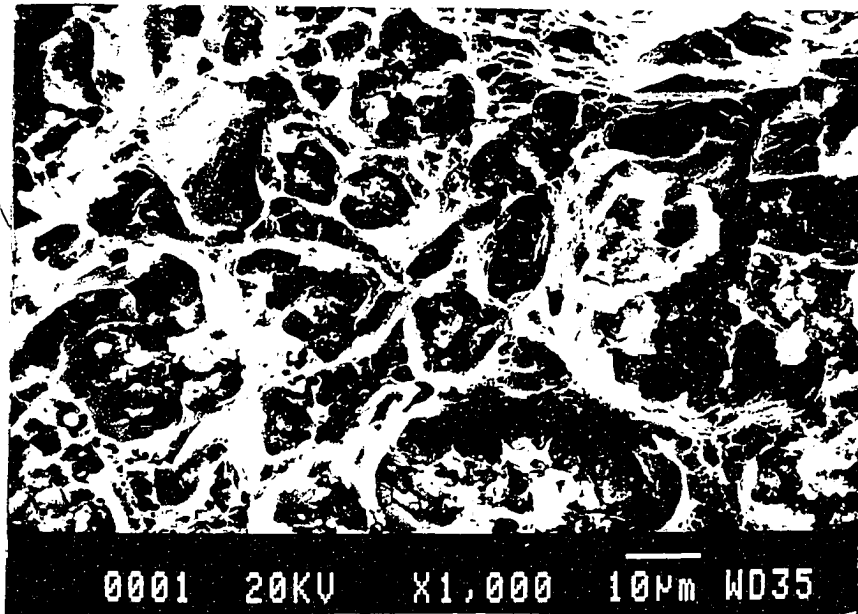
Figure 4.37 Appearance of a fracture surface produced in a P/M 2014 alloy standard sintered for 0.5h.

4.6.4 Ag Modified 2014

A summary of the tensile properties for samples microalloyed with Ag is given in Table 4.10. As shown, those samples sintered for shorter periods of time (2 and 4h) exhibit minimal differences in tensile properties. Thus, it is suggested that such variations in sintering time again have minimal influence. Although measured values are marginally lower than those for equivalent alloy standards, it is interesting to note that improvements over the standard were measured in some instances. Unlike the ternary alloy system, the tensile behaviour of 2014 is not significantly affected by Ag addition. SEM examination of fracture surfaces revealed extensive dimpling, indicative of a ductile mode of fracture.

Table 4.10 Engineering tensile properties for Ag modified P/M 2014 samples sintered for 2 and 4h.

Sample	HRB	Yield Strength (MPa)	UTS (MPa)	Elongation at Fracture (%)
2h Sinter	85	446	497	11.2
4h Sinter	86	464	513	9.9

4.6.5 Sn Modified 2014

As previously mentioned, it was often difficult to avoid cracking during the hot swaging of Sn modified samples. Although swaged rods previously sintered for 0.5, 1,2,3,4,8, and 16h were produced for tensile specimens, only the select few that appeared uncracked were machined and tested. The results of these limited tests are shown in Table 4.11. From the data gathered it appears that the addition of Sn has a negative effect on tensile strength, and that this effect becomes increasingly deleterious as the sintering time, and in turn Sn content, is raised. When fracture surfaces of the tested specimens were examined, a tendency towards intergranular failure was observed. Examples of this trend are given in Figure 4.38.

Table 4.11 Engineering tensile properties for Sn modified P/M 2014 samples sintered for 0.5, 1, and 3h.

Sample	HRB	Yield Strength (MPa)	UTS (MPa)	Elongation at Fracture (%)
0.5h Sinter	86	477	514	10.9
1h Sinter	85	449	493	10.5
3h Sinter	81	423	470	11.4
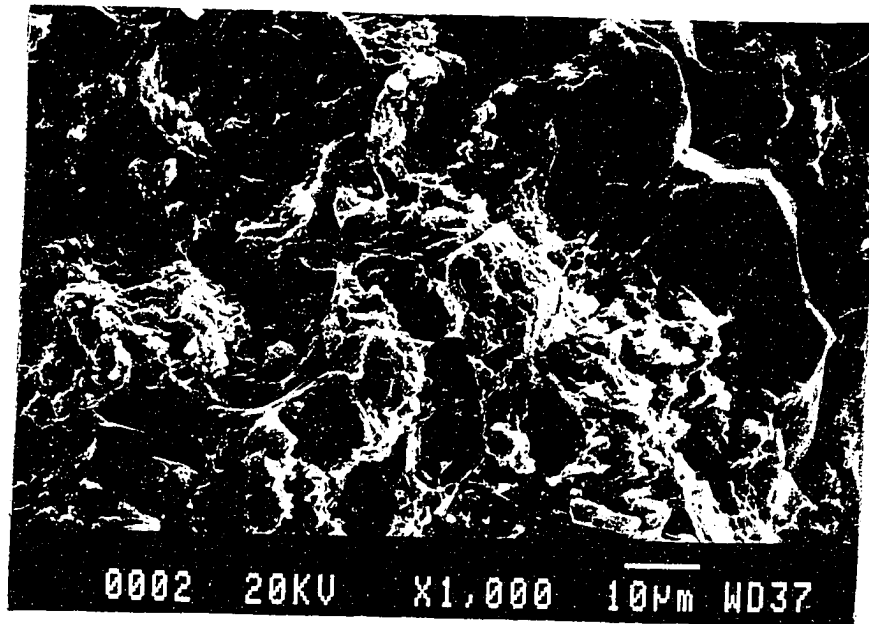
(a)
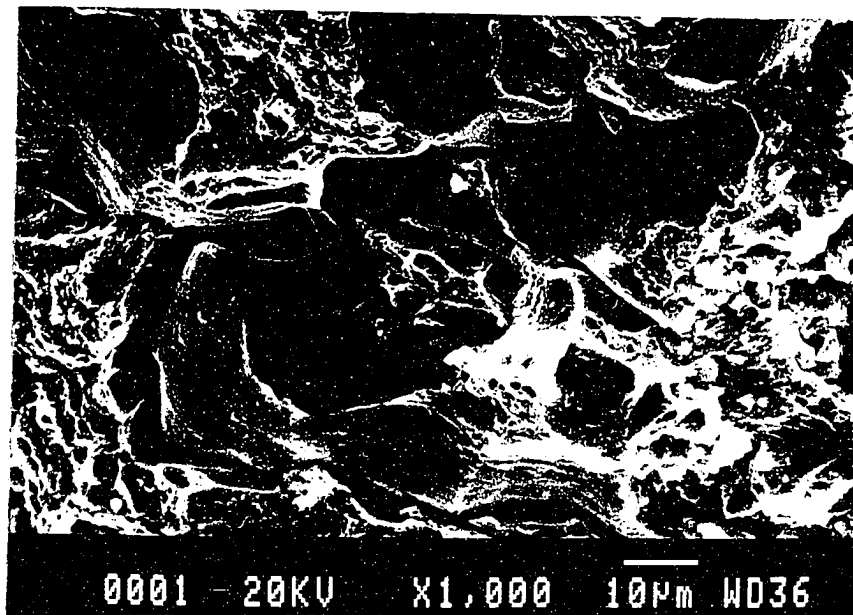
(b)

Figure 4.38 Appearance of fracture surfaces produced in Sn modified P/M 2014 samples sintered for (a) 1h and (b) 3h.

4.6.6   Li modified 2014

Several samples previously sintered for 16h were hot swaged, heat treated, and machined into tensile specimens. Results of these tests indicated an average yield strength of 410 MPa, UTS of 475 MPa, and elongation of 15%. These results are slightly lower than an equivalent 2014 standard.

4.7   WEAR TESTING

The following sections detail the results gathered during the assessment of dry sliding wear behaviour. Aspects considered included weight loss as a function of load, sintering time and Sn content. All numerical data shown are average values and a complete listing of all data is given in Appendix D. Wear track morphology, and wear debris were also examined.

4.7.1   Weight Loss vs. Applied Load

To establish a baseline, the wear behaviour of 2014 P/M standards was first considered. Results of normalized weight loss vs. applied load are shown in Figure 4.39; little difference occurs between samples sintered for time periods of 0.5 and 16h. Also included in the figure are data for wrought 2014. Apparently, this I/M product possesses better wear resistance than the P/M counterparts produced in this work. The improvement over P/M is quite consistent and the largest difference occurs at a load of 20N.

Results of normalized weight loss vs. applied load for samples microalloyed with either Sn or Ag are shown in Figures 4.40 and 4.41 respectively. Although a gradual improvement in wear resistance with prolonged sintering time was noted for samples
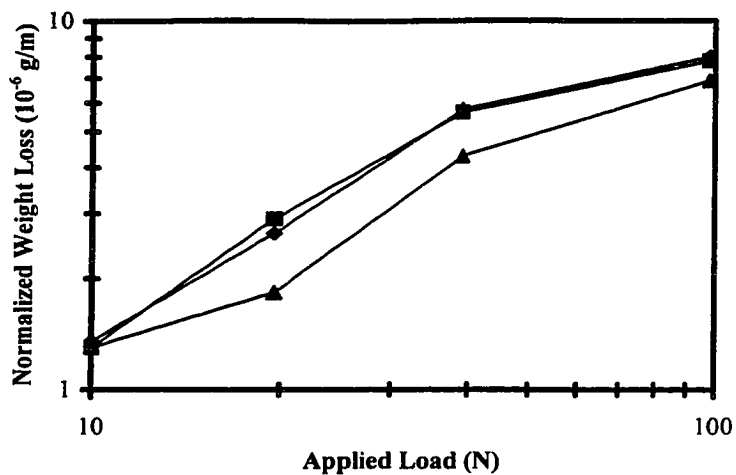
Figure 4.39 Normalized weight loss ($\times 10^{-6}$ g/m) vs. applied load for wrought 2014 (▲) and

P/M 2014 standards sintered for 0.5h (♦) and 16h (■).
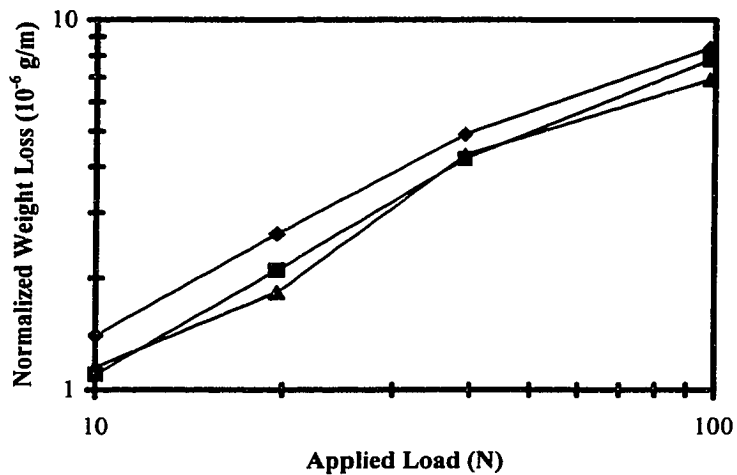
Figure 4.40   Normalized weight loss ($\times 10^{-6}$ g/m) vs. applied load for P/M 2014 microalloyed with Sn when sintered for 0.5h (♦), 2h (■), and 4h (▲).
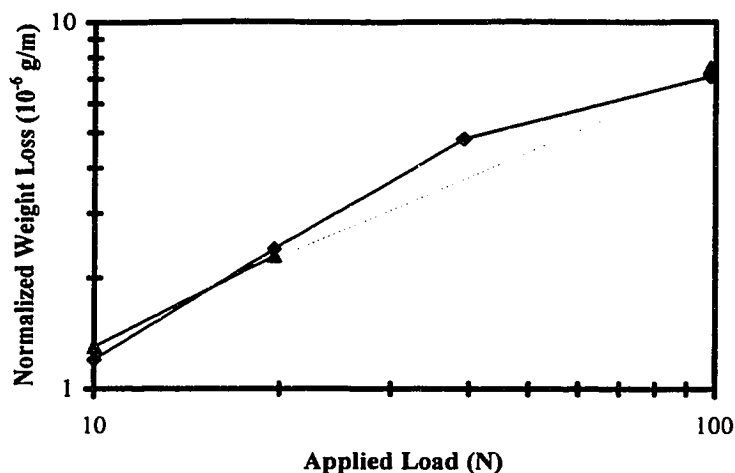
Figure 4.41 Normalized weight loss (x10⁻⁶ g/m) vs. applied load for P/M 2014 microalloyed with Ag when sintered for 4h (♦) and 16h (▲).

microalloyed with Sn, little difference was noted between those containing Ag. As with P/M standards and wrought material, the greatest variation in wear resistance again occurred at an intermediate load of 20N.

4.7.2 Wear Track Morphology

Examination of wear tracks revealed similar trends of morphology change with applied load, regardless of the sample under consideration. As examples, micrographs of the wear track morphologies generated on an alloy P/M standard sintered for 0.5h and Sn modified 2014 sintered for 4h are shown in Figures 4.42 and 4.43. In all cases, a load of 20N generated a track that was comprised of rough craters (labeled "C") and flat grooved sections (labeled "F"). Further examination at higher magnification revealed that each possessed a very fine microstructure. Within the craters, the microstructure resembled a fracture surface. However, the flat regions were composite in nature, comprised of sub-micron particles embedded within a matrix component. Using EDS, elevated levels of
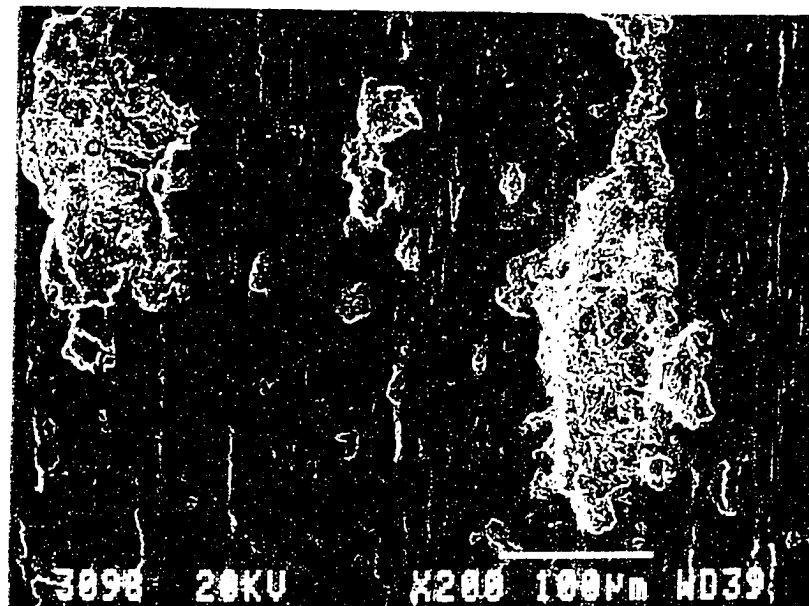
(a)
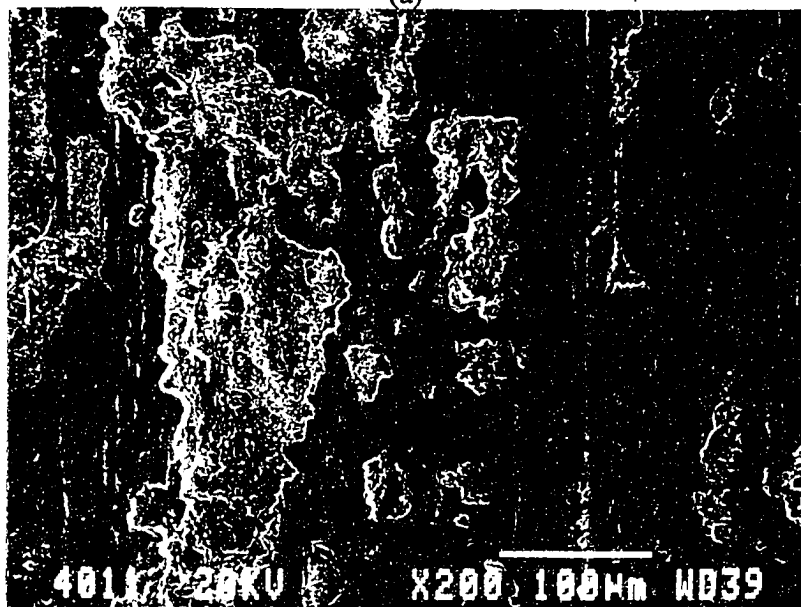
(b)

Figure 4.42   Wear track developed on (a) P/M standard sintered for 0.5h and (b) Sn modified 2014 sintered for 4h, using an applied load of 20N.   Cratered and flat regions labeled with "C" and "F" respectively.
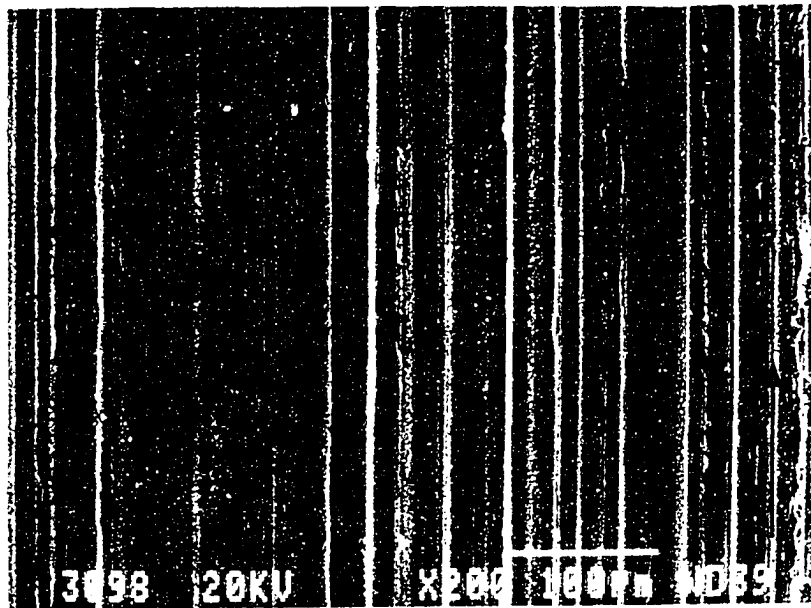
(a)
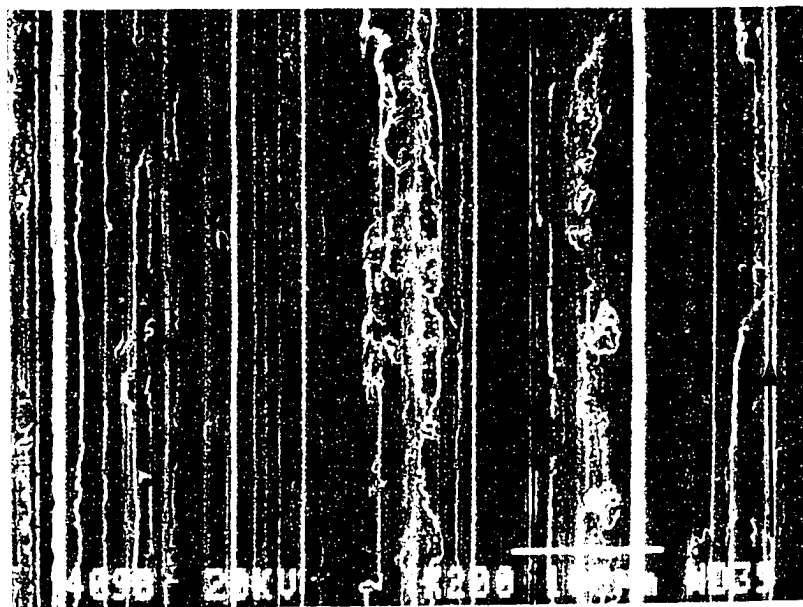
(b)

Figure 4.43 Wear track developed on (a) P/M standard sintered for 0.5h and (b) Sn modified 2014 sintered for 4h, using an applied load of 98N.

iron were detected in the worn surface. Although these measured iron contents varied considerably, those recorded within the craters were consistently higher than those found in adjacent flat regions (i.e. 10 % vs. 20 % respectively). Additional EDS data revealed that both areas were substantially oxidized. Small amounts of molybdenum, tungsten, chromium and vanadium were also detected; each of these is an alloying element in M2 tool steel. Increases in applied load caused the cratering aspect to diminish, and a flat, grooved morphology eventually became the dominant feature.

4.7.3   Wear Debris

As with wear track morphology, the nature of the wear debris for a given load also exhibited a certain degree of similarity. Material collected during tests run at the lighter loads (Figure 4.44) was primarily powdery together with small plate-like particles. Whereas each contained an elevated iron content, that found in the former was consistently higher.

Despite increasing the applied load to 98N, the debris remained as a mixture of the two morphologies; however, the size and quantity of plates were found to increase for all specimen types. EDS analysis again showed a higher iron content within the powder as opposed to the plates, and an elevated level of oxides in both. Although these trends were consistent for each sample type, dissimilarities also existed. For example, in P/M samples, considerable scatter was noted for the iron content from plate to plate; some were similar to that of loose powder, whereas others were almost free of iron, with a composition similar to that of 2014. This observation was not noted in debris generated from the wrought product. As well, the quantity of plate-like particles found in the debris varied. Although wrought, P/M standards and Sn modified samples of 2014 all exhibited similar fractions of these particles, those generated from Ag modified samples were consistently higher, with the 16h sample having almost 100% plate-like particles (Figure 4.45).
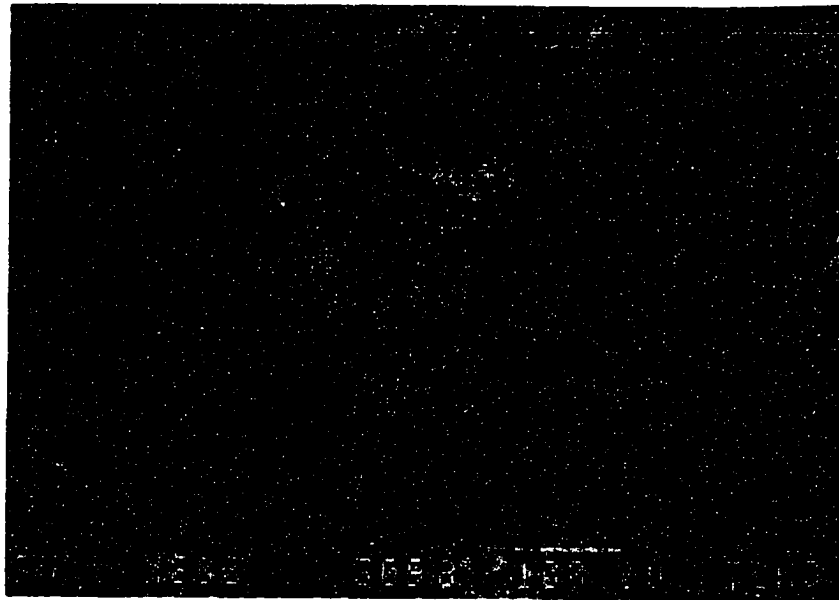
(a)
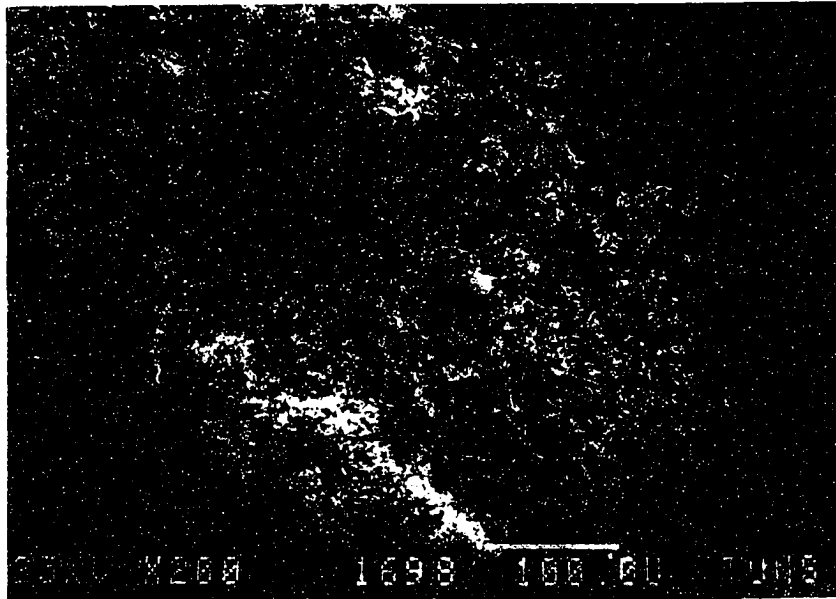
(b)

Figure 4.44 Debris collected from tests run at an applied load of 20N from (a) P/M 2014 standard sintered for 0.5h and (b) Ag modified sample sintered for 16h.
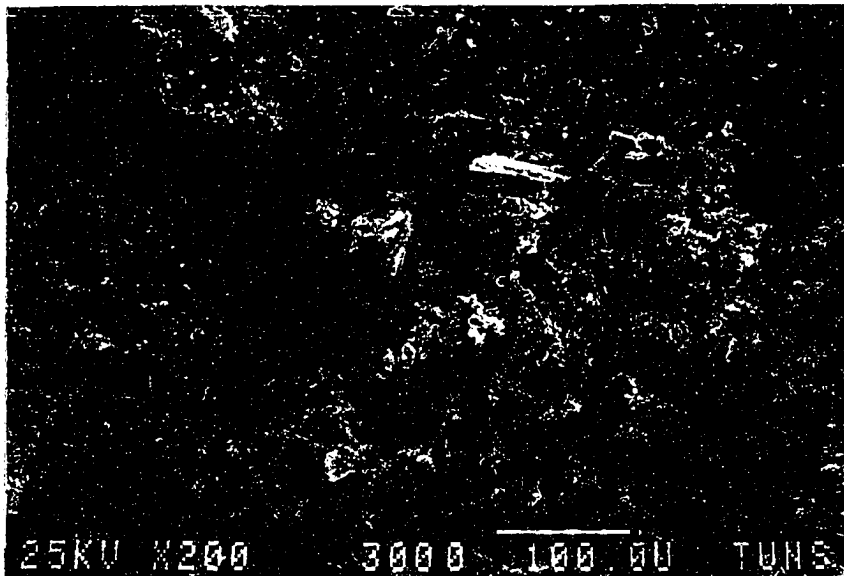
(a)
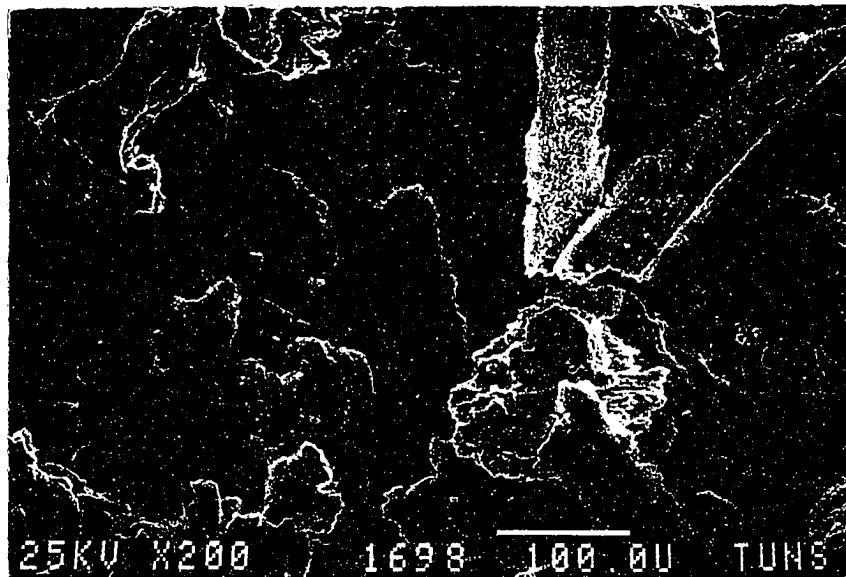
(b)

Figure 4.45 Debris collected from tests run at an applied load of 98N from (a) P/M 2014 standard sintered for 0.5h and (b) Ag modified sample sintered for 16h.

Examples of XRD spectra generated for wear debris using a load of 98N are shown in Figure 4.46. In all spectra gathered, a large, broad peak was noted, covering a range of 2θ approximately 14° to 34°. When using a glass slide containing no debris, a single, broad peak, was also noted at low 2θ values; thus, any contribution of this peak to phase identification was discounted. Additional features included a sharp main aluminum peak and a somewhat broadened peak corresponding to Fe (110) overlapping with a secondary peak of aluminum (Al (200)). Using the spectra of data collected from a P/M standard sintered for 0.5h, the latter peak was magnified and examined. Enlarged views of this peak together with overlaying stick patterns for several of the intermetallic phases possible are shown in Figure 4.47. Minor peaks at higher 2θ values were also found to correspond to aluminum and iron.
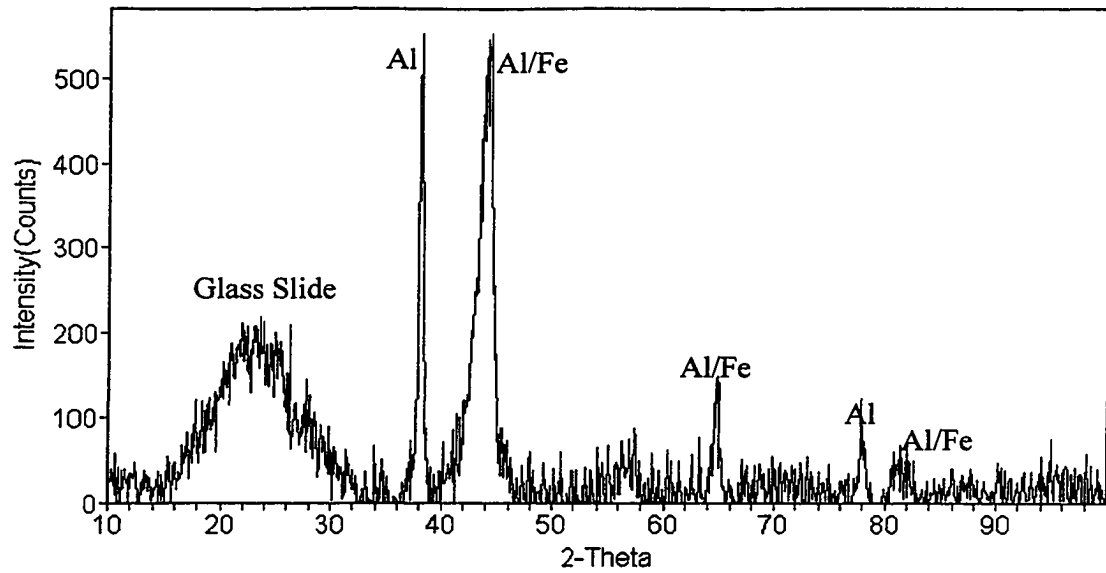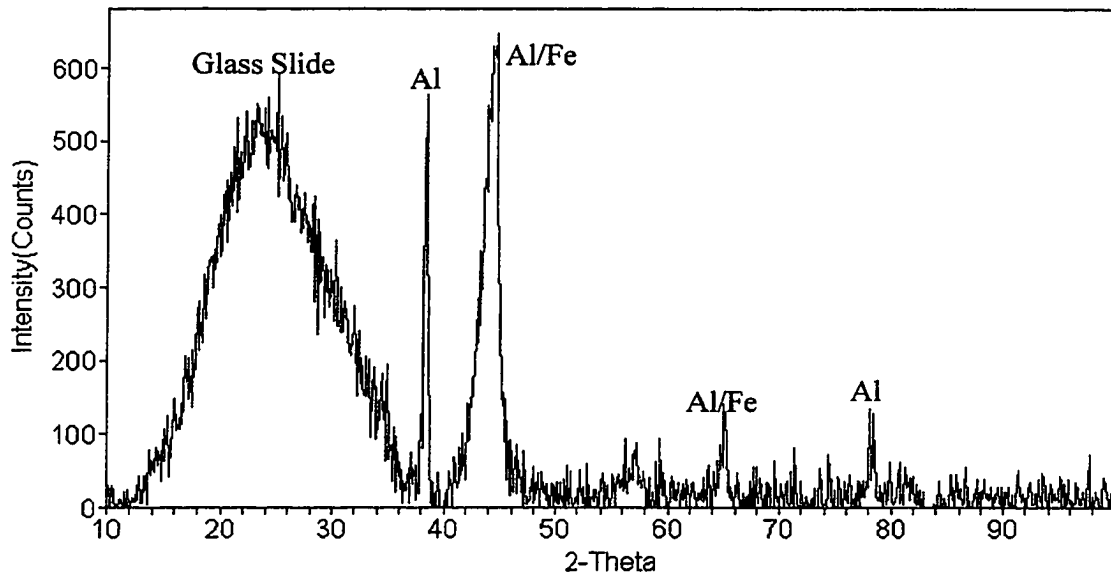
Figure 4.46 Examples of XRD spectra of wear debris collected under an applied load of 98N for (a) P/M 2014 standard sintered for 0.5 h and (b) Sn modified 2014 sintered for 4h.
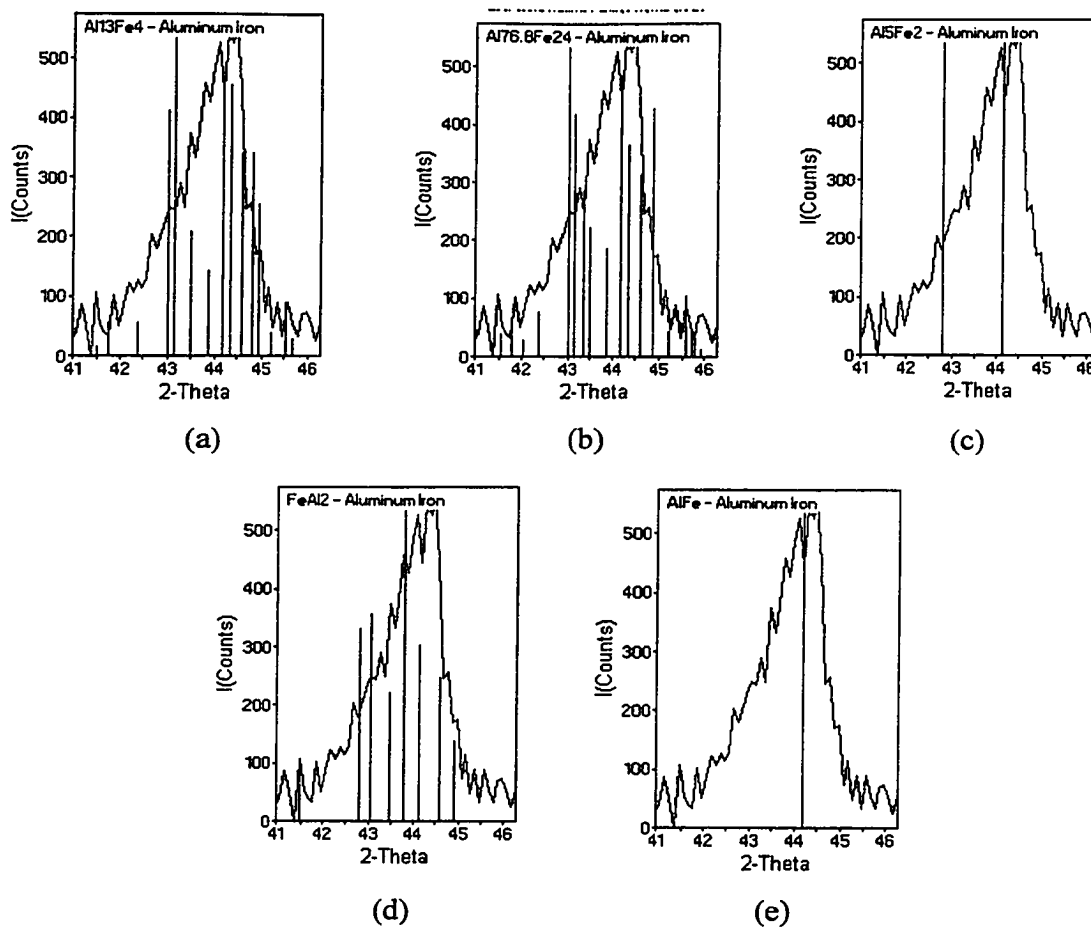
Figure 4.47 Magnified views of the broad Fe(110)/Al(200) peak. Debris was gathered from a P/M 2014 standard sintered for 0.5h and tested under an applied load of 98N. Simulated stick patterns for (a) $Al_{14}Fe_4$, (b) $Al_{76.8}Fe_{24}$, (c) Al_5Fe_2, (d) Al_2Fe and (d) AlFe.

4.7.4   Wear Rate vs. Sintering Time

In prior sections it has been shown that the most significant differences in weight loss induced by wear consistently occurred under an applied load of 20N. Plotting these results as a function of sintering time (Figure 4.48) revealed several interesting trends. First, for P/M 2014 standards, there is an apparent loss in wear resistance as the sintering time is raised. In contrast, microalloyed samples show an increase in wear resistance with sintering time, the greatest improvements being for those microalloyed with Sn. Wear resistance also correlated with Sn content as measured through bulk area EDS analyses (Figure 4.49).
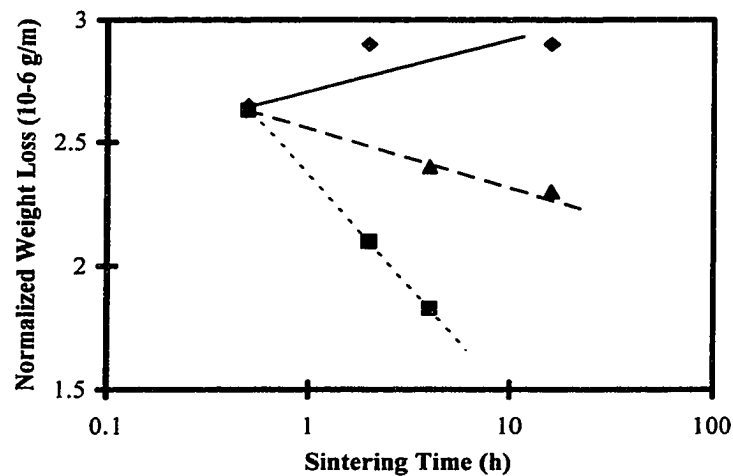
Figure 4.48 Normalized weight loss $(x10^{-6}$ g/m) as a function of sintering time for P/M standard (♦), Sn modified (■) and Ag modified 2014 (▲) (applied load of 20N).
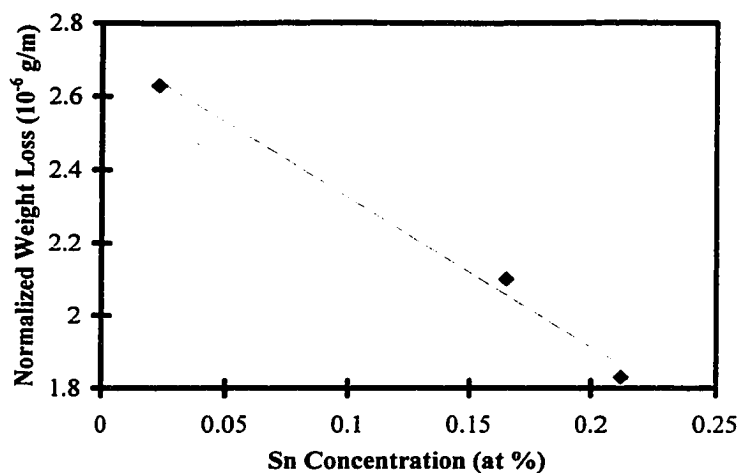
Figure 4.49 Normalized weight loss ($\times 10^{-6}$ g/m) as a function of Sn content (applied load of 20N).

4.8 CORROSION TESTING

As noted earlier, aluminum alloys can exhibit excellent corrosion resistance although some are vulnerable to attack. Amongst those most susceptible to corrosion are members of the 2xxx series of commercial aluminum alloys, an example being alloy 2014 [77]. Thus, knowledge of the corrosion behaviour of this alloy and any effects that further microalloying may have on it is essential. In order to assess the corrosion rate of any given alloy within a particular solution, one approach is to measure polarization resistance curves. In this procedure, a voltage is applied between the sample (working electrode) and a graphite rod (reference electrode) and the resulting current is measured with an ammeter. As the current is increased, the potential of the working electrode is concurrently measured, but through use of a potentiometer-electrometer circuit. The resultant data is then plotted on semi-logarithmic scale graph paper and tangents (Tafel lines) are drawn to the cathodic (lower) and anodic (upper) sections. The governing

corrosion current (Icorr) is then dictated by intersection point of the tafel lines at the corrosion potential (Ecorr). Once substituted into the formula:

Corrosion Penetration Rate (mm/y) = 0.00327 $(ai/n\rho)$

where,

a	=	atomic weight of the metal
i	=	current density ($\mu A/cm^2$);
n	=	number of electrons lost (valence change)
ρ	=	density (g/cm^3).

values for the corrosion rate may be calculated. An example of this procedure is shown in Figure 4.50. The same procedure was applied to P/M (standards, Sn, and Ag modified) and wrought versions of alloy 2014; the results for each are detailed in the following sections.
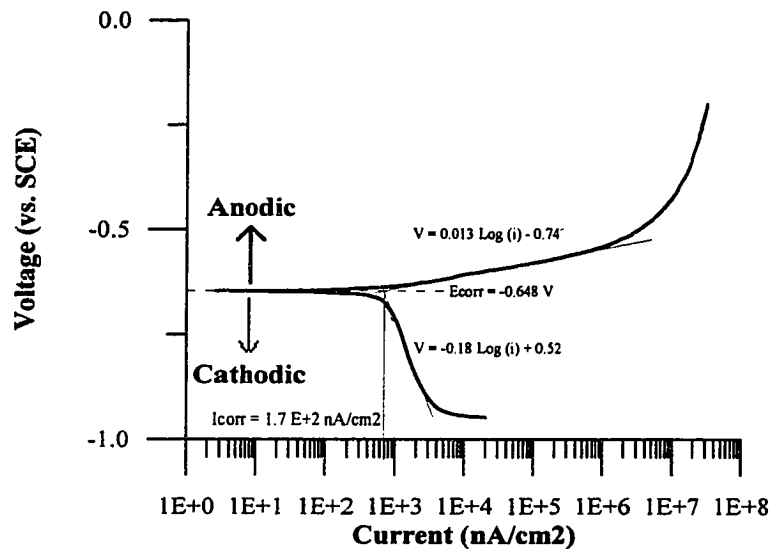
Figure 4.50 Determination of the corrosion current from a polarization curve using tafel lines. Specimen was a P/M 2014 standard sintered for 2h (T6).

4.8.1 2014 Alloy Standards

Polarization curves generated for P/M 2014 standards sintered for times of 0.5, 1, and 2h are shown in Figure 4.51. Each sample has responded in a similar manner, with only minimal differences in corrosion potential, current, and in turn, rate. The only exception was noted in the cathodic portion of the polarization curve for the specimen sintered for 1h. A summary of the data together with calculated corrosion rates is presented in Table 4.12.

To assess the influence of processing means on corrosion resistance, samples of wrought 2014 were tested for comparison. Relative to a P/M counterpart (Figure 4.52), both samples have nearly identical corrosion potentials and exhibit similar behaviour in both the anodic and cathodic portions. The corrosion rate of the wrought alloy is greater, due to an apparent shift of the entire curve to higher current densities.
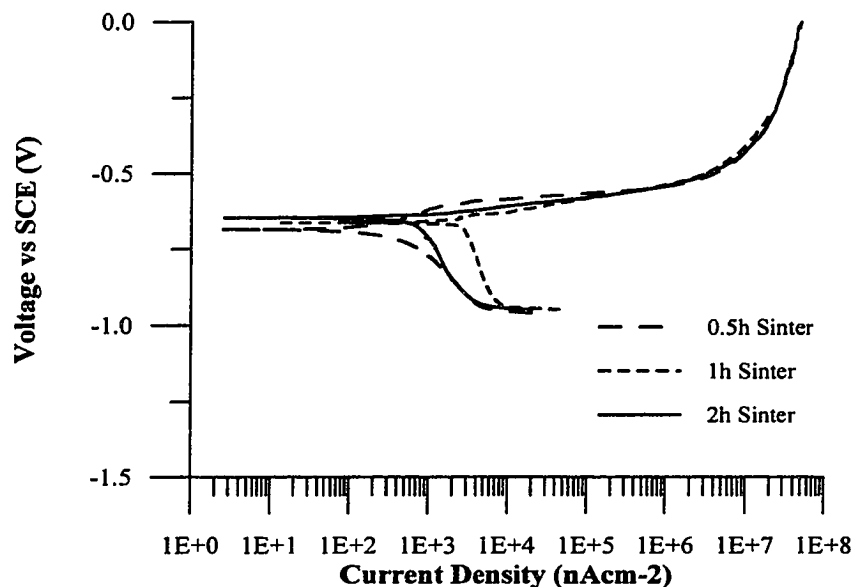
Figure 4.51 Polarization curves for P/M 2014 standard samples sintered for 0.5, 1, and 2h.
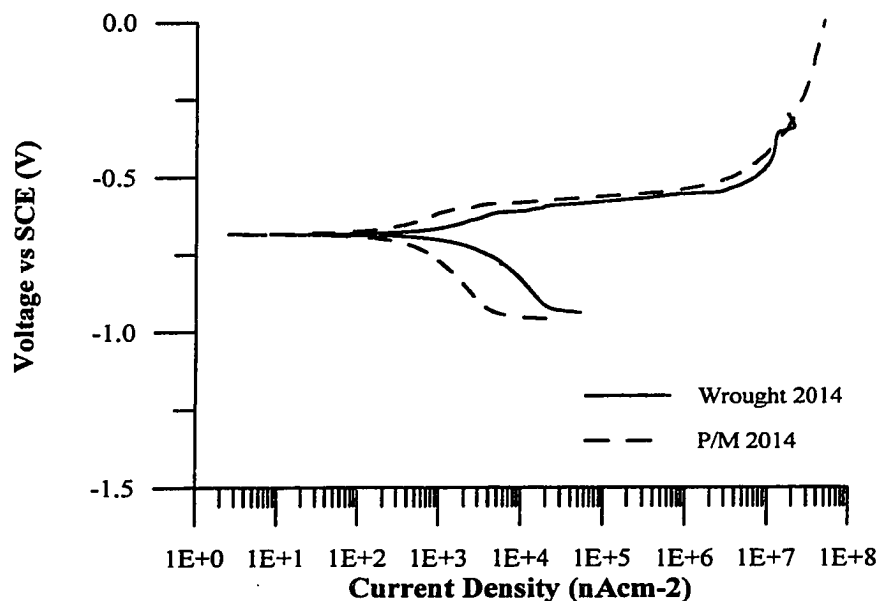
Figure 4.52 Polarization resistance curves for P/M and wrought versions of alloy 2014.

4.8.2   Ag Modified 2014

Polarization resistance curves for samples of P/M 2014 microalloyed with Ag are given in Figure 4.53. As shown, a considerable variation exists between the results. For the sample sintered 4h, a relatively high corrosion rate was measured. Relative to all other corrosion rates, this was the highest measured. However, the rate measured for the 16h sample was comparable to that found for P/M 2014 alloy standards. Only minor differences in the corrosion potential were observed, despite the variation in corrosion rate.
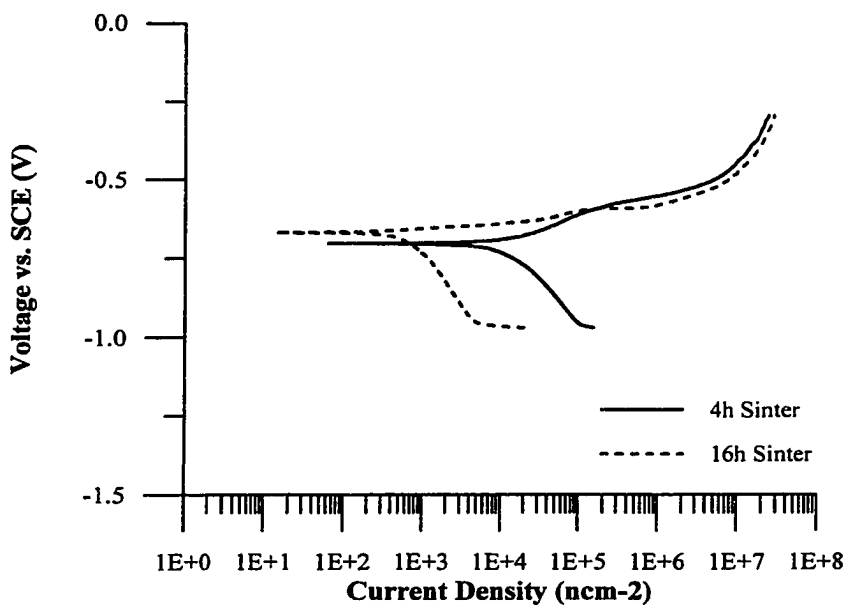
Figure 4.53 Polarization curves for samples of P/M 2014 microalloyed with Ag when sintered for 4 and 16h.

4.8.3 Sn Modified 2014

Polarization resistance curves measured for Sn modified samples sintered for times of 0.5, 1 and 2h are shown in Figure 4.54; the principal values of interest are summarized in Table 4.12. Although the variation in corrosion rate was minor relative to P/M standards, variations in corrosion potential were significant. In all three cases, a shift to more negative values (relative to P/M standards) resulted; these became most prominent in samples sintered for 0.5h.
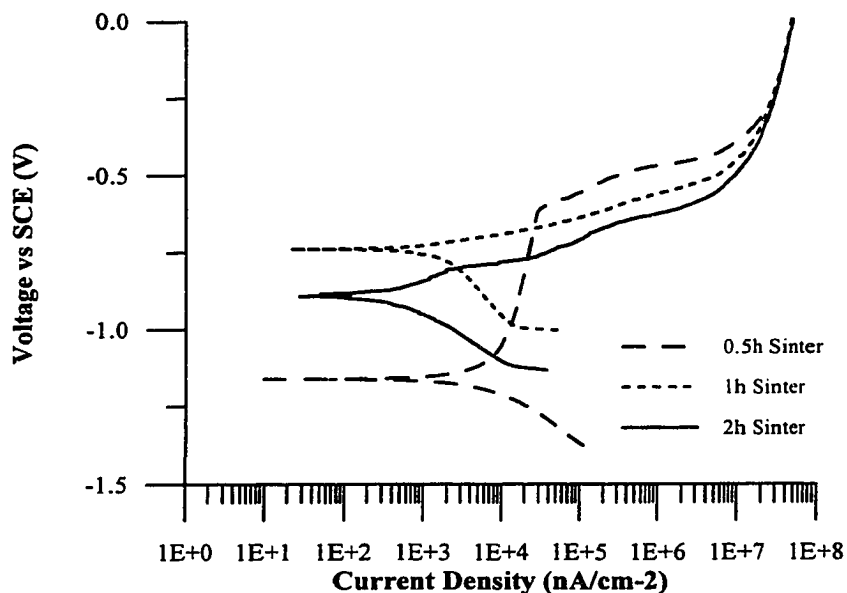
Figure 4.54 Polarization curves for samples of 2014 microalloyed with Sn when sintered for 0.5, 1, and 2h.

Table 4.12 Summary of corrosion data measured from polarization curves.

Specimen Type	Sintering Time (h)	Corrosion Potential (V)	Corrosion Current Density (nA/cm^2)	Corrosion Rate (mm/y)
P/M 2014 Std.	0.5	-0.69	1.5×10^2	1.6×10^{-3}
P/M 2014 Std.	1	-0.66	1.3×10^3	13.2×10^{-3}
P/M 2014 Std.	2	-0.65	1.7×10^2	1.8×10^{-3}
Wrought 2014	N/A	-0.68	2.8×10^3	29.4×10^{-3}
Ag Modified 2014	4	-0.71	1.03×10^4	117×10^{-3}
Ag Modified 2014	16	-0.67	1.7×10^2	1.8×10^{-3}
Sn Modified 2014	0.5	-1.14	1.3×10^3	13.9×10^{-3}
Sn Modified 2014	1	-0.74	1.1×10^3	11.4×10^{-3}
Sn Modified 2014	2	-0.87	1.1×10^3	11.4×10^{-3}

5   DISCUSSION

A method of microalloying Al-based P/M alloys in-situ during liquid phase sintering has been developed. In many investigations of alloying effects, studies are typically initiated with relatively simple alloy systems. By using such alloys, the complexities of the additional elements found in commercial alloys are avoided and laboratory studies tend to clearly reveal the influence of alloying on bulk material properties. Frequently, these results are then used as a guide to subsequent studies of more complex commercial alloys. Following this concept, two Al-based alloys were considered as a basis for all experiments in this work; ternary Al-4Cu-0.5Mg alloy and commercial grade 2014. Although both alloys are similar in composition, the complexities associated with Si, Mn and impurity elements are avoided in the ternary. The following sections discuss the experimental results relevant to processing and the characterization of products produced by standard P/M practices and "core/shell" processing.

5.1   PROCESSING

Prior to actual processing experiments, several possible microalloying additions were initially evaluated from a theoretical perspective. As a basis for this evaluation, chemical thermodynamics, diffusion rates and mass balance modeling were considered. In the case of thermodynamics, it was found that all candidates had a tendency to dissociate during sintering, some more so than others. The most prominent in this regard was $AgNO_3$. In an effort to assess the validity of these predictions, actual alloy/mineral (compound) mixtures were sintered and examined. With respect to the extent of dissociation, results showed $AgNO_3$ to be complete, SnO_2 close to completion, yet spodumene was seemingly unaffected. Whereas the trend of increasing dissociation tendency from SnO_2 to $AgNO_3$ was thermodynamically predicted, the inert nature of spodumene was not. Furthermore, if spodumene had reacted the most likely reaction product to form thermodynamically, should have been $LiAlO_2$. Since Li is a principal element of this thermally stable oxide, a minimal amount is thus available for diffusion.

Overall, these difficulties with spodumene resulted in an inability to microalloy the central core with Li. This illustrates that in order to correctly predict the reactions that occur in any system, one must address reactant products and kinetics as well as thermodynamics.

As the desired alloying addition was made via diffusion, the diffusion rates of candidate elements in Al were considered. For the three elements of principal interest, decreasing diffusion rates in solid Al from Sn to Ag to Li were anticipated. Intuitively one might expect the same order of decreasing alloying element concentrations in central alloy cores for any given sintering time. Although this appeared valid with regard to Li, the opposite was discovered for Sn and Ag. It is believed that the discrepancy with Sn and Ag was probably the result of variations in the extent of dissociation. As revealed in XRD scans of the shell component, the reduction of $AgNO_3$ was complete, that of SnO_2 was partially complete and that of spodumene was negligible. Since $AgNO_3$ experienced the greatest degree of dissociation/reduction, Ag ions should be most readily available for inward diffusion. Likewise, the diffusion of Sn and Li ions is restricted because of an incomplete reduction in the respective starting compounds. Furthermore, since SLPS was utilized, the liquid component offered a preferential path of high diffusivity for any element introduced into the core. Consequently, the higher diffusion rates experienced by one element over another in solid Al are minimized. Thus, as Ag, Sn, and Li were expected to have similar diffusion rates through the liquid phase, the larger differences between solid diffusivities were not fully reflected in the final concentrations reached whereas the extent of dissociation was.

To quantify the extent of microalloying with Ag and Sn, low magnification EDS analyses of core regions were completed (Figure 4.10). Assays indicated that the amount of diffusing species introduced varied with sintering time. Evidently, both micro and macro scale alloying could be achieved, provided an appropriate sintering time was selected. Although the change in concentration was relatively steep for short sintering

times, a plateauing trend developed as sintering continued. Assuming ideal solutions, the activity of a species is equivalent to its mole fraction. Consequently, the observed trend suggests an approach towards equilibrium. Comparing calculated results to the concentrations measured in samples sintered for 16h indicated a reasonable correlation. For example, calculated concentrations of Ag and Sn were 2.9, and 1.8 wt % respectively, whereas measurements indicated 2.8 and 1.4 wt % respectively. Thus, despite the simplicity of this approach, a reasonable estimation of the final concentration was possible.

To confirm the quantitative nature of EDS analyses, P/M 2014 alloy standards were also analyzed. Using this technique, no measurable concentration of Sn was found, whereas the Ag concentration was repeatedly analyzed to be 0.4 wt%. However, commercial specifications for 2014 state that the concentrations of Sn and Ag should be negligible. Through wet chemical analysis conducted in-house and a review of the alloy chemistry reported by Valimet, the concentrations of Sn and Ag were confirmed to be negligible. It is believed that the EDS detection of Ag simply arises because of an overlapping of peaks for Ag K_α and an Al (K_α+K_β) sum peaks (2.984 and 2.986 keV respectively). Although the latter peak was generated from Al only, it is assumed by the computer program to be one produced from Ag, and quantified as such. Thus, EDS proved to be an accurate means of assessing the concentration of Sn, yet overestimated that of Ag by approximately 0.4 wt%. Despite this, the concentration predicted by mass balance modeling remained reasonably effective.

Although the bulk assay of core regions was determined using low magnification EDS, higher magnification scans were also conducted to determine the location of the diffused species within the microstructure. Results indicated that Sn was concentrated in the intergranular regions with a negligible concentration within the alloy grains. A different distribution was noted for Ag-bearing samples wherein a reasonably uniform concentration existed throughout the microstructure. The differing distributions are

believed to be the result of solubility limits. At the sintering temperatures of interest, the approximate solid solubilities of Sn and Ag in Al are 0.1 wt% and 22 wt%, respectively. Furthermore, using isothermal tie lines on binary phase diagrams it is predicted that a liquid phase should exist in equilibrium with such saturated solids and have Sn and Ag concentrations of 52 wt% and 47 wt% respectively. Consequently, as Sn is introduced into the central core, an appreciable concentration can only be developed in the liquid portion of the sintering system. During furnace cooling, this liquid solidifies and forms the component of the microstructure denoted as the intergranular regions. However, since the solid solubility limit of Ag is relatively high in both the solid and liquid phases present during sintering, Ag readily accumulates in each. Thus, a more uniform distribution results.

Because of the nature of P/M, the presence of porosity at all stages was a common occurrence. To quantify the degree of porosity in the samples produced in this work, density measurements were carried out using mercury densitometry. Although this technique could not address the nature of the porosity (interconnected or closed isolated pores), measured values were believed to be reasonable. Results indicated that alloy standards as well as the products of "core/shell" processing densified appreciably during sintering, reaching sintered densities of approximately 92% of theoretical. After final swaging practices, all sample densities were found approach theoretical values. Thus, the presence of the outer shell had no deleterious effects on densification. Although a value for the density of 2014 was found, a value for the ternary alloy was not. As an estimate for the ternary alloy, the specific gravity of 2014 was used. Despite the similarities in alloy chemistry, 2014 is alloyed more extensively with relatively heavy elements such as Cu and Mn. Thus, the usage of this value provides a reasonable yet conservative estimate.

5.2 AGE HARDENING/TENSILE PROPERTIES

Since the Al alloys used are heat treatable, the influence of microalloying additions on age hardening and tensile strength was assessed. Initially, the hardening response of samples based on the ternary alloy was evaluated. To determine if any hardness improvement resulted from Ag additions, age hardening experiments at 433K were performed. When comparing the hardening response of standards versus that of Ag modified samples, it was noted that for both, peak hardness (T6 treatment) was achieved after aging for ~18h. However, the value found for Ag modified samples was consistently higher, regardless of sintering time. The observed improvement of 25-30 points is in agreement with similar studies utilizing I/M techniques [150]. Results of tensile tests on samples in the T6 condition correlated well with the hardness data, revealing significant improvements. Most notable was the improvement of some 60MPa in yield strength. Furthermore, UTS was improved by approximately 20MPa with only a minor concomitant reduction in elongation. Consequently, the general mode of fracture was preserved, with all samples failing in a ductile manner. Thus, an amount of Ag, sufficient to enhance hardness, was introduced during each of the sintering times considered (2 and 4h). Furthermore, the introduction of Ag via "core/shell" appears to behave in the same manner as that introduced by standard I/M techniques.

To extend this study to a commercial level, age hardening curves were measured for standard and microalloyed versions of P/M 2014. Aging curves were generated for samples of P/M 2014 sintered for 0.5, 2 and 16h. Although the hardening response was similar in samples sintered for the shorter periods, increasing this time to 16h promoted a distinct reduction in hardness. This trend was also preserved in the results of tensile tests. This is believed to result from increased microstructural coarsening and segregation that is known to occur. Heat treatment practices cited for peak hardness in wrought 2014 were also found to yield peak hardness in P/M 2014. However, the maximum hardness and tensile strengths attained were greater in certain P/M products than that cited for a wrought counterpart. This implies that for alloy 2014, P/M processing can yield a

product of increased mechanical integrity, yet the attainment of this improvement requires no special heat treatment considerations.

The hardness improvements noted for the ternary alloy system were not manifested in samples of P/M 2014 microalloyed with Ag. For sintering times of 2 and 4h, no significant improvement in hardness or tensile properties was observed. This trend was also noted in similar studies that employed I/M practices, when no discernable hardness improvement was attained with the addition of 0.5 wt% Ag to 2014 [11]. However, when the sintering was prolonged to 16h, a minor yet consistent improvement was noted. It is believed that this resulted from the chemistries of grains and intergranular regions changing with sintering time [58]. As sintering progressed, an increased segregation of alloying elements to the liquid phase resulted. Whereas Ag is known to impart a hardness improvement to many Al alloys, difficulties are commonly encountered in alloys that contain Si [151]. EDS analysis indicated a negligible concentration of Si in alloy grains after sintering for 16h. Although such analyses were conducted on as-sintered microstructures, it is believed that Si partitioning was preserved reasonably well in the final heat-treated samples. Thus, it can be postulated that in samples sintered for 16h the chemistry of alloy grains has approached that required for hardness improvement by Ag. Unfortunately, this improvement was not quantified in terms of tensile strength. However, since a strong correlation between hardness and tensile strengths exists in all previous data, it seems reasonable to assume that this trend would continue in this instance as well.

For all samples of P/M 2014 microalloyed with Sn, a steady reduction in peak hardness with increased sintering time resulted. Due to processing difficulties, this reduction was only quantified in terms of tensile properties for a select few samples. However, in such tests tensile and yield strengths were found to also diminish with increased sintering time. This reduction is believed to be the result of microstructural coarsening and exceeding the solid solubility limit of Sn. Despite the introduction of Sn

during sintering, it seems reasonable to assume that the microstructure of Sn modified samples would coarsen at a rate similar to that of P/M 2014 standards. Thus for any given sintering time, the reduction of hardness through this action should also be comparable. As previously shown in Figure 4.16, the reduction in hardness that was achieved in alloy standards sintered for 16h was reached after only 8h in Sn modified samples. This implies that aside from microstructural coarsening, a secondary factor must also exist. Chemical analyses of Sn modified samples indicated that in most instances the amount of Sn introduced was in excess of its solid solubility limit in Al. Since Sn is inert with respect to Al, its accumulation in the intergranular regions is most likely that of discrete Sn globules. Thus, a composite of sorts is created with the P/M 2014 as the matrix component and the soft malleable Sn as a secondary phase. Therefore, hardness is a combination of both constituents and overall, a softer, weaker alloy results.

In microalloying experiments involving spodumene, it was postulated that a negligible amount of Li was introduced. However, the detection of Li is difficult using conventional means. Thus, age hardening experiments were conducted on several samples that potentially contained Li. Despite variations in aging temperature, no consistent difference in hardness relative to P/M 2014 standards was observed. In I/M practices, additions of Li as low as 0.13 wt% to similar alloy systems are known to impart a hardness improvement [20]. Thus, it seems reasonable to conclude that even if Li is present, its concentration is very low. However, it is worthy to note that the incorporation of Li using I/M practices is also difficult.

5.3 TRANSMISSION ELECTRON MICROSCOPY

In order to determine if microalloying additions had any significant influence on the precipitates formed during aging, TEM studies of several samples were conducted. As described earlier, I/M microalloying of similar alloys with Ag can result in a transformation of the dominant precipitate from θ-type to Ω. Due to the differing habit

planes of θ ({100}) and Ω ({111}), distinction between them using a TEM can potentially be as easy as viewing the alloy specimen along a suitable zone axes. Perhaps the most useful axis in this regard is the <011>-type, since information on both the {100} and {111}-type of planes is gathered simultaneously. Thus, for any BFI recorded in this orientation, one can superimpose both types of planes and potentially determine which precipitates are θ' and which are Ω. Another useful zone axis in the study of θ-type precipitates is the <100>-type. Here, certain {100} crystal planes can be viewed edge-on and normal to the axis concurrently. In this fashion, strong evidence supporting the presence/absence of the plate-like θ' precipitates can be obtained.

The first samples to be analyzed with the TEM were ternary alloy standards. From the <100> BFI given in Figure 4.22, it is evident that precipitates of uniform thickness lie on variants of {100} planes. It is believed that these precipitates are actually plate-like precipitates of θ' viewed in an edge-on manner. Further evidence of θ' was seen as streaking in the corresponding DP. In this pattern, streaking extended in <100> directions and formed faint crosses at the center of each quadrant of four bright matrix spots. Such streaking clearly implied the presence of θ' precipitates since the similarity between the photographed DP and that calculated for θ' (Figure 1.23) was evident. Since EDS analysis of the same region indicated an absence of Ag, these precipitates can not be Ω. Further evidence pertaining to an absence of Ω precipitates was discovered in <110> and <111> DPs (Figure 4.23). In these patterns, an absence of streaking in <111> directions and spots characteristic of Ω was noted whereas streaking in <100> directions characteristic of θ' was present.

In accordance with Figure 1.10, the chemistry of the ternary alloy implied the possible existence of S-type precipitates. However, since streaking in <100> DPs was more representative of θ' and the amount of Mg available for S-type (Al$_2$CuMg) precipitation is low, it was believed that a negligible amount of S-type precipitates are

present. Overall, the data from BFIs, DPs and EDS analysis imply that θ' is the dominant precipitate. This dominance was preserved through all sintering times considered.

Relative to ternary alloy standards, samples microalloyed with Ag (4h sinter) exhibited significant differences in precipitates. When orienting the sample into a <110> zone axis, the resulting DP exhibited intense streaking along <111> directions with little along a <100> direction (Figure 4.25). By superimposing {111} and {100} planes on the corresponding BFI it is clear that the majority of precipitates lie on the former planes, with few observed on {100} planes. Although such data suggest that both θ' and Ω-type precipitates exist, Ω is clearly dominant. Further evidence of Ω precipitation was exhibited in DPs recorded along <111> and <100> zone axes. When the <111> diffraction pattern generated from this sample (Figure 4.26) was compared to a recently published computer generated pattern for Ω (Figure 1.23) [142] a strong match was revealed. Finally, using a <100> zone axis, the resulting DP (Figure 4.26) also indicated the presence of Ω through the small square arrangement of spots within the larger square of bright spots produced from the Al matrix. Also of interest was the recurrence of features found in similar patterns taken from the sample free of Ag (streaking in <100> directions together with faint crosses at the centre of each square of matrix spots). Again, these factors present strong evidence for the existence of both θ' and Ω-type precipitates.

To confirm the presence of Ag as required for the formation of Ω precipitates, the chemistry of the region discussed above was analyzed using EDS. In the resulting spectrum (Figure 4.25) the presence of Ag was verified. In similar analyses using an SEM difficulties were encountered in that an overlap between the L_α peak for Ag and the $(K_\alpha + K_\beta)$ sum peak for Al overlapped. Although additional peaks characteristic for Ag only exist at higher voltages, the operating voltage of the SEM (25kV) did not allow appreciable excitation. However, the significantly higher operating voltage of the TEM (200 kV) did permit such excitation. Consequently, the peaks observed in the EDS

spectrum at 22.16 (K_α) and 25.52 keV (K_{edge}) of Figure 4.25 were found to be characteristic of Ag and thus verified its presence.

Additional studies of the precipitates in ternary samples modified with Ag were conducted under dark field conditions. Under such conditions, interference associated with the strain fields of precipitates was avoided. Furthermore, by forming the dark field image by selected spots or streaks in the DP, one can isolate the different variants of a given precipitate. To complete this analysis, the sample was tilted into a <110> orientation, and a BFI and corresponding DP were first recorded (Figure 4.27). Centered dark field images (CDFIs) were then formed with the portion of the diffracted beam responsible for the streaks denoted as (a) and (b) in the DP. Evidently, each streak was associated with a different variant of Ω precipitates lying on a particular member of the {111} matrix planes. Aside from streaking, an array of two uniformly spaced diffraction spots was also present. Since such spots extend in a <200> direction they were most likely produced from the precipitates that were found to lie on {100} planes. Unfortunately, CDFIs generated from these faint spots were likewise very faint with no discernable details.

Through the culmination of BFIs, DPs, EDS analysis and CDFIs it is clear that Ω and θ' precipitates exist in the ternary samples modified with Ag. However, it is also clear that those of the Ω-type are dominant. These observations were confirmed for both sintering times considered (2h and 4h). Thus, it can be concluded that an amount of Ag sufficient to promote the formation of Ω was introduced in times as short as 2h.

For P/M 2014 standards, sintering times of 2, 4, and 16h were considered. When examined in a <100> orientation, precipitates of uniform thickness that lay parallel to {100} planes were found. This morphology was postulated to be plate-like precipitates viewed edge-on and was confirmed by those lying normal to the incident beam. A BFI

illustrating an example of this analysis was given in Figure 4.28. By compiling the evidence of a plate-like morphology and {100} habit plane together with characteristic streaking in <100> and <110> directions, it appeared that the dominant precipitate was again θ′ (CuAl₂). Since the chemistries of the ternary alloy and P/M 2014 were similar, the existence of θ′ as the dominant precipitate was not surprising.

In the analysis of Ag modified samples of P/M 2014, those sintered for 2, 4, and 16h were considered. For the shorter sintering times, analyses in a <100> orientation indicated that the dominant precipitate did not differ from that found in alloy standards and remained as θ′ (Figure 4.30). Additional examinations in <110> and <111> orientations also implied a dominance of θ′ through the characteristic streaking discussed earlier. For samples sintered 16h, this trend was again apparent in a <100> orientation (Figure 4.31). However, when viewed along <110> and <111> zone axes, evidence suggested that precipitates other than θ′ existed. Morphologically, the presence of irregular, hexagonal precipitates were noted (Figure 4.34) when the sample was in a <111> orientation. Furthermore, in the <110> DP of Figure 4.33 faint streaking was observed in <111> directions, thus implying the presence of precipitates on {111} planes. Since the morphology and habit plane were characteristic of Ω it was postulated that precipitates of this nature exist in this sample. However, it is also believed that θ′ is still dominant.

As mentioned earlier, increased sintering time promoted microstructural segregation. Thus, the most extensive segregation occured in the samples sintered for the longest period of time (16h). Through this action, it is believed that the chemistry of alloy grains eventually approached one that is suitable for Ω precipitation. Consequently, appreciable Ω precipitation was not achieved in samples sintered for the shorter periods, but did occur in the longest time investigated.

Through TEM analyses, it can be concluded that θ' precipitates are dominant in ternary alloy standards, P/M 2014 standards, and P/M 2014 samples modified with Ag. However, Ω precipitates dominated in ternary samples modified with Ag and also existed in P/M 2014 samples microalloyed with Ag through a sintering time of 16h. In samples found to contain Ω, considerable improvement in hardness, yield strength and UTS were consistently observed. Whereas Ω and θ' are believed to be similar in chemistry and crystalline structure, it is quite possibly their difference in habit plane that promoted the noted strength improvements. Aluminum, being a face centered cubic material, is known to deform by slip along close packed, {111} planes [23]. Since Ω forms on this same family of planes, it would offer a more direct obstacle for dislocation motion than θ', thus resulting in the observed improvements in mechanical properties.

5.4   WEAR

To assess the influence of Sn and Ag additions on the wear resistance of P/M 2014, dry sliding wear tests were conducted. Additional tests were also conducted on a wrought version of 2014 to assess the influence of processing. Initially, testing focused on 2014 P/M standard samples, addressing the influence of sintering time on wear behaviour. Results indicated a decrease in wear resistance with increasing sintering time. Although powder metallurgy products are typically credited with having a fine microstructure, coarsening can result from prolonged liquid phase sintering. As this phenomenon has been observed in many instances [58, 118], and is known to have a negative effect on wear resistance [152], the observed decrease in wear resistance was to be expected.

Comparison of results for P/M alloy standards with those for a wrought product suggested that the latter was superior. Although microstructural coarsening in P/M samples promotes a decrease in wear resistance, the content of hard, fine, aluminum oxide particles produced through atomization of alloy powder was expected to enhance

the wear resistance. Evidently, the competition between these two factors was dominated by microstructural coarsening.

In the testing of P/M samples microalloyed with either Sn or Ag, a trend of improved wear resistance with sintering time was noted. This occurred primarily for the Sn modified samples, and to a lesser extent, for Ag modified samples. As both sample types undergo microstructural coarsening, this negative effect has been counteracted by the microalloying addition. Thus, as the sintering time was extended, not only did the microstructure coarsen, but also an increasing amount of the microalloying species diffused inward. This resulted in an overall improvement in wear resistance, the reasoning for which was different for each element.

For Sn, the discrete regions of this element within the microstructure were expected to melt and spread across the wear surface, thus reducing direct metal to metal contact [89]. Although no direct evidence of this behaviour was discovered through X-ray mapping, the occurrence of such a phenomenon might be difficult to detect simply because of the limited amount of Sn added.

When considering the effects of alloying on wear resistance, researchers often acknowledge changes in stacking fault energy (SFE) as a contributing factor [153]. That is, a more wear resistant alloy develops as the SFE decreases. Since Ag is known to decrease the SFE of Al, the small improvements that were noted for Ag microalloyed samples might therefore be a consequence of this behaviour.

Regardless of the sample type considered, all weight loss vs. applied load data were reasonably linear in nature, and displayed a low slope. Typical data for other aluminum-base alloys are of the same nature, with an abrupt increase in slope corresponding to a transition from mild to severe wear [83]. As this transition has not been observed, all tests have been carried out in the mild wear regime. Furthermore, as

samples exhibited very similar behaviour with respect to wear track and debris morphologies/chemistries, it is therefore possible that the same wear mechanism(s) was also involved.

From a morphological standpoint, wear debris was primarily powdery at lighter loads, becoming increasingly more plate-like as the applied load was raised. As these plates were consistently more dilute in iron content than the loose powder, and exhibited a fine microstructure, it seems that their formation results from the compaction of powder particles together with portions of the Al-alloy test block. When using lighter loads, the force necessary for compaction was apparently not realized, thus the debris remained as loose powder.

Regarding identification of the phases present in wear debris, an obvious consistency between all X-ray spectra gathered was the broad nature of the Fe(110)/Al(200) peak. As previously mentioned EDS analysis revealed the debris to be principally comprised of aluminum, iron, and oxygen. Hence, any phase(s) responsible for the noted broadening should be chiefly comprised the aforementioned elements. Considering oxide formation first, Al_2O_3 and FeO both have their main peak slightly below metallic iron, possibly contributing to the observed broadening. Such oxides most likely form through the continuous exposure of fresh metal to air as wear proceeds. Alternatively, intermetallic phases may also exist, formed through high strain rates akin to mechanical alloying. The strong correlation between the width of the broad peak and that of the cluster of peaks known to exist for phases such as $Al_{13}Fe_4$ and $FeAl_2$ also supports this hypothesis. Finally, broadening may be simply due to the nature of the debris. As the debris was of a sub-micron morphology, it is also anticipated to be in a state of high residual stress. Both factors may contribute to peak broadening [154,155]. Thus, due to the complexity of the debris, no one phase can be said to exist exclusively, the most likely scenario being the co-existence of many phases.

5.5   CORROSION

In attempts to determine the influence of microalloying on corrosion resistance, polarization resistance curves were produced for P/M 2014 standards as well as those modified with Sn and Ag. Such tests allow for the determination of the corrosion potential, the corrosion current (through Tafel lines), and in turn the rate of corrosion. The larger the corrosion current, the larger the corrosion rate.

Corrosion studies of P/M 2014 standards indicated that differences in sintering time from 0.5 to 2h had a minor influence on the corrosion rate. When these results were compared to those acquired for a wrought version of 2014, the improved resistance of the P/M product was clear. Relative to wrought counterparts, P/M products made from Al alloys are typically accredited with having equivalent or superior resistance [156]. Thus, the aforementioned results seem reasonable and highlight an additional benefit of P/M.

Corrosion studies of Ag modified P/M 2014 were conducted on samples sintered for 4h and 16h. Results proved quite erratic in that the 4h sample exhibited the highest corrosion rate of all samples tested, whereas that sintered for 16h corroded at a rate that was very similar to that measured for P/M alloy standards. In efforts to improve the corrosion resistance of many metals, noble metal alloying is one possibility [78]. By alloying with elements such as Pt, Au and Ag, improved corrosion resistance can result. However, one notable exception is the addition of Ag to Al whereby little improvement results. Consequently, although the corrosions rates measured for Ag modified samples are erratic, they are representative of the fact that the corrosion resistance of Al is not enhanced by Ag additions. In fact, it appears that the most plausible result is an acceleration of the corrosion rate.

The corrosion resistance for Sn-bearing samples of P/M 2014 was also assessed. Overall, samples microalloyed with Sn exhibited a reduction in corrosion potential yet corroded at a rate similar to that of P/M alloy standards. Although the polarization

response of samples sintered for 1h and 2h was similar, that for the 0.5h samples was different. In such samples, the corrosion potential was reduced considerably. Furthermore, the anodic portion of the curve exhibited an obvious vertical climb followed by a portion that was essentially the same as the other samples tested. This behaviour was repeated for four additional samples and implied that pitting had occurred. Because of the short sintering time used results have shown that the concentration of Sn would be low. Thus, it seems that the observed behaviour is most likely attributable to other factors. In corrosion studies of P/M components, results frequently differ from author to author for any given alloy system [157]. Since the extent and distribution of porosity in P/M products can vary widely depending on the processing route followed, discrepancies are frequently attributed to this factor. Several of the Sn modified samples used in corrosion tests were polished and examined. Although density measurements suggest that the amount of porosity is similar in each case, the distribution was not. Whereas the 0.5h samples exhibited an abundance of fine pores, larger but fewer pores were noted in the 1h and 2h samples. This represents the natural progression of sintering with time with the shorter time insufficient for the development of large, closed and isolated pores. Since it is believed that pitting initiates at pores, the finer distribution of small pores provided a large number of nucleation sites and the observed pitting behaviour resulted.

In attempts to verify the influence of porosity, several samples that were hot swaged to a smaller diameter (higher density) were tested. Unfortunately, difficulties were encountered with the smaller holder used and the data from these tests was deemed unreliable.

As a potential alternative to I/M techniques, "core/shell" processing possesses several advantages. First is the ability to alloy selected sections within a single component. Typically, alloying additions are beneficial in some regards (i.e. strength, wear resistance), yet deleterious in others (i.e. corrosion resistance). Thus, using the means of alloying developed, only those areas that require improvement need be treated,

whereas the bulk of a part is not rendered susceptible to any of the negative influence(s). Since the process is diffusion-based, time and diffusion distance are key process parameters in the determination of the extent of microalloying; this may range from a narrow surface layer to the microalloying of a complete cross section. When used as a surface treatment process, the need for additional equipment and post processing steps common to methods such as pack cementation could be avoided. Finally, due to the highly reactive nature of Al, alloying with many elements additional to those reported here is potentially feasible, and recent studies suggest that several elements may actually be incorporated simultaneously.

Although the ternary alloy and P/M 2014 were the alloys of interest in this report, it is believed that the process may be applied to many additional aluminum-based alloys. In principle, any aluminum alloy that exhibits a substantial mushy zone (solid plus liquid regime) should be amenable to SLPS. The network of liquid that is formed then provides a path for rapid diffusion and thus allows (micro)alloying addition(s) to be introduced in a reasonable period of time. Through the adaptability and versatility associated with "core/shell" processing, the technique might offer an attractive alternative to I/M in certain instances.

6 SUMMARY

In many high strength steels, microalloying with elements such as V and Nb is instrumental in the strength levels achieved. For this reason, numerous researchers have focused on applying the same concepts to Al-based alloys. Experimenting with elements such as Ag, Sn, Li, Na, P, Zr and Ti, several principal effects of microalloying were established.

For Al alloys used in structural applications, high strength is principally attained through precipitation hardening. Consequently, most microalloying studies have focused on this aspect. In this regard, several of the most promising elements are Ag, Sn and Li. When adding small quantities of Ag (<0.5 wt%) to Al-Cu-Mg alloys, excellent improvements in mechanical properties (hardness, yield and tensile strengths) can result. Although the base alloys are strengthened by common precipitates of the θ and S-types, Ag addition promotes the formation of new precipitates referred to as Ω. Similarly, trace additions of Li can promote an increased presence of δ and T-type precipitates at the expense of a reduction in those traditionally found. Micro additions of Sn (<0.05 wt%) have also shown a positive influence on mechanical properties, although this has been limited to Al-Cu binary alloys. Unlike Ag and Li, Sn simply promotes a finer distribution of precipitates rather than the formation of precipitates that are not normally found in the base alloy.

Additional effects of microalloying include an alteration of recrystallization behaviour through Zr and Ti additions and the morphology of secondary phases in the presence of Ca, Na, or P. Despite the substantial effort directed towards Al microalloying, any influence from the means of alloying is seldomly addressed. For this reason, an alternative approach to the traditional means of microalloying (ingot metallurgy) was developed.

Termed "core/shell" processing, the technique is a powder metallurgy approach that incorporates reaction sintering and diffusion in response to an activity gradient. The process begins with ball milling wherein base alloy powder and a mineralogical/synthetic compound are mixed. Raw alloy powder is then pressed into a coherent green body. Space between this porous component and the mold walls is then filled with the milled mixture. After re-pressing, a composite green body comprised of a central alloy core surrounded by a thin outer shell results. Such composites are then heated in an inert atmosphere to a semi-solid condition. As liquid phase sintering progresses, the central core densifies and the trace element compound is reduced in the outer shell. In response to the chemical potential gradient that exists between the shell and core, a net flux of the reduced element results. Once furnace cooled, the porous shell is readily chipped free of the dense, microalloyed core.

To study the influence of microalloying additions using the technique developed, two Al-based alloys were considered; ternary Al-4Cu-0.5Mg alloy and AA2014 as a complex commercial equivalent. Each selected for its industrial importance, common usage, and extended semi-solid regime. Liquid phase sintering experiments were initiated with these alloys and it was discovered that each responded well to sintering and reached a final density of some 92% of theoretical. Appropriate sintering temperatures for the ternary and commercial alloys were found to be 903K and 873K respectively. Once sintered, samples were hot swaged to essentially full density.

With a literature review of microalloying completed, a list of elements that could be of benefit to the selected base alloys was established. Prior to actual experimentation, appropriate mineralogical or synthetic compounds for these elements were determined. Theoretical studies of thermodynamics, diffusion rates and mass balances were then completed at the sintering temperatures of interest. From these preliminary results, it was postulated that the most feasible elements were Li, Sn and Ag.

Microalloying experiments began by preparing milled mixtures of alloy powder together with spodumene ($LiAlSi2O_6$), tin oxide (SnO_2) or silver nitrate ($AgNO_3$). Numerous "core/shell" composite green bodies were then pressed and sintered for various lengths of time. To ascertain the success/failure of microalloying, sintered samples were examined using SEM/EDS (point and bulk area scans), XRD and wet chemical analysis. Results of these analyses indicated that Sn and Ag were readily incorporated into the central core, whereas an appreciable concentration of Li was not. It was postulated that the difficulty with Li arose from an incomplete reduction of spodumene and/or its transformation into $LiAlO_2$. The apparent stability of these oxides thus prevented the inward diffusion of Li.

For Sn and Ag, the maximum concentrations noted in the central core were achieved after sintering for 16h (approximately 2 and 3 wt% respectively). Due to an approach towards equilibrium, mass balance calculations provided reasonable estimates of these concentrations. Since concentrations on the microalloying scale (<0.1 at%) were achieved with shorter sintering times, the alloying technique was successful on both a micro and macroalloying scale. Point analyses of sintered microstructures indicated that Sn was concentrated in the intergranular (once liquid) regions, whereas Ag was more evenly distributed throughout. This behaviour was a result of the solid solubility that is extensive for Ag in Al, yet negligble for Sn in Al.

With the success of Sn and Ag clearly established, additional samples were then processed and swaged. For the sake of completeness, samples potentially microalloyed with Li were also swaged. Hot swaging proved to be an acceptable means of achieving near full density is all samples except those containing a considerable concentration of Sn. Since the temperature used for hot swaging was greater than the melting point of Sn, localized melting of the intergranular regions resulted. Consequently, hot shortness was

problematic and excessive cracking/fracture resulted. To circumvent this difficulty, a cold swage/anneal practice was adopted for samples to be used in wear and corrosion testing.

To characterize the mechanical properties of microalloyed samples as well as alloy standards, aging response, tensile testing, transmission electron microscopy (TEM), and wear were considered. For ternary and P/M 2014 standards, the same heat treatment (T6) as specified for wrought 2014 was found to yield peak hardness. However, a reduction in peak hardness occurred as sintering time was prolonged. This decrease was attributed to microstructural coarsening and increased segregation. Tensile test results agreed well with hardness values since the highest strengths were measured for samples sintered for the shortest periods of time. Regardless of sintering time, TEM studies indicated that both alloys were strengthened by a fine distribution of θ' ($CuAl_2$) when aged to the T6 condition.

For ternary alloy samples microalloyed with Ag, a considerable improvement in peak aged hardness and tensile strength was consistently observed. TEM analyses of such Ag-bearing samples in the T6 condition indicated a dominance of Ω precipitates with a lesser amount of θ'. Evidently, Ag additions promoted a preferential precipitation of Ω. Since Al deforms by slip along the close-packed {111} planes, the Ω precipitates that also form on these planes offered an increased resistance to dislocation motion as compared to θ' which forms on {100} planes. Consequently, the noted improvements in strength resulted.

Despite the improvements noted for the ternary alloy, when samples based on P/M 2014 were microalloyed with Ag, hardness and tensile improvements were relatively minor and only became discernable in samples sintered for 16h. Although all sintering times generated a considerable Ag concentration within the core, θ' precipitates remained dominant although presence of Ω precipitates was discernable in samples sintered for

16h. It was postulated that the increased segregation with sintering time eventually yielded alloy grains of a suitable composition that could promote Ω precipitation. When P/M 2014 was microalloyed with Sn, a trend of reduced peak hardness and tensile strength with sintering time, and in turn, Sn content was observed. Although a similar reduction was noted for alloy standards, the extent was substantially greater in Sn-bearing samples. Since Sn appeared to be inert with respect to the other elements present, concentration of this soft, malleable metal in the intergranular regions resulted in an overall reduction of strength.

To quantify the wear resistance of microalloyed samples, P/M 2014 standards and a wrought version of 2014 were subjected to dry sliding wear tests. It was concluded that all tests were run in the mild wear regime, with Sn modified samples offering the greatest resistance to wear. P/M 2014 standards became less resistant to wear as sintering time was prolonged and the microstructure coarsened. Despite the occurrence of similar coarsening in Sn-bearing samples, an improved resistance to wear was noted. Apparently, the benefits of an increased concentration of Sn outweighed the negative influence of microstructural coarsening. It was postulated that the regions of locally high Sn concentration would melt during the tests thereby reducing the coefficient of friction and consequently, wear rate. Although the analysis of wear debris indicated an elevated concentration of Fe, the existence of a single Fe-bearing phase could not be concluded. It was postulated that the debris was actually comprised of a mixture of intermetallic and oxide-type phases.

To quantify the corrosion resistance of samples based on P/M 2014 polarization resistance curves were measured. Relative to a wrought counterpart, P/M standard samples behaved in a similar manner yet exhibited an improved resistance to corrosion. Although the corrosion resistance of most microalloyed samples was also improved over the wrought product, rate of attack was raised with additions of Sn and Ag.

Appreciable success was achieved with the microalloying technique developed. The results have shown that the technique is viable for macro and microalloying certain Al-based alloys with Sn or Ag. Benefits of the procedure include the flexibility associated with a powder metallurgy processing and the potential to alloy entire or selected areas of P/M components. Since there appears to be no compromise of final mechanical properties relative to ingot metallurgy, the concept of "core/shell" processing may well be a feasible industrial alternative for the elements used in this work as well as many others.

7 CONCLUSIONS

Through completion of the research contained within this thesis, several conclusions can be drawn:

1. A novel technique for alloying P/M components ("core/shell" processing) was successfully developed.

2. The technique developed is an attractive alternative, both to traditional P/M microalloying processes and in some instances to I/M practices, for potentially enhancing mechanical properties of Al alloys.

3. Due to similar diffusion rates in liquid Al, virtually any trace element may be microalloyed into an appropriate aluminum alloy using this technique. However, the formation of an Al-trace element liquid phase at the sintering temperature may be a requirement.

4. Mass balance and thermodynamic calculations can be used to provide preliminary insight towards the success or failure of introducing a particular element.

5. The extent of alloying principally depended on the reducibility of the starting compound, the tendency of the addition to form intermetallics, and solid solubility in aluminum.

6. Of the elements considered, Ag was most readily microalloyed.

7. Using the technique, macro and micro scale alloying additions of Ag to the ternary alloy and Sn and Ag to AA2014 were possible. However, the incorporation of Li appeared to be unsuccessful.

8. Hot swaging resulted in the achievement of near full density in almost all sample types. However, the swaging of samples concentrated in Sn proved difficult.

9. Ag microalloying promoted an increase in Vickers hardness of 25 to 30 points, yield strength of ~60MPa, and UTS of 20 to 40MPa for the ternary alloy. Elongation to failure, however, was reduced by ~2%.

10. Ag additions to 2014 proved less effective than those made to the ternary alloy with only minor improvements in hardness noted.

11. The reduction in hardness and tensile properties associated with Sn additions was associated with exceeding the solid solubility limit.

12. The dominant precipitate produced during the aging of ternary alloy standards and P/M 2014 was θ'.

13. The dominant precipitate in ternary alloy samples microalloyed with Ag was found to be Ω. The improvement of mechanical properties noted for such Ag-microalloyed samples is postulated to result from the presence of Ω rather than θ' precipitates.

14. The dominant precipitate found in P/M 2014 samples microalloyed with Ag remained as θ' although certain evidence suggested that Ω was present in samples sintered for 16h.

15. When testing P/M alloy standards, wear resistance was found to diminish as sintering time was prolonged. This behaviour is a result of microstructural coarsening.

16. Comparing P/M and wrought 2014 suggested the latter possessed superior wear resistance.

17. Of all sample types examined (standard, Ag modified, and Sn modified P/M alloy and wrought 2014) the Sn modified P/M samples exhibited the highest wear resistance.

18. Through examination of weight loss data, wear tracks and wear debris, it seems that all samples are worn within the mild wear regime.

19. "Core/shell processing" is a unique means of alloying Al-based components that may well prove to be a viable industrial practice.

8 REFERENCES

1) H.N. Han and J.P. Clark, "Lifetime costing of the body in white: steel vs. aluminum," *JOM*, **47**, 5 (1995), 22-29.

2) E.J. Lavernia, T.S. Srivatsan, and F.A. Mohamed, "Review: Strength, deformation, fracture behaviour and ductility of aluminum-lithium alloys," *J. Mater. Sci.*, **25** (1990), 1137-1158.

3) E.J. Lavernia and N.J. Grant, "Aluminum-lithium alloys," *J. Mater. Sci.*, **22** (1987), 1521-1529.

4) E. Hornbogen and E.A. Starke, "Theory Assisted Design of High Strength Low Alloy Aluminum," *Acta. Metall. Mater.*, **41**, 1 (1993), 1-16.

5) C.P. Blankenship, Jr., E. Hornbogen, and E.A. Starke, Jr., "Predicting slip behavior in alloys containing shearable and strong particles," *Mater. Sci. Eng.*, **A169** (1993), 33-41.

6) R. Sankaran and C. Laird, "Effect of trace additions of Cd, In and Sn on the interfacial structure on kinetics of growth of θ' plates in Al-Cu alloy," *Mater. Sci. Eng.*, **14** (1974), 271-279.

7) S.P. Ringer, K. Hono, and T. Sakurai, "The effect of trace additions of Sn on precipitation in Al-Cu alloys: an atom probe field ion microscopy study," *Metall. Mater. Trans. A*, **26A** (1995), 2207-2217.

8) Y. Miura, K. Horikawa, K. Yamada, and M. Nakayama, "Precipitation hardening in an Al-2.4 Li-0.19 Sc alloy," Proceedings of the 4th International Conference on Aluminum Alloys, Atlanta, Georgia, USA, 2 (1994), 161-168.

9) J. Royset and N. Ryum, "Precipitation and recrystallization of an Al-Mg-Sc alloy," Proceedings of the 4th International Conference on Aluminum Alloys, Atlanta, Georgia, USA, 1 (1994), 194-201.

10) B.A. Parker, Z.F. Zhou, and P.Nolle, "The effects of small additions of scandium on the properties of aluminum alloys," *J. Mater. Sci.*, 30 (1995), 452-458.

11) I.J. Polmear, "The Effects of small additions of silver on the aging of some aluminum alloys," *Trans. Metall. Soc. AIME*, 230 (1964), 1331-1339.

12) A. Garg and J.M. Howe, "Convergent-beam electron diffraction analysis of the Ω phase in an Al-4.0 Cu-0.5 Mg-0.5 Ag alloy," *Acta. Metall. Mater.*, 39 (1991), 1939-1946.

13) J.H. Auld, "Structure of metastable precipitate in some Al-Cu-Mg-Ag alloys, " *Mater. Sci. Tech.*, 2 (1985), 784-787.

14) S.P. Ringer, W. Yeung, B.C. Muddle and I.J. Polmear, "Precipitate stability in Al-Cu-Mg-Ag alloys aged at high temperatures," *Acta. Metall. Mater.*, 42 (1994), 1715-1725.

15) J.T. Vietz and I.J. Polmear, "The influence of small additions of silver on the aging of some aluminum alloys: observations on Al-Cu-Mg alloys," *J. Inst. Metals*, 94 (1966), 410-419.

16) B. Skrotzki, G.J. Shiflet and E.A. Starke, Jr., "On the effect of stress on nucleation and growth of precipitates in an Al-Cu-Mg-Ag alloy," *Metall. Mater. Trans. A*, **27A** (1996), 3431-3444.

17) F.W. Gayle and J.R. Pickens, "Structure and properties during aging of an ultra-high strength Al-Cu-Li-Ag-Mg alloy," *Scripta Metall. Mater.*, **24** (1990), 79-84.

18) B. Skrotzki, G.J. Shiflet and E.A. Starke, Jr., "On the effect of stress on nucleation and growth of precipitates in an Al-Cu-Mg-Ag alloy," *Metall. Mater. Trans. A,* **27A**, 11 (1997), 3431-3444.

19) R.B.C. Cayless, "Alloy and temper designation systems for aluminum and aluminum alloys," in Metals Handbook, **2**, ASM, Metals Park, Ohio, (1990), 15-28.

20) D.L. Gilmore and E.A. Starke, "Trace element effects on precipitation processes and mechanical properties in Al-Cu-Li-X alloys" Proceedings of the 4th International Conference on Aluminum Alloys, Atlanta, Georgia, USA, **2** (1994), 313-320.

21) E.A. Starke, Jr. and F.S. Lin, "The influence of grain structure on the ductility of the Al-Cu-Li-Mn-Cd alloy 2020," *Metall. Trans. A*, **13A** (1982), 2259-2269.

22) L. Blackburn, W. Casada, G. Colvin, G. Shiflet, and E. Starke, Proceedings of the 1987 Aluminum-Lithium Symposium, Los Angeles, California, USA (1988), 225-236.

23) S.D. Park, B.H. Yoo, D.S. Chung, and H.K. Cho, "The effect of Be additions on precipitation response in Al-Li alloys," Proceedings of the 4th International Conference on Aluminum Alloys, Atlanta, Georgia, USA, **2** (1994), 207-214.

24) A. Luo and W.V. Youdelis, "Microstructure and mechanical behaviour of Al-Li-Cu-Mg alloy 8090 microalloyed with V and Be," *Metall. Trans. A*, **24A** (1993), 95-104.

25) A. Luo and W.V. Youdelis, "The effects of Be on mechanical properties and fracture behaviour of Al-Li alloy 8090," *Can. Metall. Quart.*, **31**, 4 (1992), 283-287.

26) A. Luo and W.V. Youdelis, "Clustering in a Be modified Al-Li-Cu-Mg alloy 8090," *Scripta Metall.*, **28** (1993), 29-34.

27) Q.H. Gui, X.J. Jiang, L.M. Ma, and Y.Y. Li, "Effect of 0.1% Y on microstructure and properties of 8090 Al-Li alloy," *Scripta Metall.*, **28** (1993), 297-300.

28) J.T. Al-Haidary and A.S. Jabur, "The effect of trace additions of tellurium on oxidation and some other properties of aluminum-lithium base alloys," *J. Mater. Sci.*, **30** (1995), 776-783.

29) U. Ramamurty, A. Bandyopadhyay, and E.S. Dwarakadasa, "Effect of heat treatment environment on Li depletion and on mechanical properties in Al-Li alloy sheets," *J. Mater. Sci.*, **28** (1993), 6340-6346.

30) T. Hagiwara, K. Kobayashi, and T. Sakamoto, "Effect of Li and Cu contents on the mechanical properties of Al-Cu-Li alloys," Proceedings of the 4th International Conference on Aluminum Alloys, Atlanta, Georgia, USA, **2** (1994), 297-304.

31) R.W. Cahn, " Grain Boundaries, Substructures and Impurities," in Impurities and Imperfections, ASM, Cleveland, Ohio, (1955), 41-83.

32) T.C. Lei, J. Sun, C.H. Tang, and M. Lei, " Precipitation- segregation mechanism for high temperature temper embrittlement of steels revealed by Auger electron spectroscopy and internal friction measurements," *Mat'ls Sci. Tech.*, **6**, 2 (1990), 124-133.

33) Raghavan Ayer, C.F. Klein, and C.N. Marzinsky, "Instabilities in Austenitic Stainless Steels," *Metall. Trans. A*, **23A** (1992), 2455-2467.

34) S.K. Chen, W.P. Nash, K.H. Hwang, C.M. Wan, and J.G. Byrne, "The sandwich structure for bcc grains in duplex Fe-Mn-Al-C alloys," *Scripta Metall. Mater.*, **24** (1990), 985-989.

35) N.H. Heo, "Nonequilibrium Grain Boundary Segregation and Ductile-Brittle-Ductile Transition in Fe-Mn-Ni-Ti Age-Hardening Alloy," *Metall. Mat'ls Trans. A*, **27A** (1993), 3059-3065.

36) M. Sundararaman and P. Mukhopadhyay, "Carbide Precipitation in Inconel 718," *High Temperature. Mat'ls Pro.*, **11** (1993), 1-4.

37) J.K. Park and A.J. Ardell, "Microchemical Analysis of Precipitate Free Zones in 7075-Al in the T6, T7 and RRA Tempers," *Acta. Metall. Mater.*, **39**, 4 (1991), 591-598.

38) M. Raghavan, " Microanalysis of Precipitate Free Zones (PFZ) in Al-Zn-Mg and Cu-Ni-Nb Alloys," *Metall. Trans. A*, **11A** (1980), 993-999.

39) K.K. Soni, D.B. Williams, J.M. Chabala, R. Levi-Setti, and D.E. Newbury, "Electron and Ion Microscopy Studies of Fe-Rich Second Phase Particles in Al-Li Alloys," *Acta. Metall. Mater.*, **40** (1992), 4, 663-671.

40) V. Radmilovic, A.G. Fox, R.M. Fisher, and G. Thomas, "Lithium Depletion in Precipitate Free Zones (PFZ's) in Al-Li Base Alloys," *Scripta Metall.*, **23** (1989), 75-79.

41) Z.W. Huang, M.H. Loretto, R.E. Smallman, and J. White, "The Mechanism of Nucleation and Precipitation in 7075-0.7Li Alloy," *Acta. Metall. Mater.*, **42**, 2 (1994), 549-559.

42) T.C. Sai and T.H. Chuang, "Atmospheric Stress Corrosion Cracking of a Superplastic 7475 Aluminum Alloy," *Metall. Mat'ls Trans. A,* **27A** (1996), 2617-2627.

43) E.A. Starke, "The Cause and Effects of "Denuded" or "Precipitate-Free" Zones at Grain Boundaries in Aluminum-Base Alloys," *J. Metals,* (1970), 54-63.

44) T.S. Srivatsan and E.J. Lavernia, "The presence and consequences of precipitate free zones in an aluminum-copper-lithium alloy," *J. Mater. Sci.*, **26** (1991), 940-950.

45) A.R. Harding in Aluminum Transformation and Technology, edited by C.A. Pampillo, H.Biloni, and D.E. Embury, ASM, Metals Park, Ohio (1978), 211-240.

46) I.M. Khatsinskaya, O.E. Grushko, L.M. Sheveleva, N.I. Kolobnev, P.D. Couch, and W.S. Miller, "The structure and phase transformations in Al-Li-Mg alloys containing Zr and Sc," Proceedings of the 4th International Conference on Aluminum Alloys, Atlanta, Georgia, USA, **2** (1994), 183-190.

47) H. Yong, W. Zhongping, Z. Yongli, H. Yunjia, and M. Liang, " Effect of alloying elements on solidification structure of 8090 Al-Li alloy welds," Proceedings of the 4th International Conference on Aluminum Alloys, Atlanta, Georgia, USA, **2** (1994), 481-487.

48) T.G. Nieh and J. Wadsworth, "High strain rate superplasticity of a powder metallurgy, Zr-modified 2124 aluminum alloy," Proceedings of the 4th International Conference on Aluminum Alloys, Atlanta, Georgia, USA, 2 (1994), 48-55.

49) A.B. De Ross and L.F. Mondolfo, in Aluminum Transformation and Technology, edited by C.A. Pampillo, H.Biloni, and D.E. Embury, ASM, Metals Park, Ohio (1978), 81-140.

50) N. Fat-Halla, "Recent developments in hypoeutectic Al-Si A-S4G alloy," *J. Mater. Sci.*, **25** (1990), 3396-3400.

51) Y.H. Tan, S.L. Lee and Y.L. Lin, "Effects of Be and Fe additions on the microstructure and mechanical properties of A357.0 alloys," *Metall. Mater. Trans. A*, **26A** (1995), 1195-1205.

52) L.Y. Wei, G.L. Dunlop, and H. Westengen, "The intergranular microstructure of cast Mg-Zn and Mg-Zn-rare earth alloys," *Metall. Mater. Trans. A*, **26A** (1995), 1947-1955.

53) Y.M. Vaynblat, B.A. Kopeliovich, and Y.G. Gol'der, *Phys. of Metals. Metallog.*, **42**, 5 (1976), 105-112.

54) Handbook of Chemistry and Physics, edited by R.C. Weast, 57th edition, the Chemical Rubber Company, Cleveland, Ohio, (1971), B63-B156.

55) A.J. McAlister, Binary Alloy Phase Diagrams, ASM, Metals Park, Ohio, (1986), 127-128.

56) A.J. McAlister and D.J. Kahan, Binary Alloy Phase Diagrams, ASM, Metals Park, Ohio, (1986), 167-168.

57) A.J. McAlister, <u>Binary Alloy Phase Diagrams</u>, ASM, Metals Park, Ohio,(1986), 3-4.

58) D.P. Bishop, "Reaction Sintering of Al-2014/Mineral Composites," M.A.Sc. Thesis, Technical University of Nova Scotia, Halifax, Nova Scotia, Canada (1995).

59) W.F. Caley, G.J. Kipouros and P.W. Kingston, "The potential application of naturally occurring minerals in ceramic and metal matrix composites," *CIM Bulletin*, **86**, 968 (1993) 116-121.

60) D.P. Bishop, G.J. Kipouros and, W.F. Caley, "Modification of the intergranular regions of aluminum alloys by reaction sintering of alloy/mineral mixtures" <u>Proceedings of the International Symposium on Light Metals</u>, Montreal, Quebec, Canada, August 1996, edited by M. Avedesian, R. Guilbault, and D. Ksinsik, CIM, 525-538.

61) D.P. Bishop, G.J. Kipouros, and W.F. Caley,"Diffusion-based alloying via reaction sintering," *J. Mater. Sci.*, **32** (1997), 2353-2358.

62) D.P. Bishop, J.R. Cahoon, M.C. Chaturvedi, G.J. Kipouros, and W.F. Caley, "Diffusion-Based Microalloying of Aluminum Alloys by Powder Metallurgy/Reaction Sintering," accepted for publication in the Journal of Materials Science (March 1998).

63) D.P. Bishop, X.Y. Li, K. Tandon, and W.F. Caley, "Dry Sliding Wear Behavior of Aluminum Alloys Microalloyed with Sn and Ag," submitted to *Wear*, February 1998.

64) D.P. Bishop, M.C. Chaturvedi, G.J. Kipouros, and W.F. Caley, "Diffusion-Based Microalloying of a Ternary Al-Cu-Mg P/M Alloy With Ag", Advances in Powder Metallurgy and Particulate Materials 1998, Metal Powder Industries Federation, Princeton, New Jersey (1998).

65) Energy, Mines and Resources Canada, Lithium: an imported mineral commodity, *Mineral Bulletin MR212*, (1986), 1-10.

66) W.B. Hampshire, "Tin and tin alloys," in Metals Handbook, 2, ASM Metals Park, Ohio, (1990), 517-526.

67) F. Rutley, Rutley's Elements of Mineralogy, Thomas Morley and Company, London, (1970), 255-262.

68) S.J. Blunder, The Industrial Uses of Tin Chemicals, The Royal Society of Chemistry, United Kingdom, (1985), 26-60.

69) C.R. Brooks, "Principles of Heat Treatment of Nonferrous Alloys," in Metals Handbook, Desk Edition, ASM, Metals Park, Ohio, (1992), 28•64-28•78.

70) I.J. Polmear and M.J. Couper, "Design and development of an experimental wrought aluminum alloy for use at elevated temperatures," *Metall. Trans. A*, **19A** (1988), 1027-1035.

71) J. Gronostajski and A. Tobota, "Thermomechanical treatment of 2014 aluminum alloy," *Mater. Sci. Tech.*, **4** (1988), 334-340.

72) W.F. Smith, Structure and Properties of Engineering Alloys, McGraw-Hill Publishing Company, Toronto, Canada, (1981), 176-189.

73) R.N. Wilson and P.G. Partridge, "The nucleation and growth of S' precipitates in in an aluminum-2.5% copper-1.2% magnesium alloy," *Acta. Metall.*, **13** (1965), 1321-1328.

74) A.K. Jena, A.K. Gupta and M.C. Chaturvedi, "A differential scanning calorimetric investigation of precipitation kinetics in the Al-1.53 wt% Cu-0.79 wt% Mg alloy," *Acta Metall.*, **37**, 3 (1989), 885-895.

75) ASM Committee on Aluminum and Aluminum Alloys, in Metals Handbook, 9th edition, Vol.2, Metals Park, Ohio, ASM International, (1979), 28-43.

76) "Standard specification for aluminum and aluminum alloy bar, rod and wire," ASTM Test B211-92a, **3.02** (1992), 173-181.

77) E.H. Hollinsworth and H.Y. Hunsicker, "Corrosion of aluminum and aluminum alloys," in Metals Handbook, **13**, ASM, Metals Park, Ohio, (1987), 583-609.

78) M.G. Fontana and R.D. Greene, Corrosion Engineering, McGraw-Hill Publishing Company, (1978), 340-380.

79) V.S. Sinyavskii, V.D. Val'kov, G.M. Toguzov and L.S. Guzei, "Effect of added tin on corrosion and electrochemical behaviour of aluminum," *Zashchita Metallov*, **23**, 5 (1987), 801-805.

80) D.S. Keir, M.J. Pryor and P.R. Sperry, "The influence of ternary alloying additions on the galvanic behavior of aluminum-tin alloys," *J. Electrochem. Soc.*, **116**, 3 (1969), 319-322.

81) R.G. Sarmurzina, A.A. Presnyakov, O.I. Morozova and N.N. Mofa, "Structure and properties of activated aluminum," *Fiz. Metal. Metalloved*, **66**, 3 (1988), 504-508.

82) D.A. Rigney, L.H. Chen, M.G.S. Naylor and A.R. Rosenfield "Wear processes in sliding systems," *Wear*, **100** (1984), 195-219.

83) J. Zhang and A.T. Alpas, "Transition between mild and severe wear in aluminum alloys," *Acta. Mater.*, **45**, 2 (1997), 513-528.

84) S.G. Caldwell, J.J Wert and G.A. Sloan, "A microscopic study of the behavior of selected Al-Cu alloys in unlubricated sliding wear," The International Conference on Wear of Materials, San Francisco, CA, edited by S.K. Rhee, A.W. Ruff and K.C. Ludema, (1981), 63-68.

85) S.M. Kuo and D.A. Rigney, "Sliding behavior of aluminum," *Mater. Sci. Eng. A*, **A157** (1992), 131-143.

86) S. Wilson and A.T. Alpas, "Effect of temperature on the sliding wear performance of Al alloys and Al matrix composites," *Wear*, **196** (1996), 270-278.

87) J.S. Zhang, X.J. Liu, H. Cui, X.J. Duan, Z.Q. Sun and G.L. Chen, "Microstructure and properties of spray deposited 2014+15 vol pct SiC particulate-reinforced metal matrix composites," *Metall. Mater. Trans. A*, **28A** (1997), 1261-1269.

88) S. Abis, G. Barucca and P. Mengucci, "Electron microscopy characterization of Al-Sn metal-metal matrix composites," *JALCOM*, **215** (1994), 309-313.

89) L.F. Mondolfo, <u>Aluminum Alloys : Structure and Properties</u>, Butterworth and Co. Ltd., Toronto, Ontario, (1979), 863-865.

90) B.K. Prasad and S. Das, "The significance of the matrix microstructure on the solid lubrication characteristics of graphite in aluminum alloys," *Mater. Sci. Eng. A*, **A144** (1991), 229-235.

91) B.K. Yen and T. Ishihara, "Effect of humidity on friction and wear of Al-Si eutectic alloy and Al-Si alloy-graphite composites," *Wear*, **198** (1996), 169-175.

92) B.K. Prasad, "Dry sliding wear response of some bearing alloys as influenced by the nature of microconstituents and sliding conditions," *Metall. Mater. Trans.* A, **28A** (1997), 809-815.

93) A. Kearney and E.L. Rooy, "Aluminum foundry products," in <u>Metals Handbook</u>, **2**, ASM, Metals Park, Ohio, (1987), 124-151.

94) ASM Committee on Definitions of Metallurgical Terms, "Glossary of metallurgical terms and engineering tables," in <u>Metals Handbook: Desk edition</u>, ASM, Metals Park, Ohio, (1992), 1•1-1•68.

95) R.W. Stevenson, "P/M lightweight metals" in Metals Handbook, 7, ASM, Metals Park, Ohio, USA, (1984), 741-764.

96) B.P. Saha and G.S. Upadhyaya, "Liquid phase sintering of T15 and T42 high-speed steel composites containing Ti (C,N)," *Int'l J. Powder Metall.*, 24, 6 (1992), 345-351.

97) J.E. Hatch, Aluminum: Properties and Physical Metallurgy, ASM, Metals Park, Ohio, USA, (1984), 379-397.

98) K. Sivakumar, K.S. Prasad, T.B. Bhat and P. Ramakrishnan, "Microstructural characteristics of shock consolidated 2124 Al alloy compacts," *J. Mater. Sci.*, 32, 19 (1996), 5271-5278.

99) D.S. Thompson, "Metallurgical factors affecting high strength aluminum alloy production," *Metall. Trans. A*, 6A (1975), 671-683.

100) J.P. Lyle and W.S. Cebulak, "Powder metallurgy approach for control of microstructure and properties in high strength aluminum alloys," *Metall. Trans. A*, 6A (1975), 685-699.

101) F.H. Froes and J.R. Pickens, "Powder metallurgy of light metal alloys for demanding applications," *J. Metals*, (1984), 14-28.

102) E. Lavernia, B. Poggiali, I. Servi, J. Clark, F. Katrak and N. Grant, "Rapidly solidified aluminum alloys: a market assessment," *J. Metals*, (1985), 35-38.

103) J.R. Pickens, "Review: aluminum powder metallurgy technology for high-strength applications," *J. Mater. Sci.*, **16** (1981), 1437-1457.

104) M.J. Couper, J.W. Luster and M. Thumann, "Development of elevated temperature powder metallurgy aluminum alloys," *Int'l J. Powder Metall.*, **23**, 1 (1991), 7-15.

105) J. Gwen, J.R. Groza, K. Yamazaki and K. Shoda, "Plasma activated sintering of tungsten powders," Mater. Man. Processes, **9**, 6 (1994), 1105-1114.

106) D.G. White, "P/M in North America," *Int'l J. Powder Metall.*, **32**, 3 (1996), 221-228.

107) W.D. Jones, <u>Fundamental Principals of Powder Metallurgy</u>, William Clowes and Sons Limited, (1960), 1-239.

108) E. Klar and J.W. Fesko, "Atomization," in <u>Metals Handbook</u>, 7, ASM, Metals Park, Ohio, USA, (1984), 25-51.

109) P. Schwarzkopf, Powder Metallurgy, The MacMillan Publishing Company, (1947), 33-47.

110) J. Wulff, Powder Metallurgy, ASM, Metals Park, Ohio, (1942), 1-35.

111) H. Hausner, "Characteristics of metal powders," New Types of Metals Powders, edited by H. Hausner, AIME, Gordon and Breach Science Publishers, New York, New York, USA, (1964), 1-8.

112) P.E. Price and S.P. Kohler, "Cold isostatic pressing of metal powders," in Metals Handbook, 7, ASM, Metals Park, Ohio, (1984), 444-450.

113) P.E. Price and S.P. Kohler, "Hot isostatic pressing of metal powders," in Metals Handbook, 7, ASM, Metals Park, Ohio, (1984), 419-443.

114) A.R. Erikson, R.E. Wiech, Jr., "Injection Molding," in Metals Handbook, 7, ASM, Metals Park, Ohio, (1984), 495-500.

115) L.B. Ferguson, O.D. Smith, "Ceracon Process," in Metals Handbook, 7, ASM, Metals Park, Ohio, (1984), 537-541.

116) L.B. Ferguson, "Spray deposition of metal powders," in Metals Handbook, 7, ASM, Metals Park, Ohio, (1984), 530-532.

117) J.H. Dudas and C.B. Thompson, "Improved sintering procedures for aluminum P/M parts," in Modern Developments in Powder Metallurgy, 5, Plenum Press, NY, (1971), 19-36.

118) R.M. German, "Supersolidus liquid phase sintering of prealloyed powders," Metall. *Mater. Trans. A,* **28A** (1997), 1553-1567.

119) ASM Committee on the Physical Fundamentals of Consolidation, "Physical fundamentals of consolidation," Metals Handbook, 7, ASM, Metals Park, Ohio, (1984) 308-321.

120) J. Svoba, H. Reidel and H. Zipse, "Equilibrium pore surfaces, sintering stresses and constitutive equations for the intermediate and late stages of sintering – I Computation of equilibrium surfaces," *Acta. Metall. Mater.,* **42,** 2 (1994), 435-443.

121) W.D. Kingery, H.K. Bowen and D.R. Ulhmann, Introduction to Ceramics, John Wiley and Sons, Toronto, Ontario, Canada, (1976), 469-501.

122) G.M. Janowski and B.J. Pletka, "The effect of particle size and volume fraction on the aging behaviour of a liquid phase sintered SiC/aluminum composite," *Metall. Mater. Trans. A*, **26A** (1995), 3027-3035.

123) J.R. Cahoon, "A re-evaluation of inverse segregation in the Al(rich)-Cu system," *Mater. Sci. Eng. A*, **A188** (1994), 211-217.

124) S.R. Thistlethwaite, "Review of alternative methods for alloying aluminum," in Light Metals 1993, edited by S.K. Das, TMS, (1993), 1175-1180.

125) A. Bahdur, T.L. Sharma, N. Parida, A.N. Mukherjee, and O.N. Mohanty, "Structure-property correlation in Al-diffusion coated steels," *J. Mater. Sci.*, **28** (1993), 5375-5381.

126) K. Stewart, "Boronizing protects metal against wear," *Adv. Mater. Pro.*, **3** (1997), 23-25.

127) B. Venkataraman and G. Sundararajan, "The high speed sliding wear behaviour of boronized medium carbon steel," *Surf. Coatings Tech.*, **73** (1995), 177-184.

128) A. Bloyce, "Surface engineering of non-ferrous alloys," *Trans. I.M.F.*, **72**, 2 (1994), 58-62.

129) R. Mevrel, C.Duret, and R. Pichoir, "Pack Cementation Processes," *Mater. Sci. Tech.,* **2** (1986), 201-206.

130) S.R.J. Saunders and J.R. Nicholls, "Coatings and surface treatments for high temperature oxidation resistance," *Mater. Sci. Tech.,* **5** (1989), 780-796.

131) G.H. Meier, C. Cheng, R.A. Perkins, and W. Bakker, "Diffusion chromizing of ferrous alloys," *Surf. Coatings Tech.,* **39/40** (1989), 53-64.

132) T.A. Kircher, B.G. McMordie, and A. McCarter, "Performance of a silicon-modified aluminide coating in high temperature hot corrosion test conditions," *Surf. Coatings Tech.,* **68/69** (1994), 32-37.

133) P. Lamesle, P. Steinmetz, J. Steinmetz, and S. Alperine,"Palladium modified aluminide coatings : Mechanisms of formation," *J. Electochem. Soc.,* **142,** 2 (1995), 497-505.

134) J. Jedlinski, K. Godlewski, and S. Mrowec, "The influence of implanted yttrium and cerium on the protective properties of a β-NiAl coating on a Nickel-base superalloy," *Mater. Sci. Eng. A,* **A121** (1989), 539-543.

135) B. Formanek, "The diffusion boronizing process of reactive atmospheres containing boron fluorides," *Mater. Sci. Forum*, **163-165** (1994), 317-322.

136) Y.R. He, R.A. Rapp and P.F. Tortorelli, "Oxidation-resistantGe-doped silicide coating on Cr-Cr$_2$Nb alloys by pack cementation," *Mater. Sci Eng. A*, **A222** (1997), 109-117.

137) R. Bianco and R.A. Rapp, "Pack cementation aluminide coatings on superalloys: Codeposition of Cr and Reactive Elements," *J. Electrochem. Soc.*, **140**, 4 (1993), 1181-1190.

138) P.A. Choquet, E.R. Naylor and R.A. Rapp, "Simultaneous chromizing and aluminizing of iron-base alloys," *Mater. Sci. Eng A*, **A121** (1989), 413-418.

139) M.H. Loretto, Electron Beam Analysis of Materials, Chapman and Hall Publishing Company, Toronto, Ontario, Canada, (1994), 242.

140) S. Kang and N. Grant, "Rapidly solidified P/M X2020 aluminum alloys," *Metall. Trans. A,* **18A** (1987), 2037-2045.

141) A.K. Gupta, P. Gaunt and M.C. Chaturvedi, "The crystallography and morphology of the S'-phase precipitate in an Al(CuMg) alloy," *Phil. Mag. A*, **55**, 3 (1987), 375-387.

142) B.C. Muddle and I.J. Polmear, "The precipitate Ω phase in Al-Cu-Mg-Ag alloys," *Acta. Metall.*, **37**, 3 (1989), 777-789.

143) W.T. Thompson, A.D. Pelton, and C.W. Bale, <u>F*A*C*T* Guide to Operations</u>, (1985), 1-43.

144) <u>Smithells Metals Reference Book, 6th Edition</u>, edited by E.A. Brandes, Butterworths Publishing Company, Toronto, Ontario, Canada, (1983), 13.1-13.97.

145) V. Burachynsky and J.R. Cahoon, "A theory for solute impurity diffusion, which considers Engel-Brewer valences, balancing the Fermi energy levels of solvent and solute, and differences in zero point energy," *Metall. Mater. Trans.*, **28A** (1997), 563-582.

146) G.H. Geiger and D.R. Poirier in <u>Transport Phenomena in Metallurgy</u>, Addison-Wesley Publishing Company, (1973), 458-460.

147) Personal communication, Cyril Cole, Technician, Minerals Engineering Centre, Technical University of Nova Scotia, March 23, 1997.

148) "Standard test methods for tension testing of metallic materials" in Annual Book of ASTM Standards, ASTM Test E8-93, **3.02** (1993), 130-149.

149) "Ranking resistance of materials to sliding wear using block-on-ring wear test," in Annual Book of ASTM Standards, ASTM Test G77-91, **3.02** (1991), 318-329.

150) S.P. Ringer, B.C. Muddle, and I.J. Polmear, "Effects of Cold Work on Precipitation in Al-Cu-Mg-(Ag) and Al-Cu-Li-(Mg-Ag) Alloys," *Metall. Mater. Trans. A*, **26A** (1995), 1659-1671.

151) Y.-S. Lee, S.P. Ringer, B.C. Muddle, and I.J. Polmear "Precipitate stability in alloys based on the Al-Cu System," in Proceedings of the 4th International Conference on Aluminum Alloys, Atlanta Georgia(USA), **2** (1994), 582-589.

152) K.R. Mecklenburg and R.J. Benzing, "Testing for adhesive wear," Proceedings of the Symposium on Selection and Use of Wear Tests for Metals, New Orleans, edited by R.G. Bayer, ASM, Metals Park, Ohio, (1975), 13-29.

153) S.G. Caldwell, J.J. Wert, and R.W. Carpenter, "The effects of stacking fault energy on sliding wear behavior of copper-aluminum alloys," in Wear of Materials, edited by S.K. Rhee, A.W. Ruff, and K.C. Ludema, ASME, New York, N.Y., (1981), 63-68.

154) B.D. Cullity, <u>Elements of X-Ray Diffraction</u>, Addison-Wesley Publishing Co., Don Mills, Ont., Canada, (1978), 286-288.

155) R.A. Antoniou, L.J. Brown, and J.D. Cashion, "The unlubricated sliding of Al-Si alloys against steel: Mossbauer spectroscopy and X-ray diffraction of wear debris," *Acta Metall. Mater.*, **42**, 10 (1994), 3545-3553.

156) <u>Powder Metallurgy Design Solutions</u>, brochure published by the Metal Powder Industries Federation, 105 College Road East, Princeton, New Jersey, (1993).

157) A. Tremblay and R. Angers, "Corrosion resistance of 316L P/M stainless steel," <u>Advances in Powder Metallurgy and Particulate Materials</u>, **7**, Metal Powder Industries Federation, Princeton, New Jersey, (1994).

A   Appendices

Appendix A:

Fabrication Flow Charts

Appendix B:

Density Data

Appendix C:

Hardness Data

Appendix D:

Tensile Data

Appendix E:

Wear Data (Weight Loss vs. Applied Load)

APPENDIX A: FABRICATION FLOW CHARTS

To prepare all of the samples required, two distinct P/M routes were employed. The routes followed in the production of alloy standards (ternary and 2014) and that used for core/shell samples are given in Figure A.1.

Isostatically Press
Master Alloy Powder
↓
Supersolidus Liquid
Phase Sintering
↓
Hot Swaging
↓
Heat Treatment
and Machining

(a)

Ball Mill Master Alloy
Powder and Element
Source Compound

Isostatically Press
Master Alloy Powder
to Form The "Core"

→ 2nd Isostatic Press ←

Supersolidus Liquid
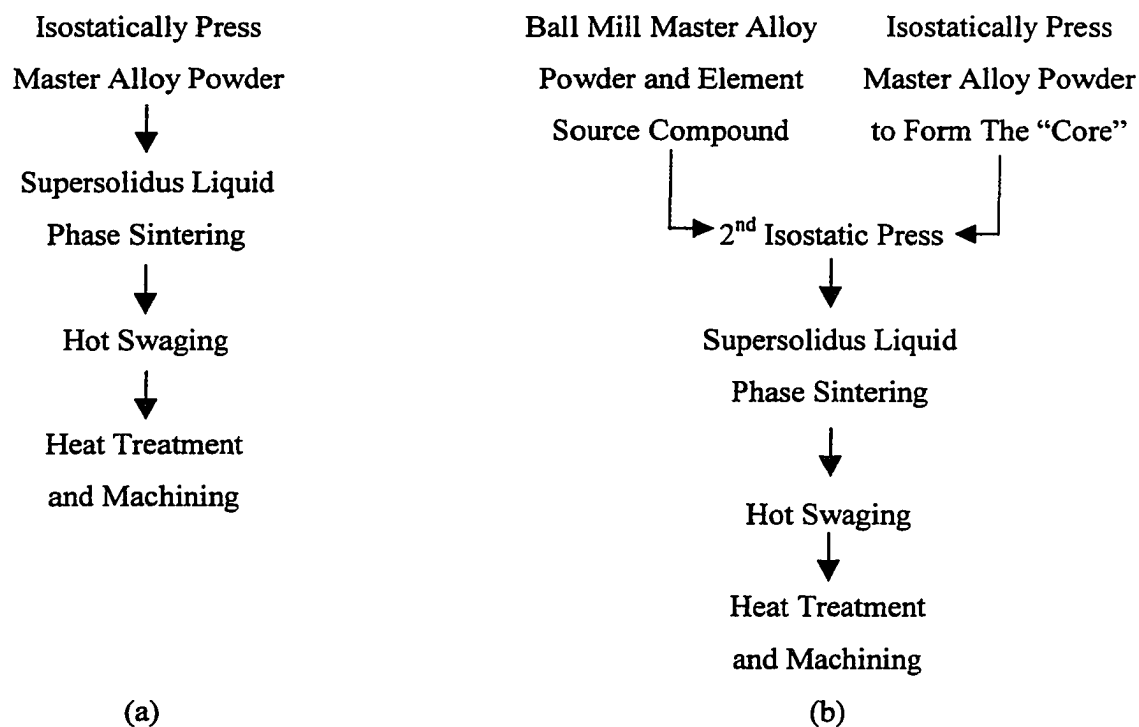Phase Sintering
↓
Hot Swaging
↓
Heat Treatment
and Machining

(b)

Figure A.1 Flow charts outlining the steps used the production of (a) alloy standards and (b) core/shell samples.

APPENDIX B: DENSITY DATA

Using mercury desitometry the densities of all P/M samples were measured. In most instances, two measurements were made for each sample type and an average value calculated. The results for alloy (ternary and 2014) standards sintered for various lengths of time are given in Table A.1. Values measured for microalloyed samples are presented in Tables A.2 and A.3.

Table A.1 Green and sintered body densities of ternary and 2014 P/M alloys.

Alloy System	Green (g/cc)	Average Green	Sintering Time (h)	As-Sintered (g/cc)	Average Sintered Density (g/cc)
Ternary	2.25, 2.25	2.25	2	2.33, 2.30	2.31 ± 0.02
			4	2.58, 2.63, 2.42	2.55 ± 0.08
2014	2.36, 2.28	2.32 ± 0.04	0.5	2.60, 2.71, 2.63	2.65 ± 0.07
			2	2.68, 2.69, 2.66	2.68 ± 0.02
			16	2.54, 2.53, 2.71	2.59 ± 0.10

Table A.2 Hot and cold swaged body densities of ternary and 2014 P/M alloys.

Alloy System	Sintering Time (h)	Hot Swaged[1] (g/cc)	Avg. Hot Swaged (g/cc)	Cold Swaged[2] (g/cc)	Avg. Cold Swaged (g/cc)
Ternary	2	2.71, 2.70	2.71 ± 0.01	-------	------
	4	2.72, 2.70	2.71 ± 0.01	-------	-------
2014	0.5	2.77, 2.78	2.77 ± 0.01	2.62, 2.73	2.68 ± 0.06
	1	2.74, 2.79	2.77 ± 0.02	2.74, 2.74	2.74
	16	2.77, 2.74	2.75 ± 0.02	2.75, 2.72	2.73 ± 0.02

1 Total RA of ~ 80%   2 Total RA of ~ 50%

Table A.3 Sintered body densities of microalloyed samples.

Alloy System	Sintering Time (h)	As-Sintered (g/cc)	Average Density (g/cc)
Ternary/Ag	2	2.54, 2.54, 2.58	2.56 ± 0.02
	4	2.58, 2.55, 2.64	2.60 ± 0.05
2014/Ag	2	2.47, 2.62, 2.69	2.59 ± 0.11
	4	2.59, 2.59, 2.51	2.56 ± 0.05
	16	2.63, 2.63	2.63
2014/Sn	0.5	2.66, 2.62, 2.51	2.60 ± 0.08
	1	2.55, 2.58	2.57 ± 0.02
	2	2.79, 2.77, 2.75	2.77 ± 0.02
	4	2.49, 2.59, 2.64	2.58 ± 0.08
	16	2.48, 2.59, 2.58	2.55 ± 0.06
2014/Li	16	2.66, 2.62, 2.62	2.63 ± 0.02

Table A.4 Hot and cold swaged densities of microalloyed samples.

System	Sintering Time (h)	Hot Swaged[1] (g/cc)	Average (g/cc)	Cold Swaged[2] (g/cc)	Average (g/cc)
Ternary/Ag	2	2.75, 2.75	2.75	-----	----
	4	2.78, 2.74	2.76 ± 0.02	------	----
2014/Ag	2	2.75, 2.76	2.75 ± 0.01	2.68, 2.75	2.73 ± 0.03
	4	2.79, 2.76	2.77 ± 0.02	2.77, 2.74	2.76 ± 0.02
	16	2.76, 2.68	2.72 ± 0.04	2.73, 2.68	2.71 ± 0.02
2014/Sn	0.5	2.77, 2.77	2.77	2.73, 2.74	2.73 ± 0.01
	1	2.76, 2.75	2.75 ± 0.01	2.70, 2.71	2.71 ± 0.01
	2	2.60, 2.71	2.65 ± 0.05	2.79, 2.76	2.77 ± 0.02
	4	2.78, 2.79	2.78 ± 0.01	2.75, 2.66	2.71 ± 0.05
	16	Shattered	------	2.70, 2.70	2.70
2014/Li	16	2.77, 2.76	2.76 ± 0.01	------	----

1 Total RA of ~ 80%   2 Total RA of ~ 50%

APPENDIX C: HARDNESS DATA

To determine the age hardening response of P/M samples, short segments of hot swaged rods were solutionized, water quenched and then aged for various lengths of time. To measure the hardness, two methods were used – Vickers hardness and Rockwell B hardness. Using an applied load of 1kg and a dwell time of 15 seconds, a Vickers hardness tester was used to measure the hardness of all samples based on the ternary alloy system (Table A.5). However, in samples based on the commercial alloy 2014, hardness was measured using an industrial Rockwell tester operating in the "B" scale (100 kg load, 1/8" diameter steel ball indentor). Results for such samples are given in Table A6.

Table A.5 Vickers hardness measurements of ternary alloy samples with and without Ag addition.

Sample	Sintering Time (h)	Aging Time (h)	HV	HV$_{avg}$
Ternary Std.	2	2	89, 94, 100, 93, 99	95 ± 3.7
		4	101, 102, 97, 101, 106	101 ± 2.1
		18	113, 116, 107, 113, 113	112 ± 3.8
		24	106, 113, 105, 113, 102	112 ± 5.3
Ternary Std.	4	2	95, 99, 88, 88, 92, 100	92 ± 5.0
		4	92, 89, 95, 92, 97, 88	93 ± 3.0
		18	106, 103, 113, 109, 113	109 ± 3.1
		24	113, 117, 106, 119, 110	113 ± 2.1
		96	127, 122, 131, 138, 135	130 ± 4.6
Ternary/Ag		18	125, 135, 135, 138, 138	134 ± 3.8
Ternary/Ag	4	2	135, 125, 128, 136, 135	132 ± 3.3
		4	132, 137, 140, 135, 143, 133	136 ± 1.4
		18	142, 143, 135, 143, 145	142 ± 2.1
		24	128, 132, 135, 127, 144	131 ± 1.9
		96	134, 126, 131, 130, 130	130 ± 1.6

Table A.6 Rockwell "B" hardness measurements of P/M alloy 2014 standard samples.

Sintering Time (h)	Aging Time (h)	HRB	HRB$_{avg}$
0.5	2	77.0, 76.0, 76.0, 76.0, 76.5, 77.1	76.4 ± 0.5
	4	80.4, 80.5, 79.4, 80.8, 78.9, 79.6	79.9 ± 0.7
	18	86.3, 86.2, 86.3, 86.9, 85.7, 85.7	86.2 ± 0.4
	24	88.0, 86.1, 87.5, 87.1, 87.0	87.2 ± 0.8
	96	87.5, 87.0, 88.0, 85.5, 86.8	87.1 ± 1.0
2	2	71.7, 73, 72.7, 72.6, 71.8, 71.6	72.2 ± 0.6
	4	81.6, 83.5, 82, 80.6, 80.5, 81.3	81.6 ± 1.1
	18	84.7, 84.1, 85.5, 83.7, 84.5, 84.4	84.5 ± 0.6
	24	84.5, 83.9, 85.8, 85.5, 84.4, 85.3	84.9 ± 0.7
	96	83.5, 82, 82.7, 80.7, 81.3, 83.4,	82.3 ± 1.1
16	2	68.1, 66.5, 69.3, 67.8, 65.7, 65.7	67.2 ± 1.5
	4	75.2, 74.4, 77.3, 74.9, 72.9, 76.6	75.2 ± 1.6
	24	78.4, 78.5, 79.6, 81.2, 80.5, 77.6, 79.3	79.3 ± 1.4
	96	80.7, 80.4, 79, 80.5, 82.2	80.6 ± 1.1

Table A.7   Rockwell "B"   hardness measurements of P/M alloy 2014 samples microalloyed with Ag.

Sintering Time (h)	Aging Time (h)	HRB	HRB$_{avg}$
2	2	75.3, 71.9, 71.3, 71.3, 73.1	72.6 ± 1.7
	4	79.3, 78.6, 79.4, 78.1, 78.6	78.8 ± 0.6
	18	85.5, 85.4, 85.4, 85.1, 85.4	85.4 ± 0.2
	96	81.2, 80.8, 81.0, 80.3, 81.8	81.0 ± 0.5
4	2	77.0, 77.5, 76.0, 75.5, 76.5, 77.5	76.7 ± 0.8
	4	84.0, 82.1, 82.5, 81.1, 81.6	81.8 ± 0.6
	18	85.5, 91.0, 85.0, 82.1, 88.3	86.3 ± 3.4
	24	86.5, 85.0, 87.0, 85.0, 86.5	86.0 ± 0.9
	96	83.0, 83.5, 87.1, 84.9, 83.5	84.4 ± 0.9
16	2	75.5, 77.0, 76.0, 76.1, 75.0	75.9 ± 0.7
	4	79.5, 81.0, 79.0, 80.5, 81.1, 81.5	80.4 ± 1.0
	18	86.5, 82.5, 82.5, 83, 82, 85.0, 82.0	83.4 ± 1.7
	24	84.5, 83.0, 83.0, 83.5, 83.4, 82.5	83.3 ± 0.7
	96	82.5, 80.5, 81.0, 81.5, 81.3	81.4 ± 0.9

Table A.8   Rockwell "B"   hardness   measurements   of P/M   alloy   2014   samples
microalloyed with Sn.

Sintering Time (h)	Aging Time (h)	HRB	HRB$_{avg}$
1	2	74.6, 75.2, 74, 72.7, 74.2, 73.3, 73.7	74.0 ± 0.8
	4	80.9, 81.1, 80.3, 81, 80.3, 80.2,	80.6 ± 0.4
	18	85.1, 84.7, 84.6, 86.1, 85.6	85.2 ± 0.6
	96	81.9, 82.5, 82.3, 81.4, 81.7,	82.0 ± 0.4
2	2	70.5, 71.6, 71.4, 69.3, 69.4, 68.3	70.1 ± 1.3
	4	80.4, 80.5, 79.4, 80.8, 78.9, 79.6	79.9 ± 0.7
	18	82.3, 82.3, 81.1, 82.9, 82, 82.5	82.2 ± 0.6
	96	81.7, 81.9, 82.2, 79.8, 79.7, 82.9, 80.6	81.3 ± 1.2
4	2	67.2, 65.8, 65, 66.3, 66.8, 63.5	66.2 ± 0.9
	18	80.2, 80.5, 80.8, 79.4, 79.5, 80.1	80.1 ± 0.6
	96	78.9, 80.2, 78.8, 77.8, 79.2, 75.2	79.0 ± 0.9
8	2	57.6, 63.1, 61.7, 64.5, 62.5, 61.2, 60.0	61.5 ± 2.2
	4	69.9, 70.7, 69.4, 67.1, 69.5	69.3 ± 1.3
	18	78.0, 79.6, 80.8, 78.5, 78.9, 78.6	79.2 ± 1.1
	96	77.6, 76.5, 77.8, 78, 76.9, 76.6	77.3 ± 0.7

APPENDIX D: TENSILE DATA

Using an Instron test frame, tensile tests were conducted in accordance with ASTM standards. Representative tests were conducted for all sample types considered in a T6 condition (Table A.9). Although duplicates for each sample type were heat-treated and machined, some were damaged during the final stage of preparation and thus were not tested. Hence, in some instances results were limited to a single test. Resulting stress vs. strain data were then analyzed using the in-house software programs to give engineering values for yield strength (0.2% offset), UTS and elongation to fracture.

Table A.9 Summary of engineering values measured in tensile tests.

System	Sintering Time (h)	Yield Strength (MPa)	UTS (MPa)	Elongation to Fracture (%)
Ternary Standard	2	337.6, 342.4 (340.0 ± 3.3)	401.6, 410.4 (406.3 ± 4.4)	16.3, 15.5 (15.5 ± 0.8)
	4	342.4	410.4	14.8
Ternary + Ag	2	386.8, 400.5 (393.7 ± 7.4)	422.3, 435.6 (428.9 ± 6.9)	13.0, 12.4 (12.7 ± 0.3)
	4	440.4, 457.1 (448.9 ± 8.4)	493.6, 505.1 (498.1 ± 7.0)	10.1, 13.3 (11.7 ± 1.6)
P/M 2014 Standard	0.5	460.0, 446.9 (453.6 ± 6.6)	514.0, 511.7 (512.9 ± 1.2)	11.7, 9.4 (10.5 ± 1.1)
	2	465.5	501.8	9.7
	16	435.7, 440.6 (438.1 ± 2.3)	487.7, 484.7 (486.2 ± 1.5)	11.4, 11.8 (11.6 ± 0.2)
P/M 2014 + Ag	2	449.3, 441.9 (445.6 ± 5.2)	499.2, 495.1 (497.2 ± 2.9)	10.6, 11.7 (11.2 ± 0.5)
	4	470.5, 457.0 (463.5 ± 6.3)	521.5, 505.1 (513.3 ± 8.3)	9.7, 10.1 (9.9 ± 0.2)
P/M 2014 + Sn	0.5	477.0	514.3	10.9
	1	448.5	492.5	10.5
	3	423.4	469.7	11.4
P/M 2014 + Li	16	402.5, 409.0 405.8 ± 3.3)	446.3, 474.0 (450.2 ± 14.1)	9.4, 15.0 (12.2 ± 2.8)

APPENDIX E: WEAR DATA (WEIGHT LOSS VS. APPLIED LOAD)

In accordance with ASTM standards, dry sliding wear testing was conducted on samples of P/M 2014 in a standard condition and when microalloyed with Ag or Sn. For each applied load, a minimum of four tests was run for each sample type. However, due to the common occurrence of uneven wear tracks, many results were not used. Only those results used in this thesis are presented in Tables A.10 to A.12. Prior to graphing this data (Figures 4.39 to 4.41) all points were normalized by dividing the weight loss by the total sliding distance of 1000 m.

Table A.10 Weight loss vs. applied load data for P/M 2014 standards.

Sintering Time (h)	Applied Load (N)	Weight Loss (mg)	Average Loss (mg)
0.5	9.8	1.1, 1.6, 1.6, 1.5	1.4 ± 0.2
	19.6	2.4, 2.9, 2.7, 2.6	2.7 ± 0.2
	39.2	5.7, 5.6, 5.9	5.8 ± 0.1
	98.0	8.0, 8.3, 8.1, 7.7	8.0 ± 0.3
16	9.8	1.4, 1.2, 1.2, 1.5	1.3 ± 0.2
	19.6	2.7, 3.1, 2.9, 2.9	2.9 ± 0.2
	39.2	5.6, 5.7, 5.5, 5.8	5.7 ± 0.1
	98.0	7.8, 7.8, 7.7, 7.9	7.8 ± 0.1

Table A.11   Weight loss vs. applied load data for P/M 2014 microalloyed with Sn.

Sintering Time (h)	Applied Load (N)	Weight Loss (mg)	Average Loss (mg)
0.5	9.8	1.4, 1.3, 1.5, 1.0	1.4 ± 0.2
	19.6	2.7, 2.4, 2.7, 3.0	2.6 ± 0.3
	39.2	4.9, 4.7, 4.7, 5.1	4.9 ± 0.2
	98.0	8.4, 8.3, 8.3, 8.5	8.4 ± 0.1
2	9.8	1.2, 0.9, 1.1, 1.1	1.1 ± 0.1
	19.6	2.4, 2.2, 2.1, 1.8	2.1 ± 0.2
	39.2	4.5, 4.4, 3.8, 4.2	4.2 ± 0.3
	98.0	7.8, 7.2, 7.9, 8.2	7.8 ± 0.3
4	9.8	1.2, 1.1, 1.4, 1.1	1.2 ± 0.1
	19.6	1.4, 2.1, 2.0	1.8 ± 0.4
	39.2	4.3, 4.4, 4.3, 4.3	4.3 ± 0.1
	98.0	6.9, 7.0, 6.8, 6.8,	6.9 ± 0.1

Table A.12 Weight loss vs. applied load data for P/M 2014 microalloyed with Ag.

Sintering Time (h)	Applied Load (N)	Weight Loss (mg)	Average Loss (mg)
4	9.8	1.3, 1.2, 1.2, 1.2	1.2 ± 0.1
	19.6	2.4, 2.1, 2.5, 2.4	2.4 ± 0.2
	39.2	4.6, 5.0, 4.9	4.8 ± 0.2
	98.0	7.2, 6.9, 7.1	7.1 ± 0.1
16	9.8	1.2, 1.4, 1.4	1.3 ± 0.1
	19.6	2.1, 2.4, 2.6, 2.2	2.3 ± 0.2
	98.0	7.5, 7.3, 7.3, 7.9	7.5 ± 0.3